Numerical Methods for Moving-Habitat Models in One and Two Spatial Dimensions

Jane Shaw MacDonald

Thesis submitted in partial fulfillment of the requirements for the degree of
Doctorate in Philosophy Mathematics and Statistics[1]

Department of Mathematics and Statistics
Faculty of Science
University of Ottawa

© Jane Shaw MacDonald, Ottawa, Canada, 2022

[1]The Ph.D. program is a joint program with Carleton University, administered by the Ottawa-Carleton Institute of Mathematics and Statistics

Abstract

Temperature isoclines are shifting with global warming. To survive, species with thermal niches must shift their geographical ranges to stay within the bounds of their suitable habitat, or acclimate to a new environment. Mathematical models that study range shifts are called moving-habitat models. The literature is rich and includes modelling with reaction-diffusion equations. Much of this literature represents space by the real line, with a handful studying 2-dimensional domains that are unbounded in at least one direction. The suitable habitat is represented by the set over which the demographics (reaction term) has a positive net growth rate. In some cases, this is a bounded set, in others, it is not. The unsuitable habitat is represented by the set over which the net growth rate is negative. The environmental shift is captured by an imposed shift of the suitable habitat. Individuals respond to their environment via their movement behaviour and many display habitat-dependent dispersal rates and a habitat bias. Such behaviour corresponds to a jump in density across the interface of suitable and unsuitable habitat. The questions motivating moving-habitat models are: when can a species track its shifting habitat and what is the impact of an environmental shift on a persisting species. Without closed form solutions, researchers rely on numerical methods to study the latter, and depending on the movement of the interface, the former may require numerical tools as well. We construct and analyse two numerical methods, a finite difference (FD) scheme and a finite element (FE) method in 1- and 2-dimensional space, respectively. The FD scheme can capture arbitrary movement of the boundary, and the FE method rather general shapes for the suitable habitat. The difficulty arises in capturing the jump across a shifting interface. We construct a reference frame in which the interfaces are fixed in time. We capture the jump in density with a clever placing of the nodes in the FD scheme, and through a Lagrange multiplier in the FE method. With biological applications, we demonstrate the power of our solvers in advancing research for moving-habitat models.

Dedications

This manuscript is dedicated to my grandmothers, Florence McCormick and the late Lorraine MacDonald. Your strength spans generations, and has inspired, guided, and supported me on this journey. I love you both dearly.

Acknowledgement

First and foremost, I thank my two supervisors, Dr Yves Bourgault and Dr Frithjof Lutscher, for their incredible support and kind, dedicated guidance. I have truly enjoyed working with both of you. I will often think back fondly on our meetings, which, no matter the content, always ended with a new lead, laughter, and smiles. I feel incredibly fortunate to have had the opportunity to learn from both of you. You are spectacular role models, and the lessons I have learned under your mentorship are of immeasurable value.

I am deeply grateful for the financial support that my supervisors provided me and supported me in obtaining. A big thanks goes to the NSERC Simulations-Based Engineering Sciences Program for their fiscal support and for all of the academic and professional activities they organised. Another big thanks goes to the Ontario Graduate Student Scholarship for their funding. I am extremely thankful to the Mathematics and Statistics Department for their fiscal support through out my years as a graduate student, providing me with opportunities to engage as an educator, and for supporting my nominations for internal scholarships in leadership roles. I thank TLSS for supporting my nomination for the Excellence in TA award and providing their fiscal support.

Through out my years in this program, I had the pleasure of working with and receiving mentorship and support from many people. Special thanks goes particularly to Dr Jaclyn Brusso, Dr Benoit Dionne, Dr Emmanuel Lorin, Dr Catherine Mavriplis, and Dr Monica Nevins.

My sincere thanks is extended to the entire Mathematics Department administrative team for their committed support, especially Diane Demers, Janick Rainville, Mayada El-Maalouf, and Carolynne Roy.

I would be amiss not to mention the support of the Women in Mathematics Club, particularly from my dear friends Dr Adèle Bourgeois, Alex McSween, Behnaz Refahi, and Dr Maiko Serizawa.

Many thanks goes to my friend Maryam Basiri for her support and time. Beyond being an amazing woman and dear friend, you are also one of my favourite people to talk about serious mathematics with, thank you for always being willing to do so.

Francesco, words cannot express my gratitude to you. You believed in me everyday and supported me constantly with kind words of encouragement. Your patience

and love provided an unwavering support through out this endeavour for which I am forever thankful.

My family, Mom, Dad, Maggie, and John, you have been my safest refuge through out my entire life and particularly, through out this PhD journey, that, as you know from many discussions has been great, but certainly not without its difficulties. I thank you deeply for the love and support you've given me through out this time.

I am indebted to a few friends who graciously offered their time to edit my texts, particularly, Elizabeth Hay. Elizabeth, your genuine excitement to read my work and consistent, unprompted offerings of your time always surprised me. From all of you, I have learnt a lot, and remain forever available to return the favour. In the same spirit, I thank my parents, Laura and Glen MacDonald, for willingly taking the time to read and give feed back on multiple texts.

Finally, to all my friends who, when I confided in them about the challenges I was facing, told me that I will overcome them, thank you many times over. Your words stayed with me and gave me courage. And it is with courage that this manuscript came to completion.

Contents

List of Figures

List of Tables

Chapter 1

Introduction

The ability of a species to persist in a given habitat has long been the motivating phenomenon for many mathematical and ecological studies. Understanding the conditions that keep a population striving in its habitat can assist in conservation science. The mathematics community has contributed many insights through mathematical modelling, which often, in the spirit of mathematics, characterises important concepts with model parameters. One such concept is the critical patch-size, frequently denoted by L^*. The critical patch-size highlights the delicate balance of spatial spread and growth. Species often need resource-rich environments to sustain their population levels. That is, there are suitable habitats, within which individuals can reproduce; outside such habitats, individuals are more likely to die. Since no habitat is infinitely long and individuals disperse and explore, the growth within the suitable habitat is balanced by dispersal away from it. Roughly speaking, L^* is the smallest a suitable habitat can be for a species to persist. This concept was first introduced via a reaction-diffusion equation by Skellam [58] in 1951 and then again by Kierstead and Slobodkin [32] in 1953.

A common modelling approach to use for these spatial dynamics are one-dimensional idealisations where the population density is modelled in time over some spatial domain. Of the many types of approaches within these idealisations, we focus on and introduce one here. The suitable habitat is represented by a bounded interval on the real line. Within this interval, the dynamics are governed by a reaction-diffusion equation describing movement and reproduction, outside the interval, movement and death. Then, L^* is measured by the length of the interval needed for the zero steady-state to be unstable. Historically, the critical patch-size was studied on a bounded domain with no consideration for the surrounding landscape and with hostile boundary conditions, meaning zero density at the boundary. The idea of including dynamics in the surrounding area came much later with Ludwig et al. [38]. These authors assumed that across the interfaces, which are the end points of the bounded interval across which dynamics abruptly change, flux and density were continuous. This as-

sumption was presumed natural and carried over to related literature.

The location where an environment goes from suitable to unsuitable is sometimes called a habitat edge. Individuals of many species change their movement behaviour across habitat types and near a habitat edge. For example, individuals commonly bias their movement towards a preferred patch and/or disperse faster within bad patches than within suitable ones [54, 51]. Ovaskainen and Cornell showed that considering such movement behaviour in a mathematical model results in a jump condition on density at the interface [44]. Maciel and Lutscher showed that mathematical models which include this jump condition give different outcomes for L^* than ones that do not [40].

For the past decades, climate change has been identified as a major contributor to species extinction and range shifts [45, 27, 31, 59, 60, 61]. A range shift occurs when a species' geographical range (in the sense of where the species can be found) moves. Range shifts as a result of climate change then indicate that some species are able to follow their suitable habitat as it shifts with the warming climate. Whether or not they can do this successfully in the long-run is unknown. Many mathematicians have considered this question and have suggested different models to analyse persistence-extinction outcomes, including models based on reaction-diffusion equations [48, 3, 39]. This small subset of the mathematical literature umbrellaed under the term *moving-habitat models* is the set most closely related to the content of this work. The common consensus of these papers is that the critical patch-size is dependent on the speed at which the suitable habitat moves. In [48] and [3] the authors find a critical speed of climate change above which extinction is inevitable. In [39] the aforementioned critical speed is found to be a soft threshold above which species whose individuals have particular movement behaviour may be able to persist. This soft threshold is a result obtained from generalising the interface conditions of [48] and [3] to include individual movement behaviour such as presented in [44, 40]. In all of these papers, the authors make the idealised assumption that the suitable habitat shifts at a constant speed.

Researchers have studied species presistance in the face of climate change using reaction-diffusion equations in higher spatial dimensions; see for example, [8]. In addition, Richter et al [52] present a numerical approach combined with GIS mapping in two space dimensions with temperature-dependent growth (the reaction term). The 2-dimensional analogue of the 1-dimensional problem studied in [39] is still an open question.

Moving-habitat models have proven foundational to understanding persistence conditions. Yet, these conditions are built on assumptions that often amount to some kind of averaging, for example, a constant shift of the suitable habitat. Moreover, we lack analytical tools to study the impact of deforming and shifting boundaries on population densities, or to study the population densities in transient times. The goal of this thesis is to provide computational tools to address the more realistic scenarios

being observed and recorded by scientists.

The main content of this work is three-fold. The first project is the development of a finite difference scheme for the spatially 1-dimensional system with arbitrary interface movement. In this project, we construct and validate the scheme before applying it to three ecologically motivated scenarios. For each scenario, we analyse the role of the model parameters, for example, habitat bias, on the population outcome. The second project focuses on the application of the finite difference scheme to periodic shifting speeds of the interfaces. We thoroughly investigate the impact of the amplitude of the periodic shift on population persistence and, given persistence, the impact of the amplitude and the frequency of the periodic shift on population densities. In the last project, we formulate a moving-habitat model in a 2-dimensional spatial setting that includes habitat-dependent movement behaviour. We develop and analyse a finite element method to solve the system in the case analogous to [39], that is, when the shift of the habitat is constant. We implement the method using the FreeFEM++ finite element library [25]. With this software, we validate the scheme numerically. Finally, we present a biologically motivated scenario.

Chapter 2

Literature Review

2.1 Reaction-Diffusion Equations and Spatial Ecology

Climate change can lower biodiversity, cause extreme weather, land degradation, and desertification [57]. One measurable quantity of climate change is the movement of the temperature isoclines poleward and/or upward in altitude [11]. Correspondingly, species with sensitive climatic niches shift or will shift their range to remain in their suitable habitat [27, 11]. In our modelling approach, we focus on such climate-driven range shifts.

In this section, we introduce the literature that motivated our research. We acknowledge that many other types of mathematical models have been used to study the problem of conservation in the face of climate change. What we present here is only a small subset. We specifically focus on the literature that relates closely to our mathematical model.

2.1.1 The 1-Dimensional Model and Ecological Results

In 2004, Potapov and Lewis [48] studied the impact of climate change on a two-species competition model. They describe the demographics and dispersal of the two species via a system of reaction-diffusion equations. The two species, represented by u_i, $i = 1, 2$, are tracked over the whole real line, where the suitable habitat is limited to a bounded interval, as described in Section 1. The bounded interval shifts along the real line at a constant speed c. The system is then, for $i, j = 1, 2$, $i \neq j$

$$u_{it} = D_i u_{ixx} + (r_i - \alpha_{ii} u_i - \alpha_{ij} u_j) u_i, \qquad L_1(t) < x < L_2(t),$$

$$u_{it} = D_i u_{ixx} - m_i u, \qquad x < L_1(t) \quad \text{or} \quad x > L_2(t),$$

where as $|x| \to \pm\infty$, $u \to 0$. Here, indices t and x denote partial derivatives. For species i, the model parameters D_i, r_i, α_{ii}, α_{ij} and m_i are the diffusion coefficient, the intrinsic growth rate, intra- and interspecies competition coefficients and mortality rate, respectively. The authors make the change of variable $x' = x - ct$, which then fixes the interface points $L_i(t)$ to $L_1(t) = 0$ and $L_2(t) = L > 0$ for all times $t > 0$. We call this the fixed system.

Among the various results presented in [48], the authors show equivalence of stability of the steady-states of the fixed system and that of the boundary value problem,

$$\begin{aligned} &u_{it} = D_i u_{ixx} + c u_{ix} + (r_i - u_i - \alpha_{ij} u_j) u_i, && 0 < x < L, \\ &u_{ix} - k_i^+ u_i = 0, && x = 0, \\ &u_{ix} - k_i^- u_i = 0, && x = L, \end{aligned}$$

for $i = 1, 2$, $i \neq j$, where r_1 and D_1 are scaled to 1 and D_2, r_2 and α_{ij} remain parameters of the system. The boundary conditions of this associated problem result from the method of Ludwig et al [38]. The density-flux proportionality constants $k_i^{\pm}$, are functions of the original model parameters, where $\pm$ denotes the sign of the function. (We give more detail on this method later within the present section.) With this equivalence, Potapov and Lewis conclude that the critical patch-size for the i^{th} species, denoted by L_i^* is an increasing function of c and that there exists a critical speed c_i^* for which as $c \to c_i^*$, $L_i^* \to \infty$.

In 2009, Berestycki et al [3] analysed a reaction-diffusion equation for the corresponding single species model in [48]. The authors use a geometric approach by studying the dynamics of the system via phase-plane analysis. They illustrate that non-zero solutions for the density, u, on the bounded interval $0 < x < L$ in the u, u_x-plane correspond to orbits that can leave from a point on the positively sloped half-line $u_x = \mu^+ u$ and reach a point on the negatively sloped half-line $u_x = \mu^- u$ in an interval of length L. Here $\mu^{\pm}$ take on the same role as $k_i^{\pm}$ do for the bounded system of [48]. They show that for such trajectories to exist, the origin must be a stable spiral, which happens only when $c < c^*$, the critical speed.

In 2018, MacDonald and Lutscher [39] generalized the reaction-diffusion models presented in [48] and [3]. They focused on a single species model and incorporated, inspired by the results of [40], interface conditions as derived in [44]. That is, the authors included habitat preference and habitat-dependent dispersal rates. The authors

describe population demographics via the logistic function. Their model was:

$$\begin{cases} u_t = Du_{xx} + u(r - au), & ct < x < L + ct, \\ u_t = d_1 u_{xx} - m_1 u, & x < ct, \\ u_t = d_2 u_{xx} - m_2 u, & x > L + ct, \\ \\ u\left((ct)^+, t\right) = k^\alpha u\left((ct)^-, t\right), \\ \left(Du_x + cu\right)\left((ct)^+, t\right) = \left(d_1 u_x + cu\right)\left((ct)^-, t\right), \\ \\ u\left((L + ct)^-, t\right) = k^\beta u\left((L + ct)^+, t\right), \\ \left(Du_x + cu\right)\left((L + ct)^-, t\right) = \left(d_2 u_x + cu\right)\left((L + ct)^+, t\right), \\ \\ k^\alpha = \frac{\alpha}{1-\alpha}\sqrt{\frac{d_1}{D}}, \qquad k^\beta = \frac{\beta}{1-\beta}\sqrt{\frac{d_2}{D}} \\ \\ \lim_{x \to \pm\infty} u(x, t) = 0, \end{cases} \tag{2.1.1}$$

where k^α and k^β are the respective factors of the jump in density across the interfaces $x = ct, L + ct$. The parameters α and β are the probabilities that an individual at the interface $x = ct, L + ct$, respectively, moves into the suitable habitat. The $\pm$ in the interface conditions denote the corresponding limits from the left and the right.

The authors make a change of variable $x' = x - ct$ and scale the variables D, r and a to unity. The resulting nondimensional system is

$$\begin{cases} \tilde{u}_{t'} = \tilde{u}_{x'x'} + c'\tilde{u}_{x'} + \tilde{u}(1 - \tilde{u}), & 0 < x' < L', \\ \tilde{u}_{t'} = D_1 \tilde{u}_{x'x'} + c'\tilde{u}_{x'} - m_1'\tilde{u}, & x' < 0, \\ \tilde{u}_{t'} = D_2 \tilde{u}_{x'x'} + c'\tilde{u}_{x'} - m_2'\tilde{u}, & x' > L', \\ \\ \tilde{u}\left(0^+, t'\right) = k^\alpha \tilde{u}\left(0^-, t'\right), \\ \left(\tilde{u}_{x'} + c'\tilde{u}\right)\left(0^+, t'\right) = \left(D_1 \tilde{u}_{x'} + c'\tilde{u}\right)\left(0^-, t'\right), \\ \\ \tilde{u}\left(L'^-, t'\right) = k^\beta \tilde{u}\left(L'^+, t'\right), \\ \left(\tilde{u}_{x'} + c'\tilde{u}\right)\left(L'^-, t'\right) = \left(D_2 \tilde{u}_{x'} + c'\tilde{u}\right)\left(L'^+, t\right), \\ \\ \lim_{x' \to \pm\infty} \tilde{u}(x', t') = 0, \end{cases} \tag{2.1.2}$$

with $\tilde{u} = \frac{a}{r}u$, $t' = rt$, $D_i = \frac{d_i}{D}$, $c' = \frac{c}{\sqrt{Dr}}$, $m_i' = \frac{m_i}{r}$ and $L' = L\sqrt{\frac{r}{D}}$. The already nondimensional terms k^α and k^β may now be written as $k^\alpha = \frac{\alpha}{1-\alpha}\sqrt{D_1}$ and $k^\beta = \frac{\beta}{1-\beta}\sqrt{D_2}$.

As before, the change of variable introduces a drift term into the resulting system. We drop the primes and tildes for notational simplicity. Solutions of System (2.1.2) mapped with the variable change $x \mapsto x + ct$ are solutions to the nondimensionalised form of System (2.1.1).

Following the method of [38], System (2.1.2) has an associated boundary-value problem on the spatial interval $x \in [0, L]$. At steady-state, $u_t = 0$. Thus, bounded solutions for u on the intervals $x < 0$ and $x > L$ are of the form

$$u(x) \sim e^{n_1^+ x}, \qquad u(x) \sim e^{n_2^- x} \tag{2.1.3}$$

respectively, where $n_i^{\pm} = \frac{-c}{2D_i} + \frac{\sqrt{c^2+4D_i m_i}}{2D_i}$. From the interface condition at $x = 0$, the steady-state solutions on $x < 0$ satisfy $u_x = n_1^+ u$. This relation combined with the interface conditions result in the left-boundary condition at $x = 0$, namely

$$u_x(0^+) + cu(0^+) = \frac{D_1 n_1^+ + c}{k^\alpha} u(0^+). \tag{2.1.4}$$

Similarly, one can obtain a right-boundary condition at $x = L$. The associated boundary-value problem of System (2.1.2) is

$$\begin{aligned} &u_t = u_{xx} + cu_x + u(1-u), && (x,t) \in (0,L) \times \mathbb{R}^+, \\ &u_x + cu = \gamma_0^\alpha u, && \text{at } x = 0, \\ &u_x + cu = \gamma_0^\beta u, && \text{at } x = L, \end{aligned} \tag{2.1.5}$$

where $\gamma_0^\alpha = \frac{D_1 n_1^+ + c}{k^\alpha} = \frac{c+\sqrt{c^2+4m_1 D_1}}{2k^\alpha}$ and $\gamma_0^\beta = \frac{D_2 n_2^- + c}{k^\beta} = \frac{c-\sqrt{c^2+4m_2 D_2}}{2k^\beta}$.

The authors then prove that although non-steady state dynamics are different for the two systems, steady-state solutions within $x \in [0, L]$ coincide. Thus, the authors are able to, in the same spirit as [48], prove equivalence of stability of steady-states between the systems (2.1.5) and (2.1.2).

With this theorem, the authors then present conditions for instability of the zero steady-state. They employ a similar approach as in [3] by using a phase plane analysis. We summarise their results here in two lemmas, for more details we refer the reader to [39].

Lemma 2.1.1. *When $c < 2$, a finite critical patch-size exists and is given by*

$$\sin(z_0 L^*) \left[z_0^2 + \left(\frac{c}{2} - \gamma_0^\alpha \right) \left(\frac{c}{2} - \gamma_0^\beta \right) \right] = \cos(z_0 L^*) z_0 \left(\gamma_0^\alpha - \gamma_0^\beta \right), \tag{2.1.6}$$

where $z_0 = \frac{\sqrt{4-c^2}}{2}$.

Lemma 2.1.2. *For all $c \geq 2$, there exists a critical value $\bar{k}^\alpha = \frac{c+\sqrt{c^2+4m_1D_1}}{c-\sqrt{c^2-4}}$, such that for any $k^\alpha > \bar{k}^\alpha$ and $k^\beta > 0$ a finite critical patch-size exists and is given by*

$$\sinh(s_0L^*)\left[s_0^2 + \left(\gamma_0^\beta - \frac{c}{2}\right)\left(\frac{c}{2} - \gamma_0^\alpha\right)\right] = \cosh(s_0L^*)s_0\left(\gamma_0^\beta - \gamma_0^\alpha\right), \tag{2.1.7}$$

where $s_0 = \frac{\sqrt{c^2-4}}{2}$.

The threshold value $c = 2$ is the corresponding critical speed found in [3] and [48], above which a finite critical patch-size does not exist. Thus, the analysis of [39] suggests that this threshold is somehow *soft*: Species that have particular movement rates and strong preferences for their suitable habitat may still be able to persist for speeds of climate change above this threshold.

For all of these analyses, the critical speed c^* is equal to the Fisher speed [21]. In ecology, this speed is the asymptotic speed of the front of invasion of an initially small population introduced in an infinitely good habitat [58]. In the unscaled model, $c^* = 2\sqrt{rD}$. Thus, the results of the critical spreading speed, inform us that a population cannot survive if the habitat shifts faster than the asymptotic spreading speed of the population.

One limiting assumption common to all three of the models we presented here is that space is idealised to one dimension. An argument for this simplification is that temperature heterogeneity is most severe across latitudinal lines, and temperature isoclines are shifting poleward [11]. Yet, topography can introduce difficult to pass barriers, like mountains. For a more realistic spatial setting, one can consider two spatial dimensions. The next section presents some literature that has tackled this problem.

2.1.2 The 2-Dimensional Model

The number of sources that are tackling the impact of climate change via mathematical modelling in a 2-dimensional domain is growing, although remains small relative to the set considering only one spatial dimension. We highlight here two studies that employ reaction-diffusion equations.

In 2008 and 2009, Berestycki et al [4], [5] generalised their results from [3], which we discussed in the previous section, to a spatially d-dimensional system. They introduced a system with rather general assumptions on the reaction term. The suitable habitat is determined by the bounded domain over which the net growth rate is positive. They proved existence and uniqueness of travelling-wave-type solutions and characterised the long-time solutions with respect to the speed of the shift.

More recently, Bouhours and Giletti [8], studied a moving-habitat model in d spatial dimensions, $d \geq 1$, where they generalised further the reaction term to include weak Allee effects. An Allee effect is a positive correlation between density and growth rate for some values $0 < u < b$, where b is a positive constant and u is population density. They studied the asymptotic behaviour of solutions to the reaction-advection-diffusion equation

$$u_t = \Delta u + cu_x + f(x, y, u) \quad t > 0, \quad (x, y) \in \mathbb{R} \times \omega,$$

where $\omega \subseteq \mathbb{R}^{d-1}$, $d \geq 1$ and $c \geq 0$. Here, $u = u(x, y, t)$ is the population density in space (x, y) and time t. The function f is the growth function, and its spatial dependence describes the heterogeneity of the habitat. With the change of variable $x \to x + ct$, the above equation is equivalent to

$$u_t = \Delta u + f(x - ct, y, u), \qquad t > 0, \quad (x, y) \in \mathbb{R} \times \omega.$$

So we see that c describes a constant shift of the habitat. In their scenario, f as a function of x is nondecreasing and as $x \to \pm\infty$, $f(\cdot, y, u) \to g_{\pm}(u)$, where $g_{-}(u) \leq 0$ $u \geq 0$, and g_{+} is a reaction term that supports population growth. For example, this could be the logistic function as in System (2.1.1), although as already stated, they consider more general functions. When $d = 2$, the spatial setting is an open region of $\mathbb{R}$ on which there is one interface that shifts at speed c cutting the region into two distinct subdomains. The subdomain to the left of the interface represents the unsuitable habitat, and the subdomain to the right, the suitable habitat. For this model, the authors find conditions under which a population goes to extinction or persists, and they characterise the outcome based on the shifting speed, and due to the Allee effect, the initial condition.

No one has yet included habitat-dependent movement behaviour in their analysis of persistence conditions in two spatial dimensions. Additionally, the studies for moving-habitat models in spatially 2-dimensional systems do not yet include an analysis of the impact on population densities. For example, in the one-dimensional case, Berestycki et al [3], show that the largest population sizes are supported at intermediate shifting speeds. (See Chapter 3, where we find parameter ranges and the mechanisms for which such situations occur.) Alternatively, transient dynamics are at least as important as long-time solutions. For example, in a shrinking habitat, the population may be doomed. Studying the shape of density profiles through transient stages can help identify populations that may need conservation assistance. Such population analysis has the potential to assist ecologists in establishing key characteristics to identify populations that are the most susceptible to extinction. Numerical methods provide a way to perform such studies.

2.2 Numerical Mathematics Background

Two main challenges arise when developing a numerical method to solve a moving-habitat model with habitat-dependant movement behaviour. The first challenge is to describe the movement of the interfaces over the discretised space. The second challenge is to accurately capture the solution across the interface. In this section, we review numerical techniques that motivate the construction of our numerical solvers.

2.2.1 Moving Domains: Numerical Approaches

The first step in constructing a numerical scheme is developing an appropriate mesh. The mesh should reflect the geometry of the spatial domain and adapt to the dynamics of the system. In this section, we illustrate ways to adapt the mesh to fit the boundary of the moving domain. Following Donea et al [14], we discuss here the arbitrary Lagrangian-Eulerian (ALE) description of motion. The ALE description combines the pure Eulerian and the pure Lagrangian descriptions. Donea et al had the application of fluid dynamics in mind and so the particle velocity is available at all points of the domain for all times. Thus, one can identify a material domain, defined by the material particles, that is distinct from the spatial domain. In the pure Eulerian description, the material particles move with respect to the mesh. In the pure Lagrangian approach, the spatial domain is discretised so that every grid node is permanently attached to a material particle. The model that we are interested in has a prescribed advective velocity only for the interfaces. We adapt the terminology used in [14] to fit our case.

To describe the methods, we consider a model problem similar to System (2.1.1). Let $u = u(x,t)$ be the density in time, t and space, x. Let $L_i(t) \in \mathbb{R}$, $i = 1, 2$, be such that $L_2(t) > L_1(t)$ for all t and define $\Gamma(t) = \{L_1(t), L_2(t)\}$. Then consider the parabolic problem

$$u_t - D_i u_{xx} - F(x,t,u) = 0, \qquad x \in \mathbb{R}\backslash\Gamma(t), \tag{2.2.1}$$

where

$$D_i = \begin{cases} D_0, & L_1(t) < x < L_2(t), \\ D_1, & \text{otherwise}, \end{cases}$$

$$F(x,t,u) = \begin{cases} u(r - au), & L_1(t) < x < L_2(t), \\ -mu, & \text{otherwise}, \end{cases}$$

and $r, a, m, D_0, D_1 \in \mathbb{R}^+$. Considering this equation as a description of population density, the equation states that the change of density in time is equal to dispersal

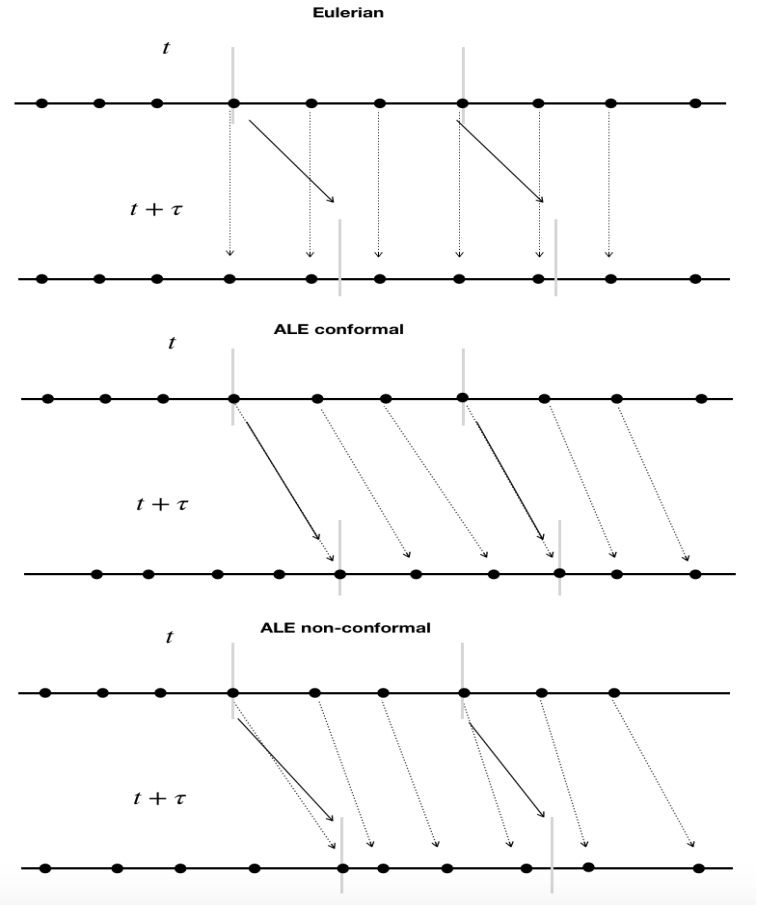

Figure 2.1: Illustrated comparison of the Eulerian, ALE conformal and ALE non-conformal spatial mesh for System (2.2.1). Light grey lines denote the location of $L_1(t)$ and $L_2(t)$. Bullet points denote nodal placement. Dotted arrows denote mesh motion and solid arrows denote interface motion.

by diffusive movement and the growth/death process, which is either logistic growth or linear death given by F. The coefficients, D_i, $i = 0, 1$ are the diffusion rates of the species and r, a, and m are the intrinsic growth rate, intraspecies competition coefficient, and mortality rate, respectively. The system is not complete because we are missing interface conditions across $\Gamma(t)$.

Our system is currently written in an Eulerian frame. The interfaces move continuously with respect to a fixed spatial domain. A corresponding mesh, in lieu of any adaptation, would thus have a fixed set of nodes. As time t increases, the interface points, described by $\Gamma(t)$, move across the mesh made up of fixed grid points (Figure 2.1). Donea et al point out that Eulerian formulations of numerical schemes are quite capable of treating large distortions of the interface, which is a favourable property. In our unidimensional problem, this occurs when $|L_2(T) - L_1(T)| \gg |L_2(0) - L_1(0)|$,

$T > 0$. When the interface moves relative to a fixed coordinate system, at any time t, the interface falls either on a node or between two nodes of the grid. Moreover, the nodes linked to the interface change in time. The numerical scheme then requires the use of the immersed interface method [35], [34], or interpolation and remeshing at every time step. Not only can these steps complicate the scheme and its implementation, but can also introduce losses in accuracy. One main difficulty is to obtain a high-order method beyond first order in grid size.

In our model example, the ALE description requires the use of two coordinate systems, one to represent the physical space x of Problem (2.2.1) and one to describe the computational domain, over which a mesh is built and the numerical solution is computed. In fluid mechanics, there is a third closely related coordinate description defined by the material particles, namely the Lagrangian description. A change in coordinate systems requires a restatement of the system via a bijective mapping $\varphi^{-1}(x,t) = (\tilde{x}(x,t),t)$. This mapping defines the reference frame. For example, the reference frame could be chosen so that $\varphi^{-1}(x,t)$ maps to the initial configuration at $t = 0$. Thus, one could align the interface with the same node for all time, an advantageous strategy with respect to the computational effort. Donea et al note that to obtain a one–to–one correspondence, the mapping φ must satisfy $\det(\partial x/\partial\tilde{x})(x,t) \neq 0$, and to impose invariance in orientation of the reference axes $\det(\partial x/\partial\tilde{x})(x,t) > 0$.

For a given mapping φ, the change of variable $v(\tilde{x}(x,t),t) = u(x,t)$ transforms System (2.2.1) to

$$v_t - \frac{D_i}{x_{\tilde{x}}^2} v_{\tilde{x}\tilde{x}} + \left(\frac{D_i x_{\tilde{x}\tilde{x}}}{x_{\tilde{x}}^3} - \frac{x_t}{x_{\tilde{x}}} \right) v_{\tilde{x}} - F(\tilde{x},t,v) = 0, \qquad \tilde{x} \in \mathbb{R}\backslash\tilde{\Gamma}. \tag{2.2.2}$$

A mesh is now built and computations carried in the $\tilde{x}-$coordinate system. We note that our description of motion in (2.2.2) differs from that in [14] as they are missing the term $\frac{D(\tilde{x},t)x_{\tilde{x}\tilde{x}}}{x_{\tilde{x}}^3}$, that comes from the second derivative. It is likely that in [14] the authors are working under the assumption that $x_{\tilde{x}}$ is constant in $\tilde{x}$, while we make no such assumption. The mapping $\varphi(\tilde{x},t)$ then gives us the solution for Problem (2.2.1) on the $x-$coordinate system. In the ALE description, the choice of $x(\tilde{x},t)$ introduces a mesh velocity

$$\left.\frac{\partial x}{\partial t}\right|_{\tilde{x}},$$

where the notation $|_{\tilde{x}}$ means holding $\tilde{x}$ fixed. This velocity describes the motion of the mesh points in the physical frame relative to the computational grid $\tilde{x}$. While the computational domain remains fixed in time, the physical domain changes. For Problem (2.2.1), there is a clear choice for the velocity specification at the interface points $x = L_i(t)$, that being exactly the velocity of the interface. However, some arbitrariness results in the specification of the velocity over the whole domain. In general, the choice of mapping $x(\tilde{x},t)$ may lead to a conformal grid with the interfaces, see middle illustration of Figure 2.1, or a non-conformal grid, see bottom illustration

of Figure 2.1. Here, conformal refers to the interfaces aligning with a grid point at every time step, akin to a Lagrangian approach. Thus, a conformal grid arises when in the initial configuration a node is attached to the interface, and this nodal velocity equals the velocity of the interface.

The addition of the advective term, $\left(\frac{D(\tilde{x},t)x_{\tilde{x}\tilde{x}}}{x_{\tilde{x}}^3} - \frac{x_t}{x_{\tilde{x}}}\right) v_{\tilde{x}}$, in Equation (2.2.2) requires attention in the construction of the numerical scheme as it introduces an asymmetry to the spatial operator. For example, taking a finite difference approach, one could consider using an upwind scheme. In the case of large distortions of the domain in time, any arbitrary choice of mapping φ will likely introduce large distortions on the mesh in the physical domain. Adaptive meshing, where one remeshes at every time step, or at least when the mesh gets distorted, could remedy this problem [47]. The ALE approach is beneficial as it permits solving the system over a fixed computational domain. It is worth to note that in Section 2.1.1, the change of variable $x' = x - ct$ sets up an ALE description of motion.

With the ALE description the challenge of our moving interfaces is resolved. In the 1-dimensional system, we use a conformal ALE description and we accurately capture the jump in density by placing two nodes on the interface; see Chapter 3. In the 2-dimensional system, again with a conformal ALE description, we construct a hybrid finite element method, reviewed in the next section, where the jump in density is weakly enforced via Lagrange multipliers; see Chapter 5.

2.2.2 Hybrid Finite Element Methods with Lagrange Multipliers

Hybrid finite element methods were introduced in 1977 by Raviart and Thomas [50] as a way to relax both continuity conditions and Dirichlet conditions on the finite element space. A typical finite element space is defined over a triangulation of the domain, where across the elements of the triangulation, continuity of the finite element functions is enforced if one considers conformal approximations. A conformal approximation is when the finite dimensional space of the approximate solution is a subset of the infinite dimensional space to which the solution belongs. Additionally, the variational space and the finite dimensional approximation space respect the homogeneous Dirichlet conditions along the boundary of the domain. The goal for Raviart and Thomas was to build a finite dimensional approximation that did not enforce these conditions strongly. They introduced hybrid finite element methods, where they restate the problem with the addition of a new variable, a Lagrange multiplier or the dual variable, that weakly enforces the continuity and Dirichlet conditions. The space of the dual variable is defined on the faces of the elements. They prove that their hybrid problem is well-posed and that the first unknown, usually referred to as the primal variable, is the solution to the original problem. They define their hybrid system over the triangulated domain and obtain error estimates for both the primal

and dual variables.

In such an approach, the finite dimensional space of the approximate solution is not a subset of the infinite dimensional space to which the solution belongs, thus, the method is called nonconforming. In such a case, error estimates involve a consistency error, where the deviation of X_h, the finite dimensional space, from X, the variational space of the solution, is measured. Such error estimates involve the space of the Lagrange multiplier. Thus, the finite dimensional space of the Lagrange multiplier needs to be properly chosen so that the discrete system is well-posed and that error estimates are possible.

A comparable approach called the mortar method was originally introduced for spectral elements over decomposed domains [42]. Mavriplis motivated this approach as a way to accurately employ locally nonconforming/globally conforming meshes. A mesh is said to be conforming if the intersection of any two elements is either empty, a common single vertex, or an entire common single edge. In a decomposed domain, it is desirable to mesh each subdomain independently of the other, for example, to reduce algorithmic burden in the mesh generation.

Another benefit of the mortar method is the coupling of methods over the decomposition. Bernardi et al [7, 6] applied the mortar method to decomposed domains where they coupled spectral methods, spectral and finite element methods, and finite element methods across these domains. They prove results for multiple interpolation approximations and obtain global a priori error estimates as a sum of the consistency error and the approximation error.

Belgacem [2] further studied the mortar element method via a hybrid approach. The approach is similar to Raviart and Thomas but rather than relaxing the continuity conditions in the finite element space, Belgacem, working over a decomposed domain, relaxes the continuity conditions across the interfaces within the variational space. Belgacem obtains a priori error estimates for both the original unknown function and the Lagrange multiplier in cases where the decomposition of the domain is conforming and nonconforming. The definition of a conforming decomposition is similar to that of a conforming mesh, which we stated above.

When working with decomposed domains, as in [42, 7, 6, 2], the intersection of the boundary of the domain and the interfaces of the decomposition may not be empty. In such cases, one should consider special treatment of the mortar/Largrange multiplier. Such treatment results in working in $H_{00}^{\frac{1}{2}}$, where if a boundary and the closure of an interface have a common vertex, then at that point, the trace of the mortar/Lagrange multiplier is mapped to zero. In the finite element case, when using polynomial elements of degree s on the triangulation of an interface, elements that have vertices on boundaries are treated specially, where the polynomial order is reduced by one.

We review the hybrid finite element method by following a similar structure as Raviart and Thomas [50, 2], through a model problem of our design. Let Ω be

an open bounded subset of $\mathbb{R}^2$, with a Lipschitz continuous boundary $\partial\Omega$ such that $\Omega = \bar{\Omega}_0 \cup \Omega_1$, where $\partial\Omega_0 = \Gamma$, a closed curve in $\mathbb{R}^2$, $\bar{\Omega}_0 \cap \bar{\Omega}_1 = \Gamma$, $\Gamma \cap \partial\Omega = \varnothing$, and $\partial\Omega_1 \cap \partial\Omega = \partial\Omega$ (Figure 2.2). We consider the model problem

$$\begin{aligned} -\Delta u_i &= f_i, \quad \text{on } \Omega_i, i = 0, 1, \\ u_0 &= u_1, \quad \text{on } \partial\Omega, \\ \partial_{\boldsymbol{\nu}} u_0 &= \partial_{\boldsymbol{\nu}} u_1, \quad \text{on } \Gamma, \\ u &= 0, \quad \text{on } \partial\Omega, \end{aligned} \tag{2.2.3}$$

where $f \in L^2(\Omega)$ is such that $f|_{\Omega_i} = f_i$, $\boldsymbol{\nu}$ is the unit normal along Γ pointing into Ω_1, and Δ is the Laplace operator; i.e., $\Delta = \partial_{xx} + \partial_{yy}$. If $f_i = f_i(u)$ were functions suitable to describing population dynamics, then this equation would be the steady-state system for a two-patch type model with continuity across the interface and Dirichlet boundary conditions on Ω. Dirichlet conditions represent a hostile boundary, where individuals who cross this boundary never return. In this model, there is no environmental shift. For simplicity, we assume that f_i depends only on the spatial parameter, $\boldsymbol{x}$.

This system is equivalent to the non-homogeneous Laplace equation

$$\begin{aligned} -\Delta u &= f, \quad \text{on } \Omega, \\ u &= 0, \quad \text{on } \partial\Omega, \end{aligned} \tag{2.2.4}$$

for which the variational problem is: Find $u \in H_0^1(\Omega)$ such that

$$\int_\Omega \nabla u \nabla v \, \mathrm{d}\boldsymbol{x} = \int_\Omega f \, \mathrm{d}\boldsymbol{x}, \qquad \forall v \in H_0^1(\Omega),$$

where $H^1(\Omega)$ refers to the Sobolev space of functions that are in $L^2(\Omega)$ and whose first derivatives are in $L^2(\Omega)$, and $H_0^1(\Omega)$ contains functions in $H^1(\Omega)$ that vanish on the boundary of Ω.

For the system in the decomposed domain, we can derive an equivalent variational problem. Let $X = \{w = (w_0, w_1) \in H^1(\Omega_0) \times H_0^1(\Omega_1) \ : \ w_0 = w_1 \text{ on } \Gamma\}$. A well-posed variational problem equivalent to System (2.2.4) is: Find $u \in X$ such that

$$\sum_{i=0}^{1} \int_{\Omega_i} \nabla u_i \nabla v_i \, \mathrm{d}\boldsymbol{x} = \sum_{i=0}^{1} \int_{\Omega_i} f_i v_i \, \mathrm{d}\boldsymbol{x}, \qquad \forall v \in X. \tag{2.2.5}$$

In this formulation, the continuity of density is enforced strongly in the function space X on both the solution u and the test function v. This condition is difficult to implement accurately into a finite element method if one wishes to maintain the advantages of the decomposed domain. One such advantage could be to use a locally conforming/globally nonconforming mesh.

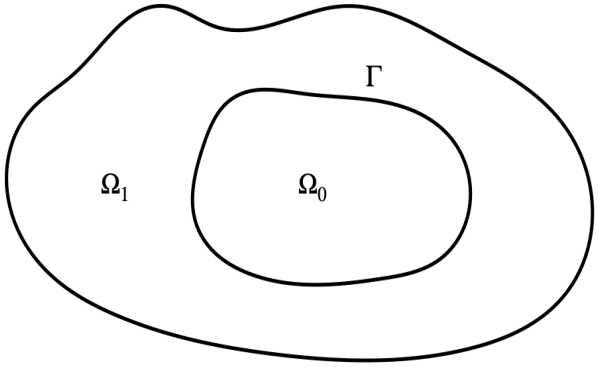

Figure 2.2: The decomposition of the domain Ω.

The hybrid finite element method allows a relaxation of the strongly enforced condition. Let

$$H(\mathrm{div};\Omega) = \{\boldsymbol{q} \in (L^2(\Omega))^2 \ : \ \mathrm{div}\boldsymbol{q} \in L^2(\Omega)\}.$$

By the Trace theorem (Theorem 1.3.2, [49]) the normal component of vector-valued functions $\boldsymbol{q} \in H(\mathrm{div};\Omega)$ is defined in $H^{-\frac{1}{2}}(\partial\Omega)$, the dual space of $H^{\frac{1}{2}}(\partial\Omega)$. That is, $\boldsymbol{q}\cdot\boldsymbol{n} \in H^{-\frac{1}{2}}(\partial\Omega)$, where $\boldsymbol{n}$ is the normal component along $\partial\Omega$. Similar definitions hold over Γ. Define

$$X = \{v \in L^2(\Omega) \ : \ (v_0, v_1) \in H^1(\Omega_0) \times H_0^1(\Omega_1) \ \},$$

and

$$M = \{\mu \in H^{-\frac{1}{2}}(\Gamma) \ : \ \exists \boldsymbol{q} \in H(\mathrm{div};\Omega) \text{ such that } \boldsymbol{q}\cdot\boldsymbol{\nu} = \mu \text{ on } \Gamma\}.$$

The hybrid formulation under consideration is then: Find $(u,\lambda) \in X \times M$ such that

$$\begin{aligned} a(u,v) + b(v,\lambda) &= \int_\Omega fv \ \mathrm{d}\boldsymbol{x}, \quad \forall v \in X, \\ b(u,\mu) &= 0 \ \mathrm{d}\boldsymbol{x}, \quad \forall \mu \in M, \end{aligned} \tag{2.2.6}$$

where

$$a(u,v) = \sum_{i=0}^{1} \int_{\Omega_i} \nabla u_i \nabla v_i \ \mathrm{d}\boldsymbol{x}, \qquad b(u,\mu) = \int_\Gamma \mu[u] \ \mathrm{d}s, \tag{2.2.7}$$

and $\int_\Gamma$ represents the duality pairing of $H^{-\frac{1}{2}}$ and $H^{\frac{1}{2}}$, and $[u] = u_0 - u_1$. Belgacem shows that the linear function $b : X \times M \to \mathbb{R}$ characterises $H_0^1(\Omega)$:

$$H_0^1(\Omega) = \{v \in X \ : \ b(v,\mu) = 0, \ \forall \mu \in M\}.$$

With the following theorem, Raviart and Thomas prove that Problem (2.2.6) is well-posed and that the unique u, the primal solution of Problem (2.2.6), is also

the solution of System (2.2.4). Additionally, they characterise the meaning of the Lagrange multiplier.

Theorem 2.2.1. *Problem (2.2.6) has a unique solution* $(u, \lambda) \in X \times M$. *Moreover,* $u \in H_0^1(\Omega)$ *is the solution of System (2.2.4) and*

$$\lambda = -\partial_{\boldsymbol{\nu}} u_0.$$

The proof uses the characterisation of $H_0^1(\Omega)$ through the bilinear form b. We have a similar statement in Chapter 5 where we consider a hybrid formulation of our 2-dimensional system that incorporates a jump in density across the interface Γ. Our proof borrows elements from the proof of Raviart and Thomas [50], but with modifications to capture the jump across Γ.

For the discretisation, one needs to choose finite dimensional spaces $X_h \subset X$ and $M_h \subset M$. For example, one can take X_h to be the union of the following two spaces

$$X_h^i = \{v_h \in \mathcal{C}(\bar{\Omega}_i) \ : \ v_h|_K \in \mathbb{P}_s(K), \forall K \in \mathcal{T}_h^i)\}$$

where K are the elements of the triangulation $\mathcal{T}_h^i$ over Ω_i. For M_h one can choose

$$M_h = \{\mu_h \in \mathcal{C}(\Gamma) \ : \ \mu_h|_F \in \mathbb{P}_s(F), \forall F \in t\},$$

where K are the elements of the triangulation t over Γ, such a triangulation can be defined by the triangulation over one of the domains Ω_i. With this set up, one can obtain error estimates for both u and λ, following ideas presented in [7, 6, 2].

In Chapter 5, we develop a similar hybrid formulation to the one we presented above. However, our Lagrange multiplier weakly enforces a jump of the form $u_0 = \kappa u_1$, where $\kappa \neq 1$ is a constant. Special treatment of M_h, as mentioned earlier, is omitted in our case, since the boundary Γ doesn't intersect with the boundary $\partial\Omega$. Finally, our main goal is good approximations of u. Thus, within this dissertation, we omit the error analysis of λ.

In the next section, we introduce two papers that focus on numerical methods in an ecological application. We highlight the differences between our problem and the ones that apply to their finite element method, and the contributions that a numerical scheme can make in ecological theory.

2.3 Numerics of Ecological Problems

In 2015, Garvie et al [22] released a collection of open-source finite element solvers to study reaction-diffusion equations of predator-prey models over arbitrarily shaped

2-dimensional domains with varying types of boundary conditions. Their goal was to illustrate the importance of habitat shape and boundary conditions on spatiotemporal dynamics, and, at the same time, provide code that can enable researchers with similar model types to further their studies.

They illustrate their findings with the classic Rosenzweig-MacArthur predator-prey model

$$u_t = \Delta u + h_1(u, v), \tag{2.3.1}$$
$$v_t = \delta \Delta v + h_2(u, v). \tag{2.3.2}$$

Here $u = u(\mathbf{x}, t)$ is the prey, $v = b(\mathbf{x}, t)$ is the predator with $\mathbf{x} = (x_1, x_2) \in \mathbb{R}^2$ and $t > 0$. The function

$$h_1 = u(1 - u) - \frac{uv}{u + \alpha},$$

describes the intrinsic birth and death dynamics and the effect of predation within the prey population and

$$h_2 = \frac{\beta uv}{u + \alpha} - \gamma v,$$

describes benefit from predation and linear death within the predator population. The parameters α, β, δ and γ are all positive constants. The authors consider the equation over a bounded domain $\Omega \subset \mathbb{R}^2$ with smooth or Lipschitz polygonal boundary $\Gamma = \Gamma_1 \cup \Gamma_2$ such that $\Gamma_1 \cap \Gamma_2 = \varnothing$. That is, they decompose their boundary into two distinct parts. This decomposition allows them to consider multiple boundary condition scenarios, where for example, on Γ_1 and Γ_2 they enforce Dirichlet boundary conditions and Neumann boundary conditions, respectively.

The authors formulate three weak formulations to capture all the considered boundary conditions. For each weak formulation the authors give precise definitions of solvability for all $0 < t < T$ and, within this interval, prove that there exist unique, nonnegative global solutions.

The authors use a standard Galerkin method to approximate the solutions of the three infinite dimensional weak problems with finite dimensional ones. They discretise time so that solutions of the finite element method are linear with respect to the time level. They do so by linearizing h_1 and h_2 around the solution at the previous time step. By doing so they are able to obtain a linear system for each of the three problems. They take advantage of the linearity at every time step to obtain a linear system for implementation of their numerical approach.

They then apply their finite element methods to study the population dynamics' dependence on the choice of boundary conditions and geometric shape of Ω. From their experiments, they conclude that boundary conditions and the geometric shape of the domain can have a profound effect on spatial heterogeneity of the two species' densities. For example, they find that wave-like phenomena can be induced by boundary conditions or obstacles, which they introduce by placing a hole inside Ω.

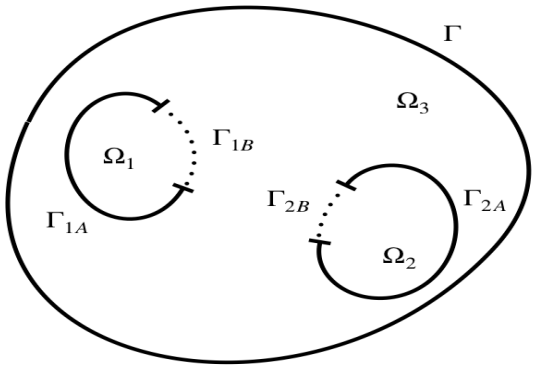

Figure 2.3: A recreation of Figure 1 in [23] illustrating the spatial domain Ω in two space dimensions.

We find this paper to be particularly motivating as the authors' contribution is similar in spirit to what we will do with our research. Their goal to create open-source and user friendly code is shared. Researchers outside of mathematics – our target audience are ecologists and/or biologists – could enhance their research with an accessible numerical approach. Their paper highlights the flexibility of a finite element method and how adaptable it can be to arbitrary spatial domains, including ones with obstacles (holes) and narrow corridors. Finally their experiments show the value of a numerical approach in furthering understanding of the ecologically relevant mechanisms that underly the fascinating dynamics that are observed in the natural world.

The term metapopulation is used to describe a population inhabiting many patches which are connected by migration. In 2017, Garvie et al [23] developed a finite element method to solve a system of reaction-diffusion equations describing a predator-prey metapopulation with Rosenzweig-MacArthur dynamics. The spatial domain consists of a bounded domain $\Omega \subset \mathbb{R}^d$, $d \leq 3$ with a sufficiently regular boundary Γ such that Ω lies locally to one side of Γ. The authors define two domains $\Omega_i \subset \mathbb{R}^d$, $i = 1, 2$ such that $\bar{\Omega}_i \subset \Omega$, $\bar{\Omega}_1 \cap \bar{\Omega}_2 = \varnothing$ and Ω_i lies locally to one side of $\partial\Omega_i$. They define $\Omega_3 = \Omega \backslash (\bar{\Omega}_1 \cup \bar{\Omega}_2)$ and the interfaces between the subdomains Ω_i and Ω_3 to be Γ_{iA} and Γ_{iB} smooth nonempty connected domains in $\partial\Omega_3$ such that $\bar{\Gamma}_{iA} \subset \partial\Omega_i$ and $\Gamma_{iB} = \partial\Omega_i \backslash \bar{\Gamma}_{iA}$. See Figure 2.3 for an example illustration of the domain Ω. The nondimensionalised model they study over this spatial domain is

$$\frac{\partial u_i}{\partial t} = \Delta u_i + u_i(1 - u_i) - \frac{u_i v_i}{u_i + \alpha}, \qquad \text{on} \quad \Omega_i \times (0, T), \quad i = 1, 2, \tag{2.3.3}$$

$$\frac{\partial u_i}{\partial t} = D\Delta v_i + \beta \frac{u_i v_i}{u_i + \alpha} - \gamma v_i, \qquad \text{on} \quad \Omega_i \times (0, T), \quad i = 1, 2, \tag{2.3.4}$$

$$\frac{\partial u_3}{\partial t} = D_1 \Delta u_3 - \xi_1 u_3, \qquad \text{on} \quad \Omega_3 \times (0,T), \tag{2.3.5}$$
$$\frac{\partial v_3}{\partial t} = D_2 \Delta v_3 - \xi_2 v_3, \qquad \text{on} \quad \Omega_3 \times (0,T), \tag{2.3.6}$$

together with initial and boundary conditions

$$u_i(x,0) := u_{i0}(x), \qquad v_i(x,0) := v_{i0}(x), \qquad \text{on} \quad \Omega_i \quad \text{for} \quad i = 1,2,3, \tag{2.3.7}$$
$$\frac{\partial u_i}{\partial n_i} = \frac{\partial v_i}{\partial n_i} = 0, \qquad \text{on} \quad \Gamma_{iA} \times (0,T), i = 1,2, \tag{2.3.8}$$
$$\frac{\partial u_3}{\partial n_3} = \frac{\partial v_3}{\partial n_3} = 0, \qquad \text{on} \quad (\Gamma \cup \Gamma_{iA}) \times (0,T), i = 1,2, \tag{2.3.9}$$
$$\frac{\partial u_i}{\partial n_i} = D_1 \frac{\partial u_3}{\partial n_3}, \qquad D\frac{\partial v_i}{\partial n_i} = D_2 \frac{\partial v_3}{\partial n_3}, \qquad \text{on} \quad \Gamma_{iB} \times (0,T), i = 1,2, \tag{2.3.10}$$
$$u_i = u_3, \qquad v_i = v_3, \qquad \text{on} \quad \Gamma_{iB} \times (0,T), i = 1,2. \tag{2.3.11}$$

Here, u_i and v_i, $i = 1,2,3$, are the prey and predator population, respectively, in subdomain Ω_i. D is the diffusion rate of the predator population in Ω_i, $i = 1,2$, α is the prey handling constant, β is the benefit of predation rate, γ is the predator mortality rate, D_1 and D_2, ξ_1 and ξ_2 are the diffusion and mortality rates of the prey and predator population, respectivley, in Ω_3. We denote the outward pointing normal of Ω_i, by n_i, $i = 1,2,3$. Equations in (2.3.10) and (2.3.11) describe continuity of density and flux for both predator and prey along the Γ_{iB} interface. Equations (2.3.8) and (2.3.9) describe no flux along Γ_{iA} and Γ for both predator and prey. Thus, the equations all together describe a two patch metapopulation connected by migration through one interface per patch and the hostile environment.

They define the variables $(U,V) = (u_i, v_i)$ for $x \in \Omega_i$, $i = 1,2,3$, and restate the system over the decomposed domains as a system over the entire domain $\tilde{\Omega} = \Omega \backslash \left(\bar{\Gamma}_{1A} \cup \bar{\Gamma}_{2A}\right)$. That is,

$$\frac{\partial U}{\partial t} = \nabla \cdot (\delta_1 \nabla U) + F(U,V), \qquad \text{on} \quad \tilde{\Omega} \times (0,T),$$
$$\frac{\partial V}{\partial t} = \nabla \cdot (\delta_2 \nabla V) + G(U,V), \qquad \text{on} \quad \tilde{\Omega} \times (0,T),$$

where

$$F(U,V) := \begin{cases} u_i(1-u_i) - \frac{u_i v_i}{u_i + \alpha}, & \text{for} \quad x \in \Omega_i, i = 1,2, \\ -\xi_1 u_3, & \text{for} \quad x \in \Omega_3, \end{cases}$$
$$G(U,V) := \begin{cases} \beta \frac{u_i v_i}{u_i + \alpha} - \gamma v_i, & \text{for} \quad x \in \Omega_i, i = 1,2, \\ -\xi_2 v_3, & \text{for} \quad x \in \Omega_3, \end{cases}$$

$$\delta_1(x) := \begin{cases} 1, & \text{for} \quad x \in \Omega_i, i = 1, 2, \\ D_1, & \text{for} \quad x \in \Omega_3, \end{cases}$$

$$\delta_2(x) := \begin{cases} D, & \text{for} \quad x \in \Omega_i, i = 1, 2, \\ D_2, & \text{for} \quad x \in \Omega_3. \end{cases}$$

Since they assumed continuity in density across the interfaces, the system in the (U, V) variable has a variational formulation where all of the interface and boundary conditions are natural and do not need to be enforced in the solution space. The variational formula is:

Find $U(\cdot, t), V(\cdot, t) \in H^1(\tilde{\Omega})$ such that $(U(\cdot, 0), V(\cdot, 0)) := (u_0(\cdot), v_0(\cdot))$ and for a.e. $t \in (0, T)$ we have for all $\nu \in H^1(\tilde{\Omega})$

$$\int_{\tilde{\Omega}} \nu \frac{\partial U}{\partial t} dx + \int_{\tilde{\Omega}} \delta_1 \nabla \nu \cdot \nabla U dx = \int_{\tilde{\Omega}} \nu F(U, V) dx, \tag{2.3.12}$$

$$\int_{\tilde{\Omega}} \nu \frac{\partial V}{\partial t} dx + \int_{\tilde{\Omega}} \delta_2 \nabla \nu \cdot \nabla V dx = \int_{\tilde{\Omega}} \nu G(U, V) dx, \tag{2.3.13}$$

where $(u_0(x), v_0(x)) = (u_{0i}(x), v_{0i}(x))$ if $x \in \Omega_i$, $i = 1, 2, 3$.

They discretise the problem in space with a standard Galerkin finite element method with piecewise linear basis functions over triangles. For time, they use a finite difference discretisation. To obtain a simplified linear system of equations they use the 'mass lumping' technique. They are able to obtain a partially coupled linear system and at each time step they solve their system in two steps solving first for V^n and then secondly for U^n, where V^n and U^n are the vectors containing the approximation of the values for the predator and prey density, respectively, over the spatial domain $\tilde{\Omega}$. They validate their finite element method with mesh refinement.

The authors developed a flexible and efficient finite element method for populations with differing dynamics over spatial subdomains. They have provided a tool to study a multitude of ecologically motivated scenarios for which analytical solutions are not available. We aim to establish similar advancements for the moving-habitat model. There are two important differences between our system and theirs. Firstly, the good patch is moving, and secondly we do not enforce continuity of density across the interface. Garvie et al applied differing diffusion rates between the good and bad patches. However, they also comment that assuming continuity of density across the interfaces, although convenient for the variational formulation and finite element set up, may or may not be correct given the ecological situation one wishes to model. We claim that with the differing diffusion constants it is indeed incorrect in accordance with the papers by Ovaskainen and Cornell [44], and Maciel and Lutscher [40]. Still, by assuming continuity of density across the boundary Garvie et al were able to simplify incorporating the interface condition in the mesh set up and so avoid numerical complications that could arise by making special considerations on the interfaces.

The main difficulty we overcome in this thesis is developing numerical schemes that can accurately capture the jump in density. In Chapter 3, we develop such a scheme for the spatially 1-dimensional model with arbitrary movement of the interface with a finite difference approximation. In Chapter 5, we do so for the spatially 2-dimensional model for a constant shifting speed of a suitable habitat with arbitrary shape with a finite element approximation. Both methods create a host of opportunities for future research, for mathematicians and ecologist alike.

Chapter 3

A Finite Difference Scheme in One-dimensional Space

In this chapter I present my publication in Mathematical Biosciences. In the first half of this paper, I develop and validate a finite difference scheme to solve the moving-habitat model with general interface movement in one-dimensional space; see Section 2.1. In the second half of this paper, I present three ecologically relevant scenarios.

This paper is co-authored with my supervisors. With my supervisors, I discussed the selection of methodology and the biological interpretations made. I implemented the methods and carried out the computations, analyses and numerical validation. Finally, I drafted the paper and my supervisors provided editorial guidance.

Mathematical Biosciences 341 (2021) 108711

Contents lists available at ScienceDirect

Mathematical Biosciences

journal homepage: www.elsevier.com/locate/mbs

Original Research Article

Moving-habitat models: A numerical approach

Jane S. MacDonald [a,*], Yves Bourgault [a], Frithjof Lutscher [a,b]

[a] University of Ottawa, Department of Mathematics and Statistics, 150 Louis-Pasteur Pvt, K1N 6N5, Ottawa, Canada
[b] University of Ottawa, Department of Biology, Canada

ARTICLE INFO

Keywords:
Moving-habitat models
Finite difference method
Reaction–diffusion equation
Individual movement behaviour
Transient dynamics

ABSTRACT

As the global climate changes, biological populations have to adapt in place or move in space to stay within their preferred temperature regime. Empirical evidence suggests that shifting speeds of temperature isoclines are location and elevation dependent and may accelerate over time. We present a mathematical tool to study transient behaviour of population dynamics within such moving habitats to discern between populations at high and low risk of extinction. We introduce a system of reaction–diffusion equations to study the impact of varying shifting speeds on the persistence and distribution of a single species. Our model includes habitat dependent movement behaviour and habitat preference of individuals. These assumptions result in a jump in density across habitat types and generalize previous studies. We build and validate a numerical finite difference scheme to solve the resulting equations. Our numerical scheme uses a coordinate system where the location of the moving suitable habitat is fixed in space and a modification of a finite difference scheme to capture the jump in density. We explore a variety of shifting-speed scenarios and contribute insights into the mechanisms that support population persistence through time in shifting habitats. One common finding is that a strong bias for the suitable habitat helps the population persist at faster shifting speeds, yet sustains a smaller total population at slower shifting speeds.

1. Introduction

For the past decades, climate change has been identified as a major contributor to species extinction and range shifts; see for example [1–8]. A range shift occurs when a species' geographical range (in the sense of where the species is found) moves, for example in response to optimal temperature ranges moving in space. Observed range shifts as a result of climate change indicate that some species are able to follow their suitable habitat as it shifts with the warming climate. Whether a population can do this in the long run is unknown. How the temperature regime shifts is location and time dependent. Studies show that at different elevations warming occurs at different rates [9–11], and that ocean temperatures are warming at accelerating rates [12]. We propose a mathematical model that can capture the effects of temporally and spatially varying speeds of climate change on population dynamics.

A habitat "edge" indicates the location where two habitat types meet, for example, where the preferred temperature regime ends, where a forest meets farmland, or where a field of host-specific foliage ends. Many species adjust their movement behaviour according to habitat characteristics. The Fender's blue butterfly (*Icaricia icarioides fenderi*), which are host-specific to the Kincaid's lupine (*Lupinus sulphureus spp. kincaidii*), bias their movement towards their host plant when near habitat edges [13]. The planthopper *Prokelisia crocea* moves faster and spends less time in mudflat habitat than in brome and cordgrass habitats [14].

In mathematical models, preferential movement and/or habitat quality dependent diffusion rates introduce a jump in density across interfaces representing habitat edges [15,16]. When such individual movement behaviour is included in mathematical models of population dynamics over heterogeneous environments, persistence and extinction outcomes change [16,17]. We include individual movement behaviour into our mathematical model by making dispersal rates dependent on habitat type and by considering preferential movement behaviour when an individual is at a habitat edge.

Mathematical models for population dynamics in climate-driven moving habitats are called *moving-habitat models*. Commonly, these models describe dispersal and population dynamics in one dimension, where the location of the suitable habitat shifts in one direction along the real line. The suitable habitat is determined by a positive intrinsic growth rate. This approach started in the reaction–diffusion framework where, among many results, the authors presented coexistence and invasion analysis of two competing species [18]. This work was followed by a single species model [19], where the authors proved the existence of travelling wave type solutions. Since these two pioneering works, research on moving-habitat models has continued in the reaction–diffusion equation framework [17,20–32] and

* Corresponding author.
E-mail addresses: [redacted] (J.S. MacDonald), [redacted] (Y. Bourgault), [redacted] (F. Lutscher).

https://doi.org/10.1016/j.mbs.2021.108711
Received 3 May 2021; Received in revised form 9 September 2021; Accepted 9 September 2021
Available online 20 September 2021
0025-5564/© 2021 Elsevier Inc. All rights reserved.

expanded to integrodifference equations [33–41], integrodifferential equations [42–47] and lattice equations [48–50]. Most analyses focus on the asymptotic outcome for the population density; we consider transient phenomena.

Most studies of moving-habitat models assume that the speed of the shift, denoted by c, is constant. With this assumption, a critical speed of the shift, c^*, exists. In many studies, c^* represents a threshold speed, above which a population will eventually go extinct; see for example [19,29,32,37]. When habitat-dependent movement behaviour and habitat preference is included, c^* is a weak threshold in the sense that a population can persist for $c > c^*$ given that certain conditions are met [17]. In the reaction–diffusion framework, c^* is related to the Fisher speed [51], the asymptotic speed at which a population invades an infinite homogeneous habitat.

Few models include nonconstant speeds of climate change, namely integrodifference equations with accelerating, [52] and stochastic speeds [34], and integrodifferential equations or reaction–diffusion equations with periodic speeds; see for example [29,47]. Some authors study models in which there is a single interface that separates two semi-infinite habitats of different quality; see for example [22,23,42,49]. Depending on the direction in which this interface moves, the suitable habitat shrinks or expands. In our model, we consider a bounded suitable habitat and make no assumption on the speed or direction in which the bounds of the suitable habitat are moving. These generalities on the moving suitable habitat together with the jumps in density across habitat edges necessitate a numerical approach.

Many authors provide numerical simulations of the population dynamics to illustrate their results [23,28,33,35,37,39,40,42,46]. Yet, none of these simulations include the individual movement behaviour as described above so that they do not face the numerical challenge of capturing jumps in density across interfaces. Moreover, their focus is not on the numerical method. Moving domains and interfaces are present in multiple ecological and physical processes [53]. The complex equations governing these phenomena usually require numerical approaches to obtain solutions. For instance, free-boundary problems require the numerical tracking of a boundary whose motion is prescribed by an ordinary differential equation; for an example in ecology see [54]. Numerical methods are a common approach to address growing domains or deforming boundaries in pattern formation, cellular biology and fluid dynamics; see for example [55–58].

Numerical schemes to treat these time-dependent domains vary and heavily depend on the model dynamics. One approach is to use adaptive or moving meshes by defining a mapping that reformulates the model over a fixed spatial domain (e.g. [55–57,59,60]). The computations are performed in the fixed domain and the inverse mapping gives the solution over the original coordinate system. There are multiple ways to define such a mapping; we refer the reader to [58, 61]. Our mapping fixes the interfaces in space but in turn introduces time-dependent coefficients.

A numerical scheme can either be interface conformal (e.g. [62]) or nonconformal (e.g. [54,63,64]). Nonconformal methods require interpolation to solve for the solution around an interface. Conformal methods require the mesh to adjust to the moving interface, with some grid points falling exactly on the interface at each time step. In our model, the location of the interfaces are explicitly given and we exploit this fact in our numerical scheme by defining our reference frame so that the grid points conform to the interface. A conformal method guarantees accuracy near the interface to capture the jump in density.

This paper is organized as follows. In Section 2.1, we introduce our moving-habitat model in the form of a reaction–diffusion system similar to [17]. Our model has two sharp interfaces bounding the suitable habitat, and we include individual movement behaviour as discussed above. We allow the interfaces to move in any direction and at any speed, so long as the suitable habitat has positive length. In Section 2.2, we introduce a time dependent mapping from the coordinate system of the generalized model to a coordinate system in which the moving interfaces are fixed in space. In Section 2.3, we study the shape of the density profile of the travelling pulse solution for the analytically tractable system proposed in [17]. In Sections 3 and 4, we introduce a numerical scheme to study the complex scenarios of our generalized model and we validate this scheme numerically using two test cases from [17]. In Section 5, we present three numerical applications: (1) The two interfaces move at constant matching speeds; (2) The two interfaces move at constant nonmatching speeds; and (3) The interfaces move at accelerating speeds. In all three cases, we give insights into the mechanisms that impact the population outcome (persistence vs extinction). Finally, in Section 6, we discuss the limitations of our scheme and the ecological implications, and we give suggestions for future research directions.

2. The model

2.1. General model

We study the dynamics of a single species inhabiting a moving patch of suitable habitat surrounded by unsuitable habitat. We model the population dynamics in time with a reaction–diffusion equation on the real line. A bounded interval, $\Omega_0 = \Omega_0(t)$, represents the suitable habitat. Its size and location may change in time (t) to represent the impact of climate change. The half-lines on either side of Ω_0 represent unsuitable habitat. The edges of the suitable habitat are indicated by the two points $L_i = L_i(t)$, $i = 1, 2$, which we refer to as interfaces. We assume that for all $t \in [0, T)$, $\Omega_0(t) = \big(L_1(t), L_2(t)\big)$ is nonempty. This is a natural assumption, since an empty Ω_0 corresponds to the absence of a suitable habitat. We refer to L_1 as the trailing edge and L_2 as the leading edge. We choose this labelling since all our applications assume that the suitable habitat shifts in the positive direction.

We denote by $u = u(x, t)$ the population density over space (x) and time. We denote partial derivatives with subscripts. The general form of our system of equations is

$$u_t = d_0 u_{xx} + u(r - au), \qquad L_1(t) < x < L_2(t), \tag{1a}$$

$$u_t = d_1 u_{xx} - m_1 u, \qquad x < L_1(t), \tag{1b}$$

$$u_t = d_2 u_{xx} - m_2 u, \qquad x > L_2(t), \tag{1c}$$

with interface conditions

$$u(L_1(t)^+, t) = k^\alpha u(L_1(t)^-, t) \tag{1d}$$

$$\big(d_0 u_x + L_1'(t)u\big)\,(L_1(t)^+, t) = \big(d_1 u_x + L_1'(t)u\big)\,(L_1(t)^-, t), \tag{1e}$$

and

$$u(L_2(t)^-, t) = k^\beta u(L_2(t)^+, t), \tag{1f}$$

$$\big(d_0 u_x + L_2'(t)u\big)\,(L_2(t)^-, t) = \big(d_2 u_x + L_2'(t)u\big)\,(L_2(t)^+, t), \tag{1g}$$

where

$$k^\alpha = \frac{\alpha}{1-\alpha}\sqrt{\frac{d_1}{d_0}}, \qquad k^\beta = \frac{\beta}{1-\beta}\sqrt{\frac{d_2}{d_0}}, \tag{1h}$$

and asymptotic conditions at infinity

$$\lim_{x \to \pm\infty} u(x, t) = 0. \tag{1i}$$

Here, d_i are the diffusion rates in the different parts of the habitat and m_i are the mortality rates in the unsuitable parts. Growth in the suitable habitat is logistic, where r is the intrinsic growth rate and a is the intraspecific competition coefficient. Eqs. (1d) and (1f) state that across each interface, there is a jump in density, which represents individual movement behaviour at an interface (see Section 1) with proportionality constants given in (1h). These terms can be derived from an individual-level random walk description of the movement behaviour at an interface; see [15,16] for details. Parameter α (β) is the probability of an individual at the trailing (leading) edge moving into

the suitable habitat. The values k^α and k^β are nondimensional quantities. Eqs. (1e) and (1g) imply that the population flux is continuous across each interface so that the total population density is conserved in the absence of the reaction term. The term $L_i'(t)u$ in these equations arises from the continuous movement of the interfaces in time [17]. The limit conditions (1i) are necessary for uniqueness of solutions and to ensure that solutions stay bounded. The assumption that solutions approach zero far away from $\Omega_0(t)$ is reasonable since the further away an individual is from the suitable habitat the less likely it is to survive.

To reduce the number of parameters, we nondimensionalize the equations by taking

$$X = \sqrt{\frac{r}{d_0}}x, \quad T = rt, \quad \text{and} \quad U = \frac{a}{r}u.$$

This transformation scales d_0, r and a to unity. We set $d_i' = d_i/d_0$, $m_i' = m_i/r$, and $\Gamma_i(T) = \sqrt{\frac{r}{d_0}}L_i\left(\frac{T}{r}\right)$, and the system may be written as

$$U_T = U_{XX} + U(1-U), \qquad \Gamma_1(T) < X < \Gamma_2(T), \tag{2a}$$

$$U_T = d_1'U_{XX} - m_1'U, \qquad X < \Gamma_1(T), \tag{2b}$$

$$U_T = d_2'U_{XX} - m_2'U, \qquad X > \Gamma_2(T), \tag{2c}$$

with interface matching conditions

$$U\left(\Gamma_1^+(T),T\right) = k^\alpha U\left(\Gamma_1^-(T),T\right), \tag{2d}$$

$$\left(U_X + \Gamma_1'(T)U\right)\left(\Gamma_1^+(T),T\right) = \left(d_1'U_X + \Gamma_1'(T)U\right)\left(\Gamma_1^-(T),T\right), \tag{2e}$$

and

$$U\left(\Gamma_2^-(T),T\right) = k^\beta U\left(\Gamma_2^+(T),T\right), \tag{2f}$$

$$\left(U_X + \Gamma_2'(T)U\right)\left(\Gamma_2^-(T),T\right) = \left(d_2'U_X + \Gamma_2'(T)U\right)\left(\Gamma_2^+(T),T\right), \tag{2g}$$

where

$$k^\alpha = \frac{\alpha}{1-\alpha}\sqrt{d_1'}, \qquad k^\beta = \frac{\beta}{1-\beta}\sqrt{d_2'}. \tag{2h}$$

The conditions at infinity remain unchanged.

We work with system (2), however, we write $x = X$, $t = T$, $u = U$, and we drop all prime notations.

2.2. The reference frame

The movement of the interfaces over the real line complicates both the analysis of the system and any numerical scheme to solve this problem. To circumvent these difficulties, we define a mapping from $\mathbb{R}\times[0,T)$ to $\mathbb{R}\times[0,T)$, denoted

$$\phi : (x,t) \mapsto (y(x,t),t),$$

such that for each $t \in [0,T)$, $y(\cdot,t)$ is a C^1–diffeomorphism from $\mathbb{R}\to\mathbb{R}$. We impose on $y = y(x,t)$ the condition that

$$\tilde{\Gamma}_1 = y(\Gamma_1(t),t), \quad \text{and} \quad \tilde{\Gamma}_2 = y(\Gamma_2(t),t)$$

are fixed in the y-coordinate system for all time and that this transformation is orientation preserving. Since $y(\cdot,t)$ is a C^1–diffeomorphism, the inverse mapping $x(\cdot,t)$ is differentiable. We further assume that $x(y,\cdot)$ is differentiable. The set of points y defined by the mapping ϕ is called the reference frame. The reference frame is of particular importance because we analyse the model and define the numerical scheme over the y-coordinate system. Solutions are presented after mapping back to the x-coordinate system, which we refer to as the physical frame.

Without loss of generality, we assume that $\Gamma_1(0) = 0$, then $\Gamma_2(0) = L > 0$. For $\Gamma_i(t) \in C^1[0,T)$, a continuously differentiable function that satisfies the above conditions is

$$y(x,t) = L\frac{x-\Gamma_1(t)}{\Gamma_2(t)-\Gamma_1(t)}. \tag{3}$$

The mapping ϕ is well-defined and invertible ($\partial y(x,t)/\partial x \neq 0$) whenever the denominator of (3) is non-zero. The inclusion of L in (3) is not necessary, yet it fixes the right-most interface at $y = L$ and sets the patch size as a parameter in the model.

The transformation (3) is certainly not the only option. However, as in this transformation, from hereon we assume that $x = x(\cdot,t)$ is affine.

We set $\tilde{u}(y,t) = u(x(y,t),t)$ and denote partial derivatives of x with subscripts. The population dynamics in the reference frame are

$$\tilde{u}_t = \frac{1}{x_y^2}\tilde{u}_{yy} + \frac{x_t}{x_y}\tilde{u}_y + \tilde{u}(1-\tilde{u}), \qquad y \in \tilde{\Omega}_0, \tag{4a}$$

$$\tilde{u}_t = \frac{d_1}{x_y^2}\tilde{u}_{yy} + \frac{x_t}{x_y}\tilde{u}_y - m_1\tilde{u}, \qquad y \in \tilde{\Omega}_1, \tag{4b}$$

$$\tilde{u}_t = \frac{d_2}{x_y^2}\tilde{u}_{yy} + \frac{x_t}{x_y}\tilde{u}_y - m_2\tilde{u}, \qquad y \in \tilde{\Omega}_2, \tag{4c}$$

where

$$\tilde{\Omega}_0 = \{y \in \mathbb{R} \mid \tilde{\Gamma}_1 < y < \tilde{\Gamma}_2\}, \tag{4d}$$

$$\tilde{\Omega}_1 = \{y \in \mathbb{R} \mid y < \tilde{\Gamma}_1\}, \tag{4e}$$

$$\tilde{\Omega}_2 = \{y \in \mathbb{R} \mid y > \tilde{\Gamma}_2\}, \tag{4f}$$

with matching interface conditions

$$\tilde{u}\left(\tilde{\Gamma}_1^+,t\right) = k^\alpha\tilde{u}\left(\tilde{\Gamma}_1^-,t\right), \tag{4g}$$

$$\left(\frac{\tilde{u}_y}{x_y} + \Gamma_1'(t)\tilde{u}\right)\left(\tilde{\Gamma}_1^+,t\right) = \left(d_1\frac{\tilde{u}_y}{x_y} + \Gamma_1'(t)\tilde{u}\right)\left(\tilde{\Gamma}_1^-,t\right), \tag{4h}$$

and

$$\tilde{u}\left(\tilde{\Gamma}_2^-,t\right) = k^\beta\tilde{u}\left(\tilde{\Gamma}_2^+,t\right), \tag{4i}$$

$$\left(\frac{\tilde{u}_y}{x_y} + \Gamma_2'(t)\tilde{u}\right)\left(\tilde{\Gamma}_2^-,t\right) = \left(d_2\frac{\tilde{u}_y}{x_y} + \Gamma_2'(t)\tilde{u}\right)\left(\tilde{\Gamma}_2^+,t\right). \tag{4j}$$

The conditions at infinity remain unchanged.

This transformation introduces into Eqs. (4a)–(4c) an advective component with velocity

$$v = \frac{x_t}{x_y}. \tag{5}$$

2.3. Steady state profiles in the reference frame

Almost all existing moving-habitat models consider the scenario that the trailing and leading edge are travelling at a constant matching speed; see Section 1. Under the assumption of constant matching speeds, the location of the interfaces in the physical frame can be described as $\Gamma_1(t) = ct$ and $\Gamma_2(t) = L + ct$. The transformation (3) becomes $y = x - ct$, which sets $\tilde{\Omega}_0 = (0,L)$. The system in the reference frame is

$$\tilde{u}_t = \tilde{u}_{yy} + c\tilde{u}_y + \tilde{u}(1-\tilde{u}), \qquad y \in \tilde{\Omega}_0, \tag{6a}$$

$$\tilde{u}_t = d_1\tilde{u}_{yy} + c\tilde{u}_y - m_1\tilde{u}, \qquad y \in \tilde{\Omega}_1, \tag{6b}$$

$$\tilde{u}_t = d_2\tilde{u}_{yy} + c\tilde{u}_y - m_2\tilde{u}, \qquad y \in \tilde{\Omega}_2, \tag{6c}$$

with matching interface conditions

$$\tilde{u}\left(0^+,t\right) = k^\alpha\tilde{u}\left(0^-,t\right), \tag{6d}$$

$$\left(\tilde{u}_y + c\tilde{u}\right)\left(0^+,t\right) = \left(d_1\tilde{u}_y + c\tilde{u}\right)\left(0^-,t\right), \tag{6e}$$

and

$$\tilde{u}\left(L^-,t\right) = k^\beta\tilde{u}\left(L^+,t\right), \tag{6f}$$

$$\left(\tilde{u}_y + c\tilde{u}\right)\left(L^-,t\right) = \left(d_2\tilde{u}_y + c\tilde{u}\right)\left(L^+,t\right). \tag{6g}$$

System (6) reduces to models that have been studied before [18,19] under the assumption that diffusion coefficients across all three regions are the same, i.e., $d_i = 1$, and there is no bias for either habitat type, i.e., $\alpha = \beta = 0.5$. Under these assumptions, $k^\alpha = k^\beta = 1$. These studies show that for every $c < c^* = 2$ there exists a *critical patch-size* $L^* > 0$,

such that for every $L \geq L^*$ a positive steady state solution to (6) exists. Its profile is hump shaped with the maximum occurring inside $\tilde{\Omega}_0$. In the physical frame, this solution is a travelling pulse.

We study a generalized model by including habitat-dependent diffusion rates and preferential movement behaviour. Persistence conditions for system (6), characterized by instability of the trivial steady state, were studied in detail in [17]. A positive steady state solution for system (6) translates into a travelling pulse solution in the physical frame. We expect, due to the monotone properties of the system, that if the trivial steady state is unstable, a unique and stable positive solution exists. Here, we characterize the shape of the travelling pulse. The sign of the slope of the profile to the right of Γ_1 is equal to the sign of $\gamma_0^\alpha - c$ [17], where

$$\gamma_0^\alpha = \frac{c + \sqrt{c^2 + 4m_1 d_1}}{2k^\alpha}.$$

Proposition 1.

1. *If $k^\alpha \leq 1$, then $\gamma_0^\alpha - c > 0$.*
2. *If $k^\alpha > 1$, then the sign of $\gamma_0^\alpha - c$ is equal to the sign of $q := \frac{m_1 d_1}{k^\alpha(k^\alpha - 1)} - c^2$.*

Proof. A partial differential equation on a bounded domain can be associated to system (6) on the reference frame [17]. This problem takes the form

$$\begin{aligned} &u_t = u_{yy} + cu_y + u(1-u), && (y,t) \in \tilde{\Omega}_0 \times \mathbb{R}^+, \\ &u_y + cu = \gamma_0^\alpha u, && \text{at } y = 0, \\ &u_y + cu = \gamma_0^\beta u, && \text{at } y = L, \end{aligned} \tag{7}$$

where $\gamma_0^\beta = \frac{c - \sqrt{c^2 + 4m_2 d_2}}{2k^\beta}$. The system on the bounded domain is not equivalent to the original problem (6). Yet, stability of steady state solutions of the boundary-value problem (7) and the problem on the reference frame (6) are equivalent and these steady state solutions coincide inside the bounded domain [17].

We have that

$$\gamma_0^\alpha - c = \frac{c(1-2k^\alpha) + \sqrt{c^2 + 4m_1 d_1}}{2k^\alpha}.$$

The sign of $\gamma_0^\alpha - c$ is determined by the sign of the numerator of the above expression. When $k^\alpha \leq 1$, the numerator is positive since in this case $|1 - 2k^\alpha| \leq 1$. When $k^\alpha > 1$, then

$$c(1-2k^\alpha) + \sqrt{c^2 + 4m_1 d_1} > 0 \iff \frac{m_1 d_1}{k^\alpha(k^\alpha - 1)} > c^2. \quad \square$$

This novel result states that the maximum of the density can occur on the left interface rather than inside Ω_0.

The slope to the left of Γ_2 is always negative. Furthermore, when c is greater than the critical speed $c^* = 2$, a finite critical patch-size exists only when $k^\alpha > \bar{k}^\alpha = \frac{c + \sqrt{c^2 + 4m_1 d_1}}{c - \sqrt{c^2 - 4}}$ [17].

Corollary 2. *When $q < 0$, the steady state solution of (6) is a decreasing function for all $y > \tilde{\Gamma}_1$, except possibly at $y = \tilde{\Gamma}_2$, where a jump may occur. Moreover, when $c \geq 2$ and $k^\alpha > \bar{k}^\alpha$, then $q < 0$.*

Proof. The steady state solution inside $\tilde{\Omega}_0$ coincides with the solution to the steady state of (7). Since u_y evaluated on both boundaries is negative, we have a local maximum and local minimum at $y = 0$ and $y = L$, respectively. Thus, if a local maximum occurs in $\tilde{\Omega}_0$, it must occur after a local minimum. At local extrema inside $\tilde{\Omega}_0$ necessarily $u_y = 0$, so that at a steady state we have $u_{yy} + u(1-u) = 0$. Hence, a local minimum (maximum) can occur only when $u > 1$ ($u < 1$). This proves that no local extrema occur inside $\tilde{\Omega}_0$.

Necessarily, $\bar{k}^\alpha > 2$ [17] . Thus, if a steady state solution exists, $k^\alpha > 2$ and case (2) of Proposition 1 applies. So we have

$$k^\alpha > \bar{k}^\alpha = \frac{c + \sqrt{c^2 + 4m_1 d_1}}{c - \sqrt{c^2 - 4}} \iff \left(c - \sqrt{c^2 - 4}\right) k^\alpha > c + \sqrt{c^2 + 4m_1 d_1}.$$

Thus

$$2ck^\alpha > c + \sqrt{c^2 + 4m_1 d_1} \iff c(2k^\alpha - 1) > \sqrt{c^2 + 4m_1 d_1}.$$

Therefore, from the proof of case (2) of Proposition 1, $\gamma_0^\alpha - c < 0$. $\square$

In the physical frame for $x > \Gamma_1(t)$ (except possibly at $x = \Gamma_2(t)$) the density may be decreasing when the speed is below the threshold, and will be decreasing when the speed is above the threshold. All of these cases are illustrated in Fig. 1.

3. The numerical scheme

We introduce a finite difference scheme where all the computational effort is focused on the reference frame, i.e., a scheme to solve system (4). A main and non-standard ingredient of our scheme is the duplication of the nodal values on the interfaces $\tilde{\Gamma}_i$. This duplication allows our numerical scheme to capture the discontinuities across these interfaces. We discretize the flux conditions (4h) and (4j) with a three-point one-sided limit difference equation. The spatial grid is not necessarily uniform.

We truncate the infinite domain by taking the left and right computational endpoints as $y_{-\infty} = -a_1 L$ and $y_\infty = (a_2 + 1)L$, for some $a_i > 0$ large enough. We denote the three computational subdomains by $\tilde{\Omega}_1 = (y_{-\infty}, 0)$, $\tilde{\Omega}_0 = (0, L)$, and $\tilde{\Omega}_2 = (L, y_\infty)$. We denote by y_j the grid points, by p_i the number of grid points within the closure of each $\tilde{\Omega}_i$, and by $p = p_0 + p_1 + p_2$ the total number of grid points. We set $y_{j+1} = y_j + h_j$, where each $h_j > 0$, with the exception that $h_{p_1} = 0 = h_{p_1 + p_0}$, so that two grid points lie on each interface (Fig. 2). We denote by $U_j(t)$, $j = 1, \ldots, p$ the semi-discretized (in space) approximation of $u(x_j, t)$.

An upwind scheme controls any instability that may result from the advective component [65]. The upwind direction depends on the sign of the advective velocity, $v = v(y_j, t)$, given in Eq. (5). Thus, inside $\tilde{\Omega}_i$, we approximate the first-order spatial derivative by

$$vu_y(y_j, t) \approx \min(0, v_j)\frac{U_j - U_{j-1}}{h_{j-1}} + \max(0, v_j)\frac{U_{j+1} - U_j}{h_j}. \tag{8}$$

We approximate the second-order spatial derivative by

$$u_{yy}(y_j, t) \approx \frac{h_j U_{j-1} - (h_{j-1} + h_j)U_j + h_{j-1}U_{j+1}}{h_j^2 h_{j-1}}. \tag{9}$$

With these approximations, the semi-discrete scheme within each $\tilde{\Omega}_i$ is

$$\begin{aligned} (U_j)_t = &\left(\frac{d_i}{x_y^2 h_j h_{j-1}} - \frac{\min(0, v_j)}{h_{j-1}}\right) U_{j-1} \\ &+ \left(\frac{\min(0, v_j)}{h_{j-1}} - \frac{\max(0, v_j)}{h_j} - \frac{d_i\left(h_{j-1} + h_j\right)}{x_y^2 h_j^2 h_{j-1}}\right) U_j \\ &+ \left(\frac{d_i}{x_y^2 h_j^2} + \frac{\max(0, v_j)}{h_j}\right) U_{j+1} + F_j, \qquad y_j \in \Omega_i, \end{aligned} \tag{10}$$

where $d_0 = 1$ and

$$F_j = \begin{cases} U_j(1 - U_j), & y_j \in \Omega_0, \\ -m_i U_j, & y_j \in \Omega_{1,2}. \end{cases}$$

We discretize the time derivative with the semi-implicit forward–backward Euler (FBE) method, where the linear advection and diffusion terms are taken implicitly and all nonlinear reaction terms are taken explicitly. Thereby, we avoid solving a nonlinear equation and instead solve a linear system at each time step [66]. We denote the time step by τ and the approximation of $u(y_j, n\tau)$ by U_j^n. We set $U^n = \left[U_1^n, \ldots, U_p^n\right]^T$.

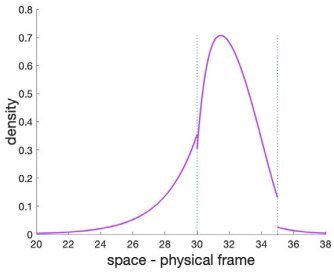

(a) Parameters are $c = 1$, $d_1 = 4$, $d_2 = 5$, $m_i = 1.4$, $\alpha = 0.3$, and $\beta = 0.7$. Here $k^\alpha \approx 0.8571$, thus the density has a maximum inside Ω_0.

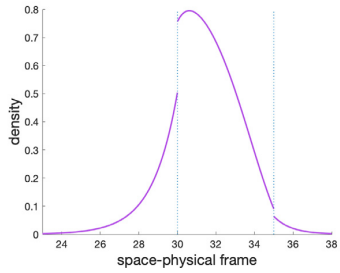

(b) Parameters are $c = 1$, $d_1 = 1$, $d_2 = 2$, $m_i = 1.4$, $\alpha = 0.6$, and $\beta = 0.5$. Here $k^\alpha = 1.5$ and $q \approx 0.8667$, thus the density has a maximum inside Ω_0.

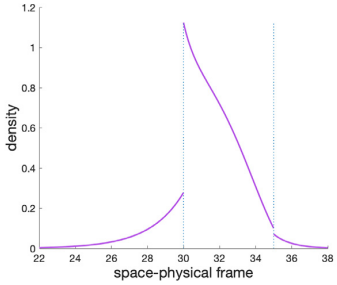

(c) Parameters are $c = 1$, $d_1 = 3$, $d_2 = 2$, $m_1 = 1.4$, $m_2 = 1.1$, $\alpha = 0.7$, and $\beta = 0.5$. Here $k^\alpha \approx 4.0415$ and $q \approx -0.6583$, thus the solution is decreasing for $y > \Gamma_1(t)$.

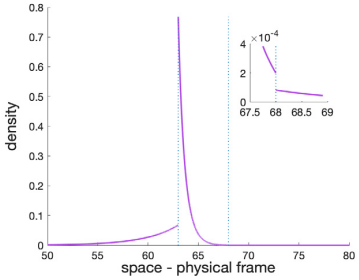

(d) Parameters are $c = 2.1$, $d_1 = 8$, $d_2 = 6$, $m_i = 1.4$, $\alpha = 0.8$, and $\beta = 0.5$. Here $c > 2$, thus the solution is decreasing for $y > \Gamma_1(t)$. The jump at Γ_2 is shown in the overlaid figure.

Fig. 1. Plots of the solution in the travelling pulse state of system (2) with $\Gamma_1(t) = ct$ and $\Gamma_2(t) = 5 + ct$ for various model parameters. The vertical dotted lines represent the location of the interfaces.

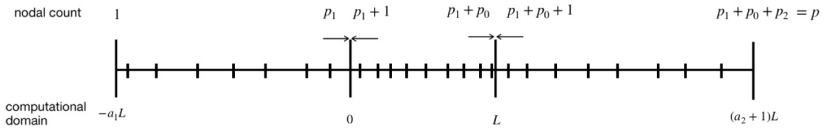

Fig. 2. An illustration of the computational spatial domain.

We account for the interface conditions (4h) and (4j) by discretizing the right- and left-sided limits of u_y as

$$u_y(y_j^\pm, t) \approx \mp \frac{(2\delta_1^\pm + \delta_2^\pm)}{\delta_1^\pm(\delta_1^\pm + \delta_2^\pm)} U_j \pm \frac{\delta_1^\pm + \delta_2^\pm}{\delta_1^\pm \delta_2^\pm} U_{j\pm1} \mp \frac{\delta_1^\pm}{\delta_2^\pm(\delta_1^\pm + \delta_2^\pm)} U_{j\pm2}, \tag{11}$$

where $\delta_1^+ = h_j$, $\delta_2^+ = h_{j+1}$, $\delta_1^- = h_{j-1}$, and $\delta_2^- = h_{j-2}$. We assign homogeneous Neumann boundary conditions at the computational endpoints and discretize with one-sided first-order differences. The interface conditions and the Neumann conditions are taken at time $t_{n+1} = \tau(n+1)$. The FBE method is then

$$\mathbf{M}\frac{U^{n+1} - U^n}{\tau} = A^{n+1}U^{n+1} + \mathbf{F}^n, \tag{12}$$

where A is the $p \times p$ time-dependent matrix obtained from Eqs. (10)–(11) together with the interface equations and Neumann boundary conditions. The matrix $\mathbf{M} = \{m_{ij}\}$ is a diagonal matrix with $m_{jj} = 0$, if y_j is a boundary point of $\tilde{\Omega}_i$, and $m_{jj} = 1$, otherwise. The vector $\mathbf{F} = \left[F_1, \ldots, F_p\right]^T$, where $F_j = 0$, for all y_j on the boundaries of $\tilde{\Omega}_i$. In applications, the linear terms of $\mathbf{F}$ are included inside A for better stability of the semi-implicit time stepping method. This scheme is first order in both space and time.

4. Validation of the numerical scheme

We focus on the impact of the numerical parameters on the accuracy of the numerical solution. We consider system (6) to build our test cases and validate our scheme. We focus on two parameter sets, denoted by S_1 and S_2, corresponding to Figs. 1(b) and 1(d), respectively. These parameter sets are both biologically and numerically interesting. Both parameter sets incorporate differing diffusion rates across habitat types and biases for the suitable habitat. Varying these parameters can change the shape of the steady state profile; see Section 2.3. The parameter set S_1 results in the density profile having a maximum in the interior of Ω_0 close to the interface Γ_1. This scenario occurs when α and d_1 are large but not large enough to make $q < 0$. To capture such humps

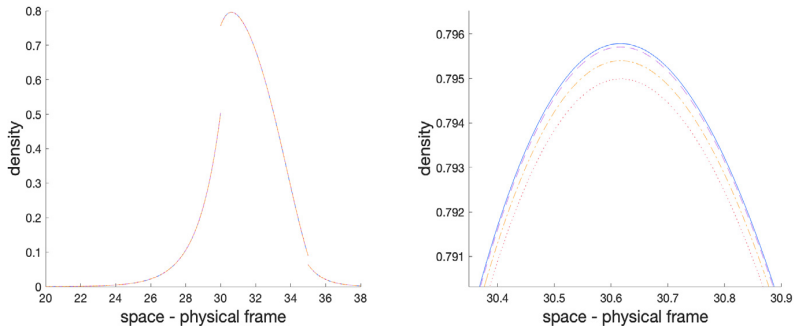

(a) (b)

Fig. 3. Plots of the solution in the travelling pulse state of system (2) with $\Gamma_1(t) = ct$ and $\Gamma_2(t) = 5 + ct$ for parameter set S_1 over uniform grids with $h = 2.0 \times 10^{-2}$, (dotted in red), $h = 1.0 \times 10^{-2}$, (dash-dotted in orange), $h = 2.5 \times 10^{-3}$, (dashed in purple). The total number of grid points is $p = 2754,\ 5502,\ 22002$, respectively. The reference solution is plotted as solid in blue. Panel 3(a): The numerical solutions over various grids are superimposed over the reference solution. Panel 3(b): The hump is where the largest error occurs. The numerical solutions converge to the reference solution.

accurately partially motivated the use of a three-point discretization of the flux interface conditions. The parameter set S_2 results in the density profile having a maximum on the interface Γ_1 followed by a steep gradient. This gradient becomes steeper with larger values of c. Such large gradients motivated the use of both the semi-implicit method and a three-point discretization of the flux interface conditions.

The proposed method was implemented in MATLAB®. All test cases were run on a Dell Optiplex 5040 with 4 Intel Core i5-6500 CPU @ 3.20GH processors and 7.7 GiB of memory on a Ubuntu 18.04.5 LTS 64-bit operating system.

For both parameter sets, we take the initial condition equal to a Gaussian curve centred within the suitable habitat, namely

$$u(x,0) = \sqrt{\frac{2}{\pi}} \exp\left(-2(x-2.5)^2\right).$$

For each parameter set, we numerically compute a reference solution over a very fine grid. We compute the reference solution for S_1 over a uniform grid with a spatial step of $h_j \equiv h = 6.25 \times 10^{-4}$, and a total number of $p = 88004$ grid points. We define the computational domain by setting $a_i = 5$, so that $[y_{-\infty}, y_{\infty}] = [-25, 30]$. This size of computational domain limits the impact of a truncated domain at infinity as assessed by a flat solution near the exterior boundaries. For S_2, we compute the reference solution over a uniform grid inside $\tilde{\Omega}_0$ with $h_j \equiv h_0 = 7.8125 \times 10^{-5}$, and a nonuniform grid inside $\tilde{\Omega}_i$, $i = 1, 2$. Inside $\tilde{\Omega}_i$, $i = 1, 2$, we space the grid geometrically with the smallest cell width $h = h_0$ occurring next to the respective interface $\tilde{\Gamma}_i$ and geometrically increasing away from the interfaces with a common ratio of $r = 1.001$. In this case, the total number of grid points is $p = 76726$. We set $a_i = 9$ so that $[y_{-\infty}, y_{\infty}] \approx [-45, 50]$. We compute both reference solutions at time $T = 30$, as by this time the numerical solutions have passed through transient stages and reached steady state. For both cases, we denote the reference solution as U_{ref}.

We denote by $\hat{U}_h^N$ the numerical solution after N time steps with h as the cell width within $\tilde{\Omega}_0$. We check the accuracy of our solutions at time $T = N\tau = 30$ using the following relative error:

$$e_\infty(\hat{U}_h^N) = \frac{\|\hat{U}_h^N - U_{\text{ref}}\|_\infty}{\|U_{\text{ref}}\|_\infty}, \tag{13}$$

where $\|V\|_\infty = \sup_j |V_j|$, for $V \in \mathbb{R}^p$. For given model parameters, we consider a numerical solution accurate enough or *grid independent* if the relative error with respect to the reference solution is below 1%. To compute e_∞, we interpolate the reference solution onto the coarser grid using the spline function provided by MATLAB®, which is a cubic spline interpolation with not-a-knot end conditions.

For the validation of the scheme with respect to spatial resolution, we choose the time step $\tau = 0.1$, so that $N = 300$. For parameter set S_1, numerical solutions are grid independent even on coarse grids (Table 1). The largest error occurs at the hump of the profile (Fig. 3).

Table 1
Relative error between solutions on various spatial grids compared to the reference solution for parameter values S_1 on a uniform grid (top) and S_2 on a geometrically spaced grid (bottom).

Parameter set	h or h_0	Relative error	CPU time (s)
S1	2.0×10^{-2}	1.0×10^{-3}	0.12
	1.0×10^{-2}	4.9×10^{-4}	0.24
	2.5×10^{-3}	9.8×10^{-5}	1.43
S2	2.0×10^{-2}	1.8×10^{-1}	0.11
	5.0×10^{-3}	4.4×10^{-2}	0.52
	6.25×10^{-4}	4.9×10^{-3}	11.45

For parameter set S_2, numerical solutions are grid independent on more refined grids (within $\tilde{\Omega}_0$) than in the case of parameter set S_1 (Table 1). A finer grid within $\tilde{\Omega}_0$ is necessary due to the steep slope of the solution near Γ_1, particularly to the right of this interface. For too coarse a grid, the scheme overshoots the maximum value of U_{ref} (Fig. 4).

The FBE method is stable for time steps independent of the space step for a reaction–diffusion equation in a domain without interfaces [67]. Similarly, our scheme remains stable for a constant time step across various spatial grids, including nonuniform grids. For solutions with gradual slopes, as with S_1, the scheme is accurate for time steps at least as large as $\tau = 0.1$ (Fig. 5(a)). For solutions with steep slopes at the interface, as with S_2, the relative error can be between 3%–5% (Fig. 5(b)) for transient times but falls well below 1% as the solution reaches the travelling pulse state. Consequently, $\tau = 0.1$ was deemed to be small enough for obtaining qualitatively reliable solutions in the most difficult cases and quantitatively reliable solutions in the easiest ones.

Other parameter sets reach similar computational requirements. Furthermore, the profile of the numerical solution always coincides correctly with the proposition and corollary stated in Section 2.3.

5. Applications of the numerical method

We illustrate the power of our scheme with three applications. We start with the interfaces moving at constant matching speeds and study the impact of model parameters on the travelling pulse state. We then study the case of a growing suitable habitat. In this case, the interfaces move at constant nonmatching speeds. Finally, we study the scenario when the interfaces move at matching accelerating speeds. In the second application, the growing patch size prevents the existence

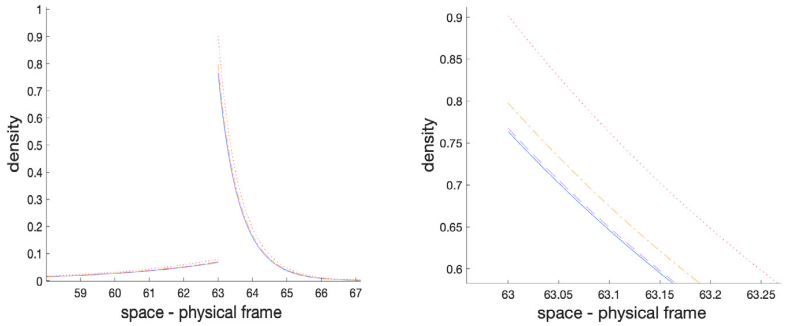

(a) (b)

Fig. 4. Plots of the solution in the travelling pulse state of system (2) with $\Gamma_1(t) = ct$ and $\Gamma_2(t) = 5 + ct$ and parameter set S_2 over geometric grids with $h_0 = 2.0 \times 10^{-2}$, (dotted in red), $h_0 = 5.0 \times 10^{-3}$ (dash-dotted in orange), $h_0 = 6.25 \times 10^{-4}$, (dashed in purple). The total number of grid points is $p = 2612,\ 5610,\ 16588$, respectively. The reference solution is plotted as solid in blue. Panel 4(a): The numerical solutions over various grids are superimposed over the reference solution, except for the larger deviation from the reference solution near the trailing edge. Panel 4(b): A close up of the curves to the right of Γ_1, where the largest error occurs. The numerical solutions converge to the reference solution.

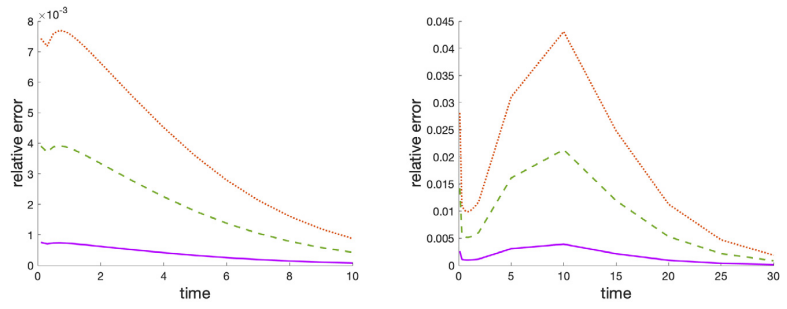

(a) (b)

Fig. 5. Plots of the relative error as a function of time. Curves correspond to time steps $\tau = 1.0 \times 10^{-1}$ (dotted in orange), $\tau = 5 \times 10^{-2}$ (dashed in green), and $\tau = 1.0 \times 10^{-2}$ (solid in purple). Panel 5(a) corresponds to parameter set S_1. The reference solution is computed with a time step of $\tau = 1.0 \times 10^{-3}$ and a uniform spatial grid with $h = 5.0 \times 10^{-3}$. Panel 5(b) corresponds to parameter set S_2. The reference solution is computed with a time step of $\tau = 1.0 \times 10^{-3}$ and a geometric spatial grid with $h_0 = 6.25 \times 10^{-4}$.

of a travelling pulse state; in the third application, it is the changing speed of the interfaces. In these applications, we focus on the transient dynamics and the impact of model parameters on these time-dependent solutions.

We refer to system (1) with stationary interfaces as the stationary system. We say that the range of a population is the largest interval within which the density exceeds a given threshold. This threshold value could correspond to a threshold above which a population is actually detectable in the field. The range is dependent on the threshold value chosen. The total population, denoted by $TP(t) = \sum_i \int_{\Omega_i} u(x,t)dx$, is the total population density over the whole computational domain. We denote by $TP_0(t)$ the total population density in the suitable habitat only. We calculate these values using the trapezoidal rule. The initial condition for every simulation run in this section was the steady state solution of the stationary system, with all relevant parameters being equal.

5.1. Constant matching speeds

When the speed of the interfaces is too large, the population will go extinct. Yet, for some intermediate speeds, both the total population and the range of the travelling pulse state can be larger than that of the steady state solution to the stationary system [19]. We consider once again system (6) and study some of the qualitative behaviour of the travelling-pulse solution. We find results similar to those in [19] and we contribute some insight into this unexpected phenomenon.

As in [19], we study the effect of the trailing mortality rate, m_1, on the total population. We denote by TP^* and TP_0^* the total population of the travelling pulse state over the whole computational domain and within the suitable habitat, respectively. We denote by TP^S the total population of the steady state solution of the stationary system.

As c increases from 0, TP^* can be much larger than TP^S and reaches a maximum at some $c \geq 0$ (Fig. 6(a)). The increase in TP^* is damped as m_1 increases. The individuals contributing to the increase in population size are found outside of the suitable habitat (Fig. 6(b)). The range of the travelling pulse state can be larger than that of the steady state solution for the stationary system (Fig. 7(a)). The largest part of the range is behind the suitable habitat (Fig. 7(b)). Since mortality there is relatively low, individuals die slowly and continue to contribute to TP^*. This group of individuals has been called a *Zombie Forest* in [68]. This study focused on the persistence of trees in a moving habitat and showed that Zombie Forests contribute positively to population persistence within the suitable habitat through seed dispersal. Following their terminology, we refer to the population in Ω_1 as the *zombie population.*

TP^* can be larger than TP^S due to a considerable bias for the suitable habitat. The strong bias helps individuals track the trailing interface and sustain a larger TP_0^* (Fig. 8(a), 8(b)). In this case, the range is a decreasing function of c (Fig. 8(c)). When this curve is flat, the range corresponds to the suitable habitat. In agreement with [17], larger values of α support population persistence at higher values of c. On the other hand, the range behind the suitable habitat is not as well populated. We only observed significant increases in TP_0^* for suitable habitat sizes closer to the critical patch-size.

We found that changing parameter values of diffusion did not significantly affect TP^*.

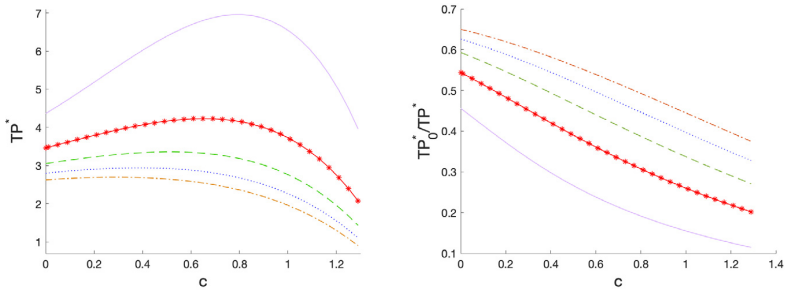

(a) (b)

Fig. 6. Illustrations of how the total population is impacted by c for $m_1 = 0.1$ (solid in purple), $m_1 = 0.2$ (star markers in red), $m_1 = 0.3$ (dashed in green), $m_1 = 0.4$ (dotted in blue), and $m_1 = 0.5$ (dash-dotted in orange). Other model parameters are set as $\alpha = \beta = 0.5$, $d_i = 1$, $m_2 = 1.4$, and $L = 3$. Panel 6(a): The total population as a function of c for various values of m_1. Panel 6(b): The ratio of the total population inside Ω_0 over the total population as a function of c for various values of m_1.

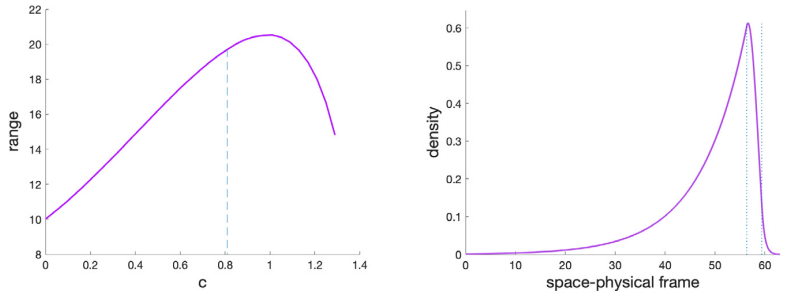

(a) (b)

Fig. 7. Panel 7(a) illustrates the range as a function of c for $m_1 = 0.1$. The dashed vertical line shows the range when $c = 0.81$. The range threshold is 0.1. Panel 7(b) illustrates the density profile of the travelling pulse when $c = 0.81$. The dashed vertical lines show the location of the interfaces.

5.2. Constant nonmatching speeds

Empirical evidence suggests that either edge may be moving faster than the other. Some studies found that at higher elevation, warming occurs at a faster rate [9,10]. This phenomenon is called elevation-dependent warming. If our bounded interval represents a patch on an altitudinal gradient, then the leading edge moves faster than the trailing edge. The opposite scenario, negative elevation-dependent warming, was reported in [11].

We describe habitat edges moving at constant nonmatching speeds by setting the interfaces in system (2) to be $\Gamma_1(t) = c_1 t$ and $\Gamma_2(t) = L + c_2 t$, for some positive c_i and L, and $c_1 \neq c_2$. Under these assumptions, the bounded interval either is growing ($c_1 < c_2$) or shrinking ($c_1 > c_2$).

We consider the case when $c_1 < c_2$ and study TP and the range as a function of time. The Fisher speed for the scaled model is $c^* = 2$; see Section 1. When $c_1 < c_2 < c^*$, we expect the population to persist in the growing domain. When $c^* < c_1 < c_2$, the persistence/extinction outcome is not as clear. We study three scenarios; We fix $c_2 = 3 > c^*$ and we take $c_1 = 1, 2, 2.5$, that is c_1 smaller, equal to and bigger than the Fisher speed.

When $c_1 < c^*$, TP, TP_0 and the range increase (Fig. 9). This increase is caused by the population profile developing an invasion front that travels at the Fisher speed in between the two interfaces (Fig. 10(a)). A weaker bias for the suitable habitat supports a larger population as a result of a larger zombie population (Fig. 9(a), 9(b)).

When $c_1 = c^*$, TP varies little while TP_0 first drops drastically, then has little variation (Fig. 9(a), 9(b)). The range initially increases, then decreases and, eventually, similar to TP and TP_0, varies little (Fig. 9(c)). The steady state solution of the stationary system with a weaker bias supports a larger population due to a larger zombie population and the carrying capacity of the suitable habitat. Yet, in this growing and moving habitat, a stronger bias eventually supports the larger total population (Fig. 9(a)). As time increases, the population profile seems to converge to a travelling pulse state, with the largest portion of the population clinging to the trailing edge (Fig. 10(b)). The weaker bias causes the drastic drop of the range (Fig. 9(c)), since the weaker bias sustains a larger zombie population. Initially, this population behind the trailing edge is hump shaped and the peak of the hump does not move in space. This hump flattens in time and when it drops below the range threshold, the range also drops (Fig. 10(b)).

When $c_1 > c^*$, TP tends to zero, and consequently so does TP_0 (Fig. 9(a), 9(b)). The range initially increases, but then decreases and eventually vanishes (Fig. 9(c)). The stronger bias causes the drastic collapse of the range. The bias assists the population in sticking to the trailing edge, yet due to the speed, a zombie population trails behind and the population density eventually falls below the range threshold. A weaker bias causes a more gradual collapse of the range (Fig. 9(c)). Individuals do not keep track of the interface and are immediately left behind the trailing edge, which creates a gap between the largest portion of the population and the suitable habitat (Fig. 10(c)). The population profile is hump shaped and the population density decreases towards zero due to diffusion and mortality.

The population can persist in a growing habitat so long as the trailing edge is not moving too fast. This result is similar to the results found in [31] and [32]. In these two studies, the suitability of the habitat is determined by the intrinsic growth rate, $r(x - ct)$, which is a continuous, nondecreasing function with a negative intrinsic growth rate as $x \to -\infty$ and a positive intrinsic growth rate as $x \to \infty$. The suitable habitat is the half line where $r(x - ct) > 0$. In both papers, the authors showed that the species could not invade the suitable habitat if the edge of the habitat shifted faster than the Fisher speed. A growing interval shifting in one direction would asymptotically reach the spatial

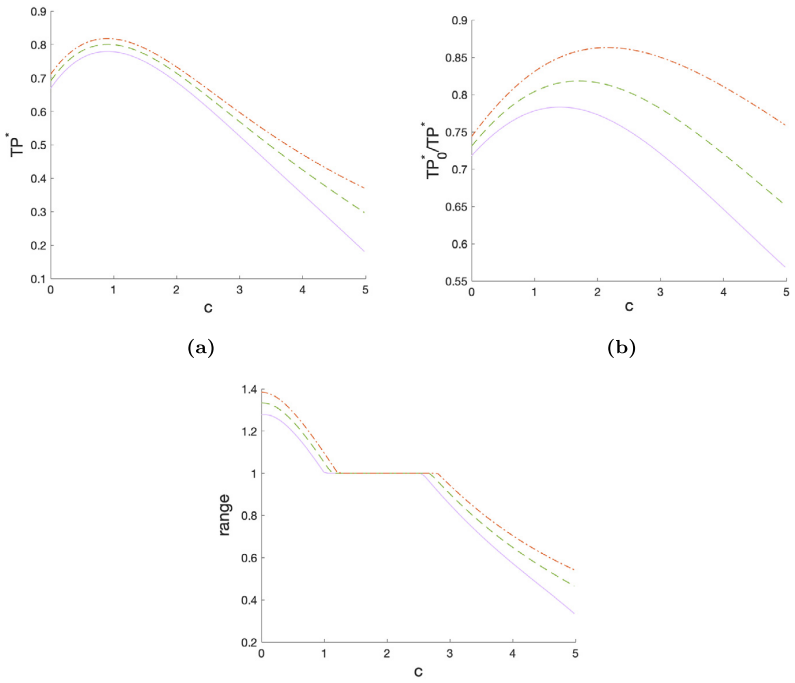

Fig. 8. Illustrations of how the total population and range are impacted by c for $\alpha = 0.93$, (solid in purple), $\alpha = 0.95$, (dashed in green), and $\alpha = 0.97$, (dash-dotted in orange). The range threshold is 0.1. Other model parameter values are $d_1 = 10$, $d_2 = 1$, $m_1 = 1$, $m_2 = 1.4$, $\beta = 0.7$ and $L = 1$. Panel 8(a): The total population as a function of c for various values of α. Panel 8(b): The ratio of the total population inside Ω_0 over the total population as a function of c for various values of α. Panel 8(c):The range as a function of c for various values of α.

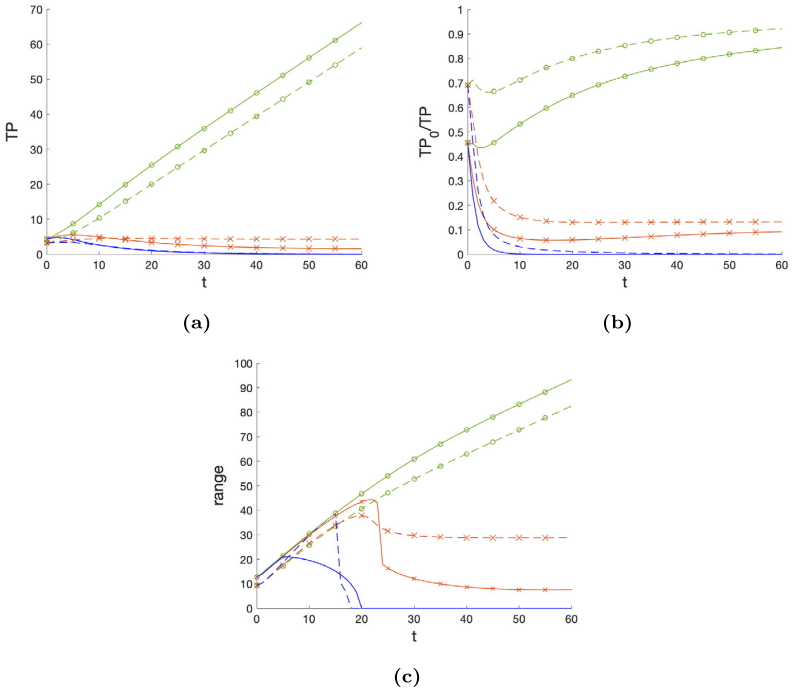

Fig. 9. Illustrations of how the total population and range change over time for $c_1 = 1$, (green with circles), $c_1 = 2$ (orange with crosses), and $c_1 = 2.5$ (blue). The dashed and solid line styles correspond to $\alpha = 0.8$ and $\alpha = 0.5$, respectively. The range threshold is 0.05. Other model parameter values are $d_i = 1$, $m_1 = 0.1$, $m_2 = 1.4$, $\beta = 0.5$, $L = 3$, and $c_2 = 3$. Panel 9(a): The total population as a function of time. Panel 9(b): The ratio of the total population inside Ω_0 over the total population as a function of time. Panel 9(c): The range as a function of time.

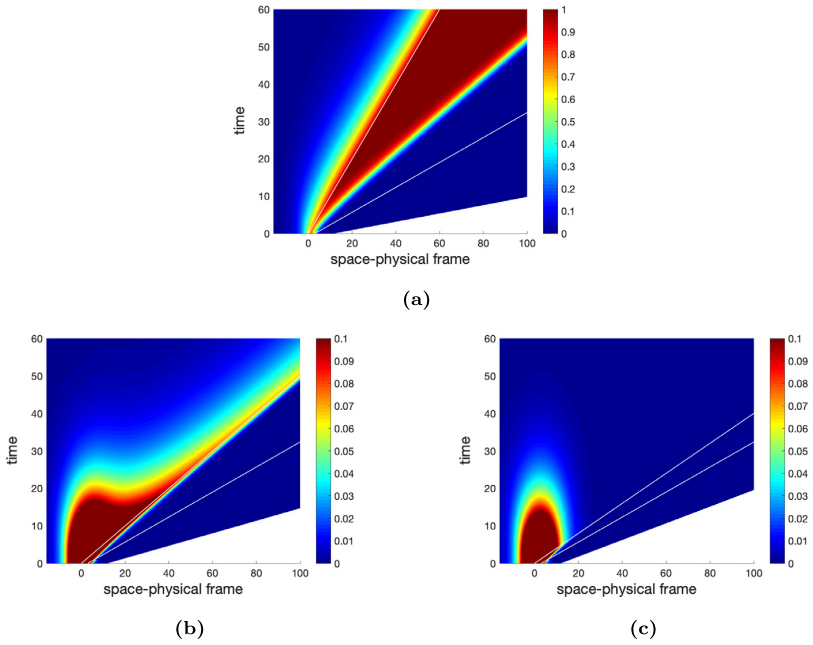

Fig. 10. The population profile as it changes over time and space when $c = 1$ (top), $c = 2$ (bottom left), and $c = 2.5$ (bottom right). Note the scale of the colourmap differs between the top and bottom figures. The white lines indicate the location of the trailing and leading edge. Other parameter values are $d_i = 1$, $m_1 = 0.1$, $m_2 = 1.4$, $\alpha = \beta = 0.5$, $L = 3$, and $c_2 = 3$.

setting of [31] and [32]. In the bounded suitable habitat, when an invasion front can be established, it is controlled by the speed of the leading edge, in that it travels at speed c_2 if $c_2 < c^*$ and travels at the Fisher speed when $c_2 > c^*$.

Populations at high risk of extinction can be identified with an expanding zombie population (Fig. 9(b), 9(c), 10(b), 10(c)).

5.3. Accelerating speeds

Accelerating speeds of environmental change have been observed for global warming, e.g., ocean temperature [12], and from direct human impact, e.g., deforestation [69]. To model such a scenario, we assume for simplicity that both interfaces accelerate at the same rate and we take $L_1 = t^{1+\epsilon}$ and $L_2 = L + t^{1+\epsilon}$, for $\epsilon > 0$. This assumption keeps the interfaces an equal distance apart for all time. When the interfaces move at a constant speed, there exists, for every parameter set, a speed c^* above which the population will go extinct. Thus, accelerating speeds will eventually lead to population extinction. We study the time to extinction and focus on the impact of α on this quantity. We define the time to extinction for an arbitrarily chosen positive value E as the time at which $TP = E$ and $TP' < 0$.

The time to extinction is a decreasing function of ϵ (Fig. 11). When ϵ is small, large values of α increase the time to extinction, but when ϵ is large, the pattern is reversed (Fig. 11).

When ϵ is very small, there is almost no acceleration and the interfaces appear to be moving at a constant speed. Within the first 100 time units, the density profile takes the shape of a travelling pulse (Fig. 12(a)). As ϵ increases, the population goes extinct within the first 100 time units, but the highest population density can still be found close to the suitable habitat (Fig. 12(b)). For larger values of ϵ, the time to extinction is even shorter and the highest population density is eventually found far away from the suitable habitat (Fig. 12(c)). The shifting speed is accelerating too quickly for the population to keep up, yet the population decay rate is small enough so that the population remains tractable for an interval of time. For high enough values of ϵ, the population completely "detaches" from the suitable habitat early on and decays in the trailing unsuitable habitat (Fig. 12(d)).

When ϵ is small enough, a strong bias for the suitable habitat helps the population stay "connected" to the suitable habitat (Fig. 13(a), 13(b)). When ϵ is too large, a strong bias for the suitable habitat reduces the zombie population, which consequently reduces the time to extinction (Figs. 13(c) and 13(d)). This result highlights again the two opposite effects that habitat preference can have on population spread and persistence.

Acceleration inevitably leads to extinction. Even for small ϵ, the observed travelling pulse profile is transient behaviour. The speed at which interfaces are travelling will eventually exceed the critical speed for the given parameter set. Large ϵ causes "detachment" from the suitable habitat, in that the majority of the population is far behind the trailing edge. And this "detachment" occurs irrespective of the strength of the bias for the suitable habitat.

6. Discussion

We have introduced a generalized model for population dynamics in a moving habitat and a corresponding numerical scheme. Our scheme is applicable to a vast array of prescribed functions $L_i(t)$. Thus, our scheme is a tool for research beyond the common assumption of constant matching speeds. The scheme is efficient, accurate and easy to implement.[1] It provides insight into the transient stages of the dynamics and can thereby help identify key qualitative behaviour indicating at-risk populations.

6.1. Numerical aspects

Since we use a conformal grid and our reference frame fixes the interfaces in space, we eliminate error from interpolation. A nonuniform grid improves CPU and memory cost by concentrating the nodes near the interfaces where the jumps in density and largest gradients occur.

[1] Code is available upon request.

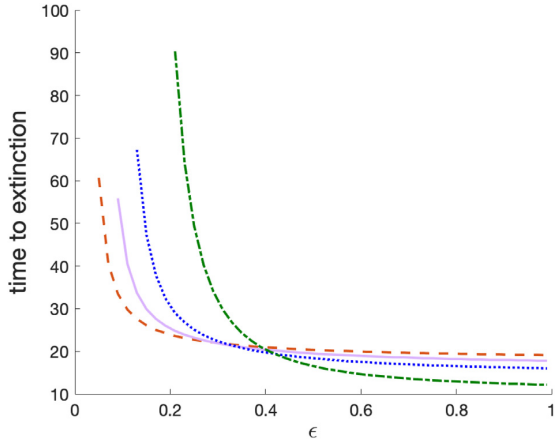

Fig. 11. The time to extinction as a function of ϵ for $E = 0.1$ and for $\alpha = 0.3$ (dashed in orange), $\alpha = 0.5$ (solid in purple), $\alpha = 0.7$ (dotted in blue), and $\alpha = 0.9$ (dash-dotted in green). For a given ϵ, if extinction did not happen within the first 100 time units, nothing is plotted. Other model parameters are $d_i = 1$, $m_1 = 0.1$, $m_2 = 1.4$, $\beta = 0.5$, and $L = 3$...

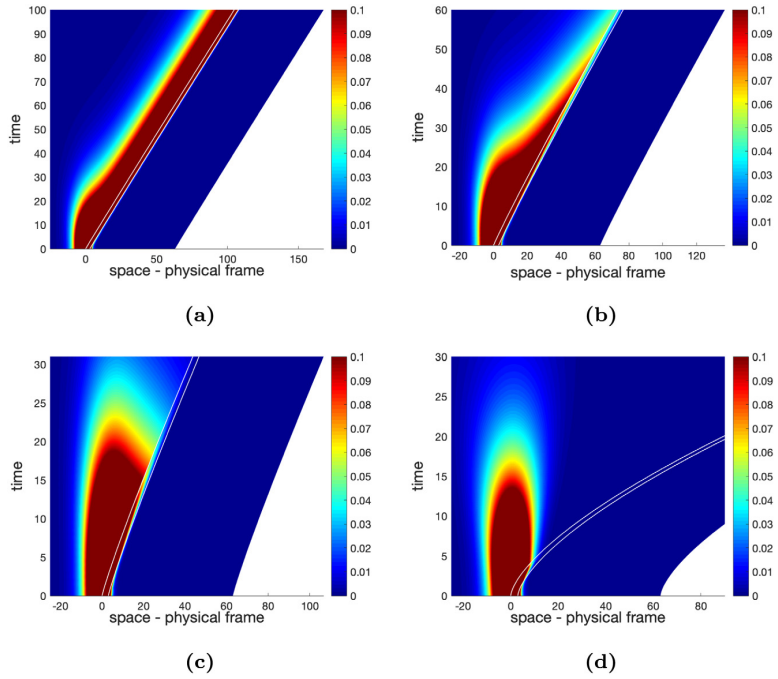

Fig. 12. The population profile as it changes over time and space when $\alpha = 0.3$ for $\epsilon = 0.01$ (top left), $\epsilon = 0.05$ (top right), $\epsilon = 0.1$ (bottom left), and $\epsilon = 0.5$ (bottom right). Note that both the horizontal and vertical scales vary between the figures. Other parameter values are $d_i = 1$, $m_1 = 0.1$, $m_2 = 1.4$, $\beta = 0.5$, and $L = 3$.

We do not remesh in our scheme and so avoid introducing error from interpolation. The scheme was validated with the interfaces moving at constant matching speeds. This validation provides an upper bound on the numerical parameters. When there is large deformation of the suitable habitat, one may need a fine mesh to ensure accuracy and stability of the solution for larger times, as a coarser initial mesh may become inadequate. A remeshing technique coupled with error estimation would work well to resolve this issue and to allow the scheme to run for all final times, but would in turn introduce interpolation error.

We represent the interfaces with a conformal grid and discretize the interface flux conditions with a second-order finite difference. Thus, the scheme could be made globally second-order accurate in space and time by discretizing the PDE using a second-order finite difference method at internal nodes.

In constructing the scheme, we made no assumption on the direction or speed of the interfaces so that the interfaces can move in opposite directions. A mapping from the reference frame to the physical frame must be known analytically to apply the scheme and we give a suggestion for this mapping. This mapping cannot capture changes in topology, for example, splitting of the suitable habitat into two suitable habitats, and leads to a singular limit when the domain collapses. Albeit, one might argue this is a degenerate case.

6.2. Ecological aspects

Our approach provides a new tool for understanding the population dynamics of moving-habitat models. By including habitat-dependent

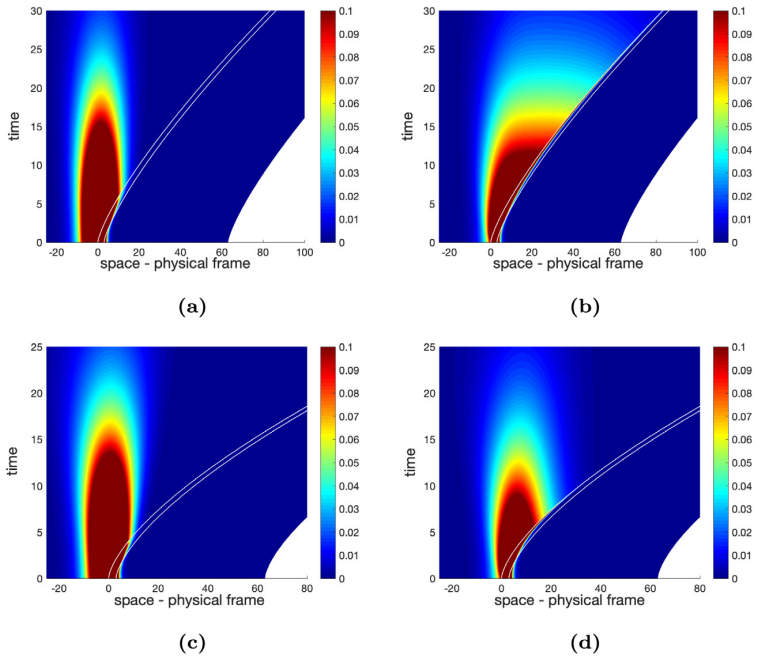

Fig. 13. The population profile as it changes over time and space when $\epsilon = 0.3$ (top) and $\epsilon = 0.5$ (bottom) for $\alpha = 0.3$ (left), $\alpha = 0.9$ (right). Note that the horizontal and vertical scales differ between top and bottom figures. Other parameter values are $d_i = 1$, $m_1 = 0.1$, $m_2 = 1.4$, $\beta = 0.5$, and $L = 3$.

dispersal rates and preferential movement, we generalize current studies and gain insight into the mechanisms that support persistence. Due to the general assumptions made on the movement of the habitat edges, we can explore several climate change scenarios outside the common constant speed case; see Section 1.

In Section 5, we explored three different scenarios. In the first scenario of constant matching speeds, we gained insight into the mechanisms that can promote a larger total population in the travelling pulse state than that of the corresponding stationary steady state. Numerically, we showed that a travelling pulse state exists and our scheme provides a reliable numerical approximation of this travelling pulse. Additionally, in Section 2.3, we analytically determined the shape of the profile at the travelling pulse state. We believe this state to be unique and globally attracting when the trivial steady state is unstable. This has yet to be proven analytically.

A growing suitable habitat was the second scenario we considered. Even though the habitat is growing, the trailing edge cannot move too fast if the population is to persist. With our simulations, we found that for large enough times, the shape of the profile at the trailing edge can be determined by Proposition 1 and Corollary 2 with c replaced by c_1. Furthermore, extinction or persistence outcomes conform to the theory determined in [17] again with c_1 replacing c. An analytical proof of these observations is for future research.

Previous studies that looked at expanding/shrinking habitats consider only one interface separating two habitat types, with one habitat type invading the other; see for example [32,33]. This differs from our approach as we have two interfaces bounding the suitable habitat. Thus, our scheme is applicable to various types of growing or shrinking domains and, in turn, is applicable to numerous phenomena. Human impact can change the size of a suitable habitat, for example, deforestation (shrinking) and reforestation (growing). Our scheme could be used to study the transient impacts of extinction debt on populations as a result of deforestation [70].

Finally, we applied our scheme to accelerating speeds of climate change. We observed that large acceleration rates can cause the majority of the population to "detach" from the suitable habitat. In [52], the author defines the term *niche deficit* which describes the population lagging behind their optimal climate niche. The "detachment" that we observe may be considered an extreme case of this deficit. In the case of quickly shifting growing domains we also observed a similar phenomenon (Fig. 10(c)). An important insight from the accelerating case is that a population in a steady travelling pulse state might be, on some transient time scale, indistinguishable from a transient profile of a population heading to eventual extinction.

A consistent insight found among all cases considered was that a high preference for the suitable habitat can actually reduce the total population density as it decreases the zombie population. In the two cases of constant moving interfaces, a high preference helps the population persist at fast shifting speeds, contrastively, at fast acceleration rates it lowers the time to extinction as a consequence of the low density in the zombie population. In [68], the authors show that the zombie population benefits the population in the suitable habitat via seed dispersal. Similarly, in our case, we showed that the zombie population can increase the total population size. Additionally, we observed that a larger zombie population can help increase the time to extinction.

The three scenarios we considered give examples of the insight we can gain from our scheme. We have not exhaustively explored these three scenarios and other scenarios are still of interest, for example periodic speeds. The scheme is an enriching tool for the further study of the impact of climate change on populations.

Declaration of competing interest

The authors declare that they have no known competing financial interests or personal relationships that could have appeared to influence the work reported in this paper.

Acknowledgements

This work was supported by the NSERC CREATE "Simulation Based Engineering" program and an Ontario Graduate Scholarship to JSM, an NSERC, Canada Discovery Grant (RGPIN-2016-0495) to FL and an NSERC, Canada Discovery Grant (RGPIN-2019-06855) to YB.

References

[1] T.L. Root, J.T. Price, K.R. Hall, S.H. Schneider, C. Rosenzweig, J.A. Pounds, Fingerprints of global warming on wild animals and plants, Nature 421 (6918) (2003) 57–60.

[2] C. Parmesan, G. Yohe, A globally coherent fingerprint of climate change impacts across natural systems, Nature 421 (6918) (2003) 37–42.

[3] C.D. Thomas, A. Cameron, R.E. Green, M. Bakkenes, L.J. Beaumont, Y.C. Collingham, B.F. Erasmus, M.F. De Siqueira, A. Grainger, L. Hannah, et al., Extinction risk from climate change, Nature 427 (6970) (2004) 145–148.

[4] A.T. Hitch, P.L. Leberg, Breeding distributions of North American bird species moving north as a result of climate change, Conserv. Biol. 21 (2) (2007) 534–539.

[5] H.M. Pereira, P.W. Leadley, V. Proença, R. Alkemade, J.P. Scharlemann, J.F. Fernandez-Manjarrés, M.B. Araújo, P. Balvanera, R. Biggs, W.W. Cheung, et al., Scenarios for global biodiversity in the 21st century, Science 330 (6010) (2010) 1496–1501.

[6] M.C. Urban, Accelerating extinction risk from climate change, Science 348 (6234) (2015) 571–573.

[7] J.J. Wiens, Climate-related local extinctions are already widespread among plant and animal species, PLoS Biol. 14 (12) (2016) e2001104.

[8] V.K. Lagerholm, E. Sandoval-Castellanos, A. Vaniscotte, O.R. Potapova, T. Tomek, Z.M. Bochenski, P. Shepherd, N. Barton, M.-C. Van Dyck, R. Miller, et al., Range shifts or extinction? Ancient DNA and distribution modelling reveal past and future responses to climate warming in cold-adapted birds, Global Change Biol. 23 (4) (2017) 1425–1435.

[9] N. Pepin, R.S. Bradley, H.F. Diaz, M. Baraer, E.B. Caceres, N. Forsythe, H. Fowler, G. Greenwood, M.Z. Hashmi, X.D. Liu, J.R. Miller, L. Ning, A. Ohmura, E. Palazzi, I. Rangwala, W. Schöner, I. Severskiy, M. Shahgedanova, M.B. Wang, S.N. Williamson, D.Q. Yang, Elevation-dependent warming in mountain regions of the world, Nature Clim. Change 5 (5) (2015) 424–430.

[10] E. Palazzi, L. Mortarini, S. Terzago, J. Hardenberg, Elevation-dependent warming in global climate model simulations at high spatial resolution, Clim. Dynam. 52 (5) (2019) 2685–2702.

[11] M. Tudoroiu, E. Eccel, B. Gioli, D. Gianelle, H. Schume, L. Genesio, F. Miglietta, Negative elevation-dependent warming trend in the Eastern Alps, Environ. Res. Lett. 11 (4) (2016) 044021.

[12] L. Cheng, J. Abraham, Z. Hausfather, K.E. Trenberth, How fast are the oceans warming? Science 363 (6423) (2019) 128–129.

[13] C.B. Schultz, E.E. Crone, Edge-mediated dispersal behavior in a prairie butterfly, Ecology 82 (7) (2001) 1879–1892.

[14] K. J. Haynes, J. T. Cronin, Interpatch movement and edge effects: the role of behavioral responses to the landscape matrix, Oikos 113 (1) (2006) 43–54.

[15] O. Ovaskainen, S.J. Cornell, Biased movement at a boundary and conditional occupancy times for diffusion processes, J. Appl. Probab. (2003) 557–580.

[16] G.A. Maciel, F. Lutscher, How individual movement response to habitat edges affects population persistence and spatial spread, Amer. Nat. 182 (1) (2013) 42–52.

[17] J.S. MacDonald, F. Lutscher, Individual behavior at habitat edges may help populations persist in moving habitats, J. Math. Biol. 77 (6–7) (2018) 2049–2077.

[18] A.B. Potapov, M.A. Lewis, Climate and competition: the effect of moving range boundaries on habitat invasibility, Bull. Math. Biol. 66 (5) (2004) 975–1008.

[19] H. Berestycki, O. Diekmann, C. Nagelkerke, P. Zegeling, Can a species keep pace with a shifting climate? Bull. Math. Biol. 71 (2008) 339–429.

[20] H. Berestycki, L. Rossi, Reaction-diffusion equations for population dynamics with forced speed I - The case of the whole space, Discrete Contin. Dyn. Syst. A 21 (1) (2008) 41.

[21] H. Berestycki, L. Rossi, Reaction-diffusion equations for population dynamics with forced speed II - cylindrical-type domains, Discrete Contin. Dyn. Syst. A 25 (1) (2009) 19.

[22] J. Bouhours, T. Giletti, Extinction and spreading of a species under the joint influence of climate change and a weak Allee effect: a two-patch model, 2016, arXiv preprint arXiv:1601.06589.

[23] Z. Zhang, W. Wang, J. Yang, Persistence versus extinction for two competing species under a climate change, Nonlinear Anal. Model. Control 22 (3) (2017) 285–302.

[24] H. Hu, X. Zou, Existence of an extinction wave in the Fisher equation with a shifting habitat, Proc. Amer. Math. Soc. 145 (11) (2017) 4763–4771.

[25] C. Cosner, Challenges in modeling biological invasions and population distributions in a changing climate, Ecol. Complex. 20 (2014) 258–263.

[26] H. Hu, T. Yi, X. Zou, On spatial-temporal dynamics of a Fisher-KPP equation with a shifting environment, Proc. Amer. Math. Soc. 148 (1) (2020) 213–221.

[27] H.-H. Vo, Persistence versus extinction under a climate change in mixed environments, J. Differential Equations 259 (10) (2015) 4947–4988.

[28] L. Roques, A. Roques, H. Berestycki, A. Kretzschmar, A population facing climate change: joint influences of Allee effects and environmental boundary geometry, Popul. Ecol. 50 (2) (2008) 215–225.

[29] J. Fang, R. Peng, X.-Q. Zhao, Propagation dynamics of a reaction-diffusion equation in a time-periodic shifting environment, J. Math. Pures Appl. 147 (2021) 1–28.

[30] H. Berestycki, L. Desvillettes, O. Diekmann, Can climate change lead to gap formation? Ecol. Complex. 20 (2014) 264–270.

[31] Y. Yuan, X. Zou, Spatial-temporal dynamics of a diffusive Lotka-Volterra competition model with a shifting habitat II: Case of faster diffuser being a weaker competitor, J. Dynam. Differential Equations (2020) 1–42.

[32] B. Li, S. Bewick, J. Shang, W.F. Fagan, Persistence and spread of a species with a shifting habitat edge, SIAM J. Appl. Math. 74 (5) (2014) 1397–1417.

[33] B. Li, S. Bewick, M.R. Barnard, W.F. Fagan, Persistence and spreading speeds of integro-difference equations with an expanding or contracting habitat, Bull. Math. Biol. 78 (7) (2016) 1337–1379.

[34] J. Bouhours, M.A. Lewis, Climate change and integrodifference equations in a stochastic environment, Bull. Math. Biol. 78 (9) (2016) 1866–1903.

[35] Y. Zhou, M. Kot, Discrete-time growth-dispersal models with shifting species ranges, Theor. Ecol. 4 (1) (2011) 13–25.

[36] M.A. Harsch, Y. Zhou, J. HilleRisLambers, M. Kot, Keeping pace with climate change: stage-structured moving-habitat models, Amer. Nat. 184 (1) (2014) 25–37.

[37] C.A. Cobbold, R. Stana, Should I stay or should I go: Partially sedentary populations can outperform fully dispersing populations in response to climate-induced range shifts, Bull. Math. Biol. 82 (2) (2020) 1–21.

[38] M. Kot, A. Phillips, Bounds for the critical speed of climate-driven moving-habitat models, Math. Biosci. 262 (2015) 65–72.

[39] M.A. Harsch, A. Phillips, Y. Zhou, M.-R. Leung, D.S. Rinnan, M. Kot, Moving forward: insights and applications of moving-habitat models for climate change ecology, J. Ecol. 105 (5) (2017) 1169–1181.

[40] M.A. Lewis, N.G. Marculis, Z. Shen, Integrodifference equations in the presence of climate change: persistence criterion, travelling waves and inside dynamics, J. Math. Biol. 77 (6) (2018) 1649–1687.

[41] A. Phillips, M. Kot, Persistence in a two-dimensional moving-habitat model, Bull. Math. Biol. 77 (2015) 2125–2159.

[42] C. Wu, Y. Wang, X. Zou, Spatial-temporal dynamics of a Lotka-Volterra competition model with nonlocal dispersal under shifting environment, J. Differential Equations 267 (8) (2019) 4890–4921.

[43] J.-B. Wang, X.-Q. Zhao, Uniqueness and global stability of forced waves in a shifting environment, Proc. Amer. Math. Soc. 147 (4) (2019) 1467–1481.

[44] W.-T. Li, J.-B. Wang, X.-Q. Zhao, Spatial dynamics of a nonlocal dispersal population model in a shifting environment, J. Nonlinear Sci. 28 (4) (2018) 1189–1219.

[45] M. Alfaro, H. Berestycki, G. Raoul, The effect of climate shift on a species submitted to dispersion, evolution, growth and nonlocal competition, SIAM J. Math. Anal. 49 (1) (2017) 562–596.

[46] J.-B. Wang, C. Wu, Forced waves and gap formations for a Lotka-Volterra competition model with nonlocal dispersal and shifting habitats, Nonlinear Anal. RWA 58 (2021) 103208.

[47] G.-B. Zhang, X.-Q. Zhao, Propagation dynamics of a nonlocal dispersal Fisher-KPP equation in a time-periodic shifting habitat, J. Differential Equations 268 (6) (2020) 2852–2885.

[48] C. Hu, B. Li, Spatial dynamics for lattice differential equations with a shifting habitat, J. Differential Equations 259 (5) (2015) 1967–1989.

[49] H. Wang, C. Pan, C. Ou, Existence of forced waves and gap formations for the lattice Lotka-Volterra competition system in a shifting environment, Appl. Math. Lett. 106 (2020) 106349.

[50] Y. Meng, Z. Yu, S. Zhang, Spatial dynamics of the lattice Lotka-Volterra competition system in a shifting habitat, Nonlinear Anal. RWA 60 (2021) 103287.

[51] R.A. Fisher, The wave of advance of advantageous genes, Ann. Eugen. 7 (4) (1937) 355–369.

[52] Y. Zhou, Geographic Range Shifts under Climate Warming (Ph.D. thesis), University of Washington, 2013.

[53] E. Knobloch, R. Krechetnikov, Problems on time-varying domains: Formulation, dynamics and challenges, Acta Appl. Math. 137 (1) (2015) 123–157.

[54] S. Liu, X. Liu, Numerical methods for a two-species competition-diffusion model with free boundaries, Mathematics 6 (5) (2018) 72.

[55] A. Madzvamuse, P.K. Maini, Velocity-induced numerical solutions of reaction-diffusion systems on continuously growing domains, J. Comput. Phys. 225 (1) (2007) 100–119.

[56] C. Zmurchok, J. Collette, V. Rajagopal, W.R. Holmes, Membrane tension can enhance adaptation to maintain polarity of migrating cells, Biophys. J. 119 (8) (2020) 1617–1629.

[57] J. Mackenzie, C. Rowlatt, R. Insall, A conservative finite element ALE scheme for mass-conservative reaction-diffusion equations on evolving two-dimensional domains, SIAM J. Sci. Comput. 43 (1) (2021) B132–B166.

[58] J. Donea, A. Huerta, J.-P. Ponthot, A. Rodrıguez-Ferran, Arbitrary Lagrangian-Eulerian methods, in: Encyclopedia of Computational Mechanics, vol. 1, Fundamentals, 2004.

[59] O. Lakkis, A. Madzvamuse, C. Venkataraman, Implicit–explicit timestepping with finite element approximation of reaction-diffusion systems on evolving domains, SIAM J. Numer. Anal. 51 (4) (2013) 2309–2330.

[60] T.E. Lee, M.J. Baines, S. Langdon, A finite difference moving mesh method based on conservation for moving boundary problems, J. Comput. Appl. Math. 288 (2015) 1–17.

[61] W. Huang, R.D. Russell, Adaptive Moving Mesh Methods, vol. 174, Springer Science & Business Media, 2010.
[62] D.R. Noble, E.P. Newren, J.B. Lechman, A conformal decomposition finite element method for modeling stationary fluid interface problems, Internat. J. Numer. Methods Fluids 63 (6) (2010) 725–742.
[63] Z. Li, An overview of the immersed interface method and its applications, Taiwanese J. Math. 7 (1) (2003) 1–49.
[64] A. Wiegmann, K.P. Bube, The explicit-jump immersed interface method: finite difference methods for PDEs with piecewise smooth solutions, SIAM J. Numer. Anal. 37 (3) (2000) 827–862.
[65] J.C. Strikwerda, Finite Difference Schemes and Partial Differential Equations, SIAM, 2004.
[66] M. Ethier, Y. Bourgault, Semi-implicit time-discretization schemes for the bidomain model, SIAM J. Numer. Anal. 46 (5) (2008) 2443–2468.
[67] T. Roy, Y. Bourgault, C. Pierre, Analysis of time-stepping methods for the monodomain model, Comput. Appl. Math. 39 (3) (2020) 1–32.
[68] R.R. Decker, Plant population dynamics under climate changes: invasions, range shifts and resilience (Ph.D. thesis), UC Davis, 2019.
[69] Z. Zeng, D.B. Gower, E.F. Wood, Accelerating forest loss in Southeast Asian massif in the 21st century: A case study in Nan Province, Thailand, Global Change Biol. 24 (10) (2018) 4682–4695.
[70] P.K. Lira, R.M. Ewers, C. Banks-Leite, R. Pardini, J.P. Metzger, Evaluating the legacy of landscape history: extinction debt and species credit in bird and small mammal assemblages in the Brazilian Atlantic Forest, J. Appl. Ecol. 49 (6) (2012) 1325–1333.

Chapter 4

Periodic Shifting Speeds

In the previous chapter, we introduced a one-dimensional moving-habitat model that can capture arbitrary movement of habitat edges. These habitat edges are defined by sharp interfaces, cutting the domain into three distinct patches, with the middle patch representing the suitable habitat and the two infinite patches on either side, the unsuitable habitat. We built, implemented, and validated a finite difference scheme that can accommodate multiple kinds of interface movement. With this scheme, we studied three interface movement types, motivated by biological scenarios. We dedicate the present chapter to the numerical study of yet another kind of interface movement: periodically shifting speeds.

4.1 Introduction

The interface movements we have studied so far all share the property that the interfaces move consistently in one direction. Although temperature isoclines have a general trend (poleward, or up in altitude), the actual location of a temperature isocline varies around this trend [13]. Additionally, other influences on habitat, like flooding, or seasonal resources, can result in seasonal expansion and contraction of a suitable habitat [28, 41].

There is a growing literature focusing on capturing such fluctuations. Within the set of moving-habitat models, researchers have introduced stochastic variation in speed in the integro-difference framework (appropriate when dispersal and growth happen at distinct times) [9] , studied the existence of time-periodic waves in periodically varying environments where the habitat is suitable to the far left and unsuitable to the far right and changes suitability on a gradient [18], and studied the existence of time-periodic waves in higher space dimensions [4]. Most closely related to our work, the authors of [56] studied the existence of time-periodic travelling pulses when the suitable habitat's shifting speed and location fluctuate almost-periodically and periodically. They focused on the effect of the amplitude of these fluctuations. Addi-

tionally, in [64], the authors studied, via integro-difference equations, the impact of fluctuations in size of the suitable habitat in the absence of an environmental shift.

We contribute two important aspects to this literature. The first is the impact of the amplitude and frequency of periodic fluctuations on population levels in shifting environments. The second is a thorough numerical study of the impact of periodic fluctuations in the size of the suitable habitat in the presence of a constant environmental shift. We structure this chapter so that we first study periodic fluctuations only in the speed and location. Then, we introduce periodic fluctuations in the size of the suitable habitat additional to the shift. In both cases, we take a completely numerical approach, applying the numerical scheme developed in Chapter 3. This approach enables us to study in depth the population profiles and population levels in time. We largely focus on studying the change in population levels compared to the absence of fluctuations. We show that some variation can indeed assist a population by keeping population levels higher than the population levels attained when there is no fluctuation.

4.2 The Model

We consider the same model as we did in Chapter 3, but with the interfaces shifting at periodic speeds. For completeness, we briefly recall the model ingredients here. We model the population dynamics with a partial differential equation where $u = u(x,t)$ is the population density over space, x, and time, t. We assume spatial heterogeneity in only one direction, and idealise space to the real line. We define the suitable habitat as the interval $(L_1(t), L_2(t))$, and assume that this interval always has positive length. Outside $[L_1(t), L_2(t)]$ is the unsuitable habitat. Here, L_1 and L_2 are the interfaces between the suitable and unsuitable habitat. The location of the interfaces is dependent on time. We assume that they shift on average in the positive direction, so we call L_1 the trailing edge and L_2 the leading edge.

The population density changes in time due to dispersal and demography, where inside the suitable habitat the birth-death dynamics are described by the logistic function, and outside by linear mortality. At the habitat edges, $L_i(t)$, we assume that individuals may exhibit a bias for a habitat type; across habitat types, we assume that dispersal rates may differ. Thus, the system of equations is

$$u_t = d_0 u_{xx} + u(r - au), \qquad (x,t) \in \Omega_0 \times \mathbb{R}^+, \tag{4.2.1a}$$

$$u_t = d_i u_{xx} - m_i u, \qquad (x,t) \in \Omega_i \times \mathbb{R}^+, \tag{4.2.1b}$$

with interface conditions

$$u(L_1^+(t), t) = k^\alpha u(L_1^-(t), t), \tag{4.2.1c}$$

$$(d_0 u_x + L_1'(t)u)\,(L_1^+(t), t) = (d_1 u_x + L_1'(t)u)\,(L_1^-(t), t), \tag{4.2.1d}$$

and

$$u(L_2^-(t),t) = k^\beta u(L_2^+(t),t), \tag{4.2.1e}$$
$$(d_0 u_x + L_2'(t)u)\,(L_2^-(t),t) = (d_2 u_x + L_2'(t)u)\,(L_2^+(t),t), \tag{4.2.1f}$$

where

$$k^\alpha = \frac{\alpha}{1-\alpha}\sqrt{\frac{d_1}{d_0}}, \qquad k^\beta = \frac{\beta}{1-\beta}\sqrt{\frac{d_2}{d_0}}. \tag{4.2.1g}$$

Here, $\Omega_0 = \{x \in \mathbb{R} \mid L_1(t) < x < L_2(t)\}$, $\Omega_1 = \{x \in \mathbb{R} \mid x < L_1(t)\}$ and $\Omega_2 = \{x \in \mathbb{R} \mid x > L_2(t)\}$ denote the different habitat patches. The x, t subscripts denote partial derivatives. Since individuals die but do not reproduce outside the suitable habitat, it is reasonable to assume that the population density vanishes far away from the suitable habitat. We translate this assumption into the asymptotic conditions, $\lim_{x\to\pm\infty} u(x,t) = 0$. The parameters d_i, $i = 0,1,2$ are the diffusion coefficients, r is the intrinsic growth rate, a is the intraspecific competition coefficient, m_i, $i = 1,2$ are the mortality rates in the unsuitable habitats, and α (β) is the probability of an individual moving into the suitable habitat if at the trailing (leading) edge.

We consider the location of each temperature isocline to be periodically varying around a constant shift. We describe the interface movement as

$$L_1(t) = c_1 t + A_1 \sin(\omega_1 t) \quad \text{and} \quad L_2(t) = L + c_2 t + A_2 \sin(\omega_2 t),$$

where c_i is the average speed of L_i, A_i is the amplitude of variation and ω_i determines the frequency of variation. We determine the range for each of these parameters throughout the text, based on the condition that Ω_0 must be nonempty.

All parameters in our model have positive values, except the amplitude of variation, A_i, $i = 1,2$. Through the standard scaling given in detail in Chapter 3, we obtain $r = 1$, $d_0 = 1$, and $a = 1$. We now consider all variables and parameters as nondimensional quantities.

The analysis of our model is complicated by the interface movement. As done in Chapter 3 through the change of variable $\phi(x,t) \mapsto (y(x,t),t)$ where

$$y = L\frac{x - L_1(t)}{L_2(t) - L_1(t)}, \tag{4.2.2}$$

we rewrite the system in the reference frame, a coordinate system where the interfaces are fixed in space. The system restated in the reference frame is

$$w_t = \frac{1}{x_y^2} w_{yy} + \frac{x_t}{x_y} w_y + w(1-w), \qquad (y,t) \in \tilde{\Omega}_0 \times \mathbb{R}^+, \tag{4.2.3a}$$
$$w_t = \frac{d_i}{x_y^2} w_{yy} + \frac{x_t}{x_y} w_y - m_i w \qquad (y,t) \in \tilde{\Omega}_i \times \mathbb{R}^+,\ i = 1,2, \tag{4.2.3b}$$

with interface conditions

$$w(0^+,t) = k^\alpha w(0^-,t), \tag{4.2.3c}$$

$$\left(\frac{1}{x_y}w_y + L_1'(t)w\right)(0^+,t) = \left(\frac{d_1}{x_y}w_y + L_1'(t)w\right)(0^-,t), \tag{4.2.3d}$$

and

$$w(L^-,t) = k^\beta w(L^+,t), \tag{4.2.3e}$$

$$\left(\frac{1}{x_y}w_y + L_2'(t)w\right)(L^-,t) = \left(\frac{d_2}{x_y}w_y + L_2'(t)w\right)(L^+,t), \tag{4.2.3f}$$

where

$$k^\alpha = \frac{\alpha}{1-\alpha}\sqrt{d_1}, \qquad k^\beta = \frac{\beta}{1-\beta}\sqrt{d_2}. \tag{4.2.3g}$$

Here, $\tilde{\Omega}_0 = \{y \in \mathbb{R} \mid 0 < y < L)\}$, $\tilde{\Omega}_1 = \{y \in \mathbb{R} \mid y < 0\}$ and $\tilde{\Omega}_2 = \{y \in \mathbb{R} \mid y > L\}$. The y, t subscripts denote partial derivatives. The asymptotic conditions remain unchanged.

To analyse our system, we apply the numerical approach constructed and validated in Chapter 3. We truncate the infinite domain of the reference frame far enough away from the suitable habitat to capture the conditions at positive and negative infinity. We simulate the model dynamics with the forward-backward Euler scheme that accounts for the matching conditions at interfaces. We find the solution in the $(x,t)-$coordinate system (the physical frame) through the inverse mapping ϕ^{-1}. For complete details on this scheme, we point the reader to Chapter 3.

When $c_i = c$, $A_i = A$ and $\omega_i = \omega$ for $i = 1, 2$ then Ω_0 remains the same size (an interval of length L) for all time. In this case, the average shifting speed of Ω_0 is c and $A\sin(\omega t)$ describes fluctuations around c and the expected location of the centre of the suitable habitat. We call this the *constant patch-size case* and explore it in Section 4.3. We study fluctuations in the size of the suitable habitat by setting $A_1 \neq A_2$. This case is studied in Section 4.4, and we call it the *varying patch-size case*.

Throughout the next two sections, we will study how amplitude and frequency change the population outcome compared to the absence of such periodic variation; i.e., setting $c_i = c$ and $A_i = 0$ for $i = 1, 2$. Many studies in different modelling frameworks have considered this scenario; for the closest related papers, see [39, 48, 3]. A common finding among those papers is that there exists a critical shifting-speed c^*, dependent on model parameters, above which the population will go extinct; see Section 2.1. When the shifting speed is below c^* the population persists. In this case, solutions have the form of travelling pulses. The persistence condition can be characterised by the critical patch-size $L^* = L^*(c)$, where, for a given shifting speed c, the population persists only if $L > L^*$. One can show that L^* is an increasing function of c [39]. We will use this terminology throughout the present Chapter.

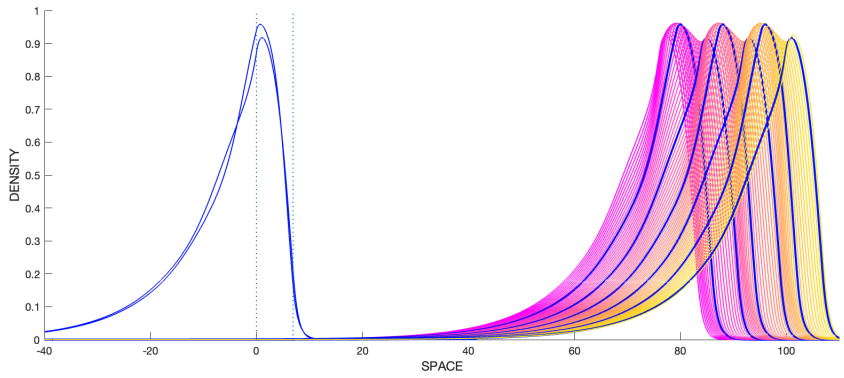

Figure 4.1: The periodic travelling pulse in the physical frame with the thick lines mapped into the reference frame. The periodic travelling pulse transitions from pink to yellow. The dotted vertical lines are the interfaces in the reference frame.

4.3 Constant Patch-Size

In this section, we study the case when $c_i = c$, $A_i = A$ and $\omega_i = \omega$ for $i = 1, 2$ and thus the length of Ω_0 is equal to L for all time. When it is necessary to distinguish between the direction of the shift at a given time, we say suitable habitat progression or recession when it is shifting in the positive or negative direction, respectively.

Shen et al [56] established analytical results on the existence of periodic travelling pulse solutions and persistence conditions when there is no jump across the interface. They focus on the impact of the amplitude of fluctuations. Particularly, they characterise persistence of the population through the approximate top Lyapunov exponent, which generalises the eigenvalue in the case of time-dependent equations. This quantity can be interpreted as the long-term average growth rate at low population densities. When the approximate top Lyapunov exponent is positive, the population will persist, when it is negative, the population will go extinct. Shen et al [56] show that this quantity is a non-increasing function of amplitude. In our analysis, we too characterise persistence conditions in terms of the amplitude of variation. Additionally, we study how the population density depends on frequency. Our approach is numerical, complements their results, and novelly contributes understanding to the effect of the amplitude and frequency on population outcomes.

4.3.1 Persistence Analysis

In the case of a constant patch-size, when the species is expected to persist, solutions to the system in the reference frame converge to a positive $\frac{2\pi}{\omega}$-periodic solution (Figure 4.1) [56]. In the physical frame, the solution shifts in space as a periodic travelling pulse. Thus, we can define a discrete mapping of the system by tracking the solution

at times $t = n\frac{2\pi}{\omega}$, $n \in \mathbb{N}$, that is

$$u\left(\cdot, \frac{n2\pi}{\omega}\right) \mapsto u\left(\cdot, \frac{(n+1)2\pi}{\omega}\right).$$

The periodic travelling pulse solution corresponds to a fixed point of the discrete map. From the theory of discrete dynamical systems, we have that the principal eigenvalue, λ, of the discrete map of the linearised system determines the persistence outcome. When $|\lambda| > 1$, the zero steady state of the discrete system is linearly unstable, when $|\lambda| < 1$, it is stable. Therefore, the population will persist if $|\lambda| > 1$, and go to extinction if $|\lambda| < 1$.

With the numerical scheme, we analyse the persistence outcome as a function of amplitude by applying the power method to the discrete mapping of the linearised model. We approximate $\lambda = \lambda^n = \max_{y\in\Omega} |U^n|$ where U^n is the numerical solution of the linearised system at time $t = n\frac{2\pi}{\omega}$, normalising on every iteration. We stop the iteration when $|\lambda^{n-1} - \lambda^n| < 10^{-6}$. We study, for various values of c, the persistence outcome as a function of A. We take $L = 1.5L^*$ so that in the absence of fluctuations, the population will persist. In particular, for larger shifting speeds, we take a larger suitable habitat length.

We find that there exists a positive value A^*, such that $\lambda < 1$ for $A > A^*$ (Figure 4.2a). Hence, the population can only endure variation of the shifting speed up to a certain threshold. Increasing values of A correspond to increasing speeds of swift, periodic suitable habitat progression. This speed can far exceed the critical speed in the case of no fluctuations. For large enough values of A, this causes an extensive toll on the population growth rate when at small densities, one that eventually causes the growth rate to become too small to support the population.

Across the columns, we observe that by increasing the average shifting speed, A^* also increases (Figure 4.2a). Yet, across the columns, not only the average shifting speed increases but also the suitable habitat length, as the critical patch-size is an increasing function of c; see Chapter 2. To better understand the relationship between c and A, we plot λ as a function of $\bar{A} = A/L(c)$ (Figure 4.2b). At higher average shifting speeds, the eigenvalue curve crosses the bifurcation point, $\lambda = 1$, at smaller values of $\bar{A}$. Thus, species occupying habitats with slower average shifting speeds, can withstand larger amplitudes relative to the suitable habitat length.

4.3.2 Population Density

The principal eigenvalue gives a condition for persistence. It is interpretable as the low-density growth rate. Here, we study how amplitude and frequency affect the long-time population density compared to the case when $A = 0$, given that the population will persist. We base our comparison on two quantities, the total population density and the range.

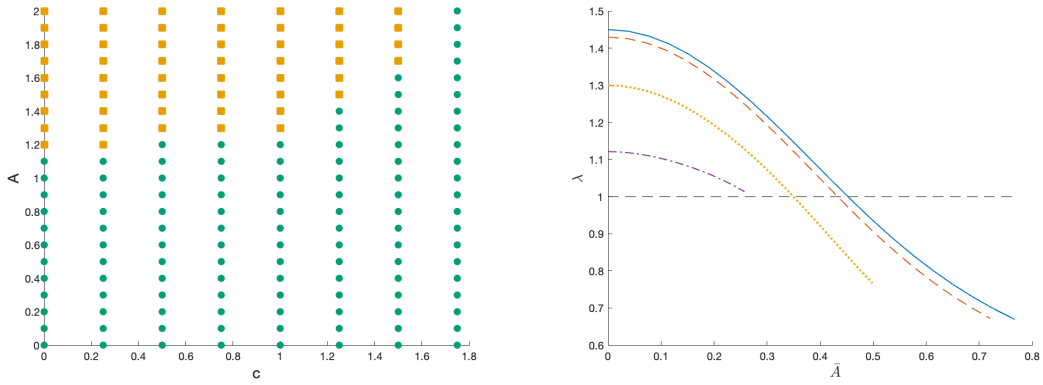

(a) **(b)**

Figure 4.2: Panel (a): The principal eigenvalue as a function of amplitude and average shifting speed. A green dot indicates that the population will persist ($\lambda > 1$), while an orange square indicates that the population will go to extinction ($\lambda < 1$). Panel (b): The principal eigenvalue as a function of $\bar{A}$ for shifting speeds, $c = 0$ (solid in blue), $c = 0.5$ (dashed in orange), $c = 1.25$ (dotted in yellow), and $c = 1.75$ (dash-dotted in purple). Other model parameters are $\alpha = 0.5 = \beta$, $D_i = 1$, $m_i = 1.4$, and $\omega = 2\pi$.

We define the total population density for a given amplitude and frequency as

$$TP_{A,\omega}(t) = \sum_{i=0}^{2} \int_{\Omega_i} u(x,t)dx.$$

We approximate this value numerically by using the trapezoidal rule. We define the maximum and minimum total population as

$$TP_{A,\omega}(\bar{t}) = \max_{t\in\mathcal{T}}(TP_{A,\omega}(t)), \quad \text{and} \quad TP_{A,\omega}(\underline{t}) = \min_{t\in\mathcal{T}}(TP_{A,\omega}(t)),$$

respectively, where $\mathcal{T} = \{t, t+\tau, ..., t+2\pi/\omega\}$, and τ denotes the time step.

We define the range as the interval within which u exceeds some arbitrarily chosen value, which we call the range threshold. One may interpret this value as a threshold value above which the species is detectable in the field. We denote the range as $R_{A,\omega}(t)$ and define the maximum and the minimum as

$$R_{A,\omega}(\bar{s}) = \max_{t\in\mathcal{T}}(R_{A,\omega}(t)) \quad \text{and} \quad R_{A,\omega}(\underline{s}) = \min_{t\in\mathcal{T}}(R_{A,\omega}(t)),$$

respectively.

We write TP and R if referring to the travelling pulse solution; i.e., when $A = 0$, $TP_{0,\omega} = TP$. We measure the relative difference between two quantities, for example between $Q_1 = TP_{A,\omega}(\underline{t})$ and $Q_2 = TP$, with the formula $(Q_1 - Q_2)/Q_2$.

We find that intermediate values of A can support larger total populations than the travelling pulse solution (Figure 4.3). That is, there are scenarios where there

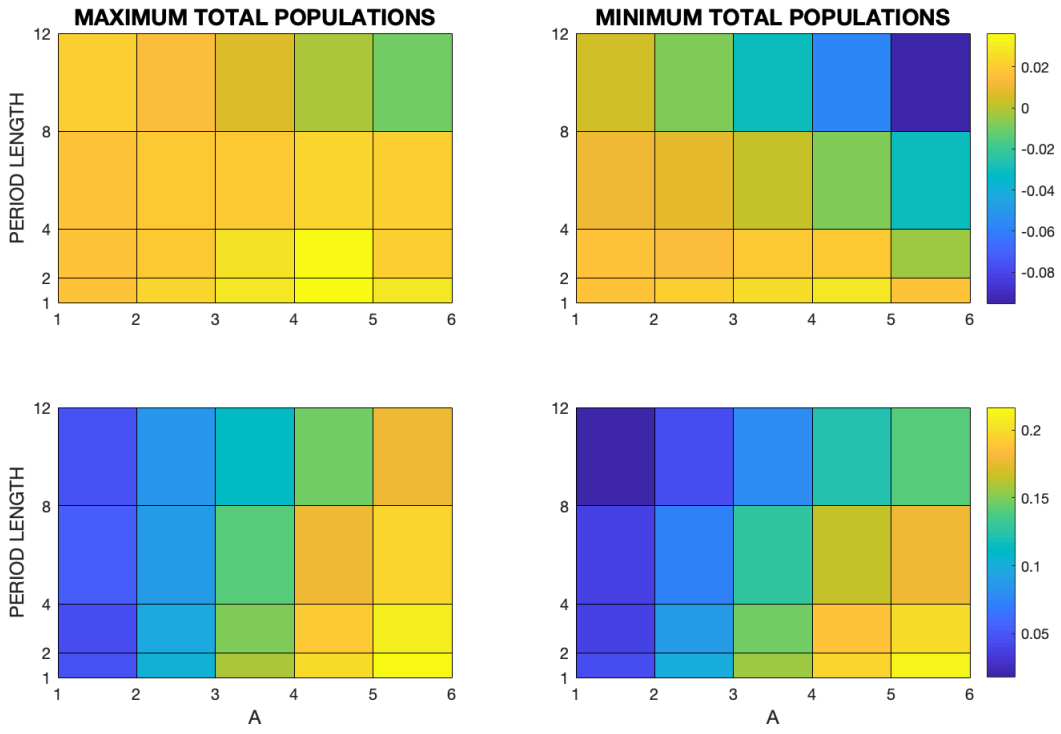

Figure 4.3: The relative difference between $TP_{A,\omega}(\bar{t})$, or $TP_{A,\omega}(\underline{t})$, and TP as functions of A and ω. Top panels: higher average shifting speed. Bottom panels: lower average shifting speed. Top panels: $c = 1$, $L = 5L^* \approx 6.9203$, and $TP \approx 14.9567$. Bottom panels: $c = 0.5$, $L = 5L^* \approx 4.0745$, and $TP \approx 9.2352$. Across all panels, other model parameters are $\alpha = 0.5 = \beta$, $d_i = 1$, $m_i = 0.1$ for $i = 1, 2$.

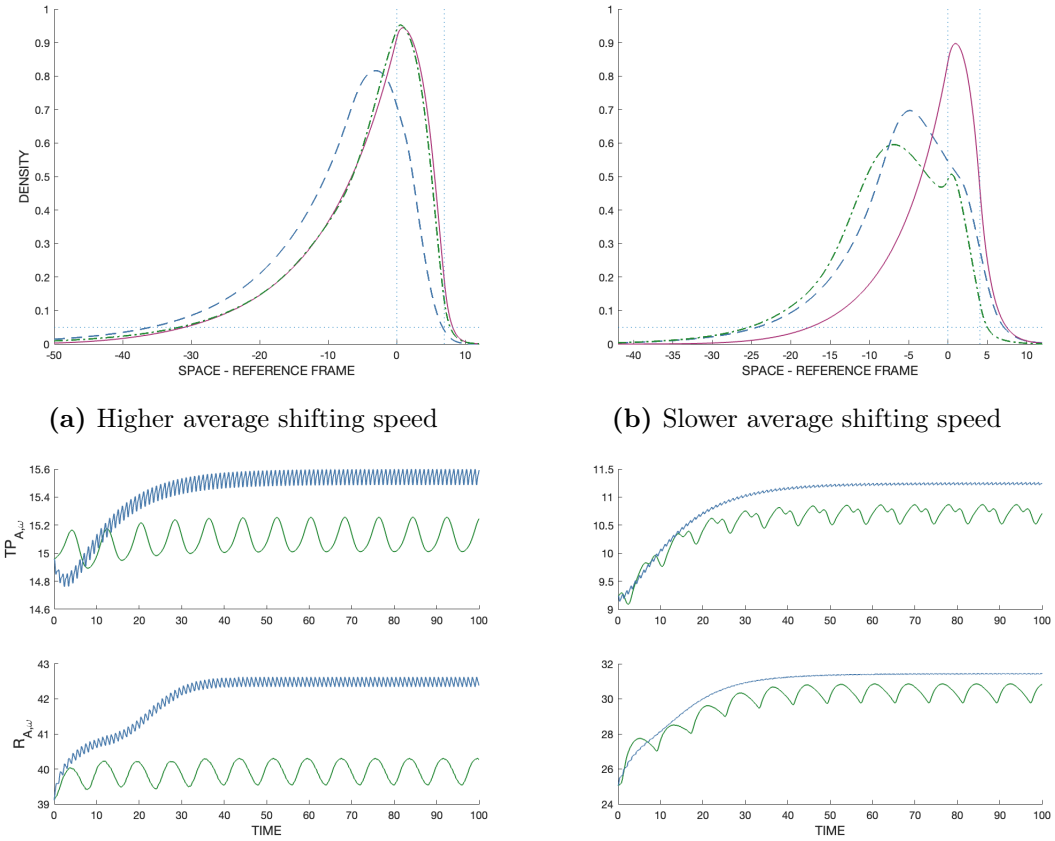

(a) Higher average shifting speed

(b) Slower average shifting speed

(c) Higher average shifting speed

(d) Slower average shifting speed

Figure 4.4: Top panels: The population density profiles at the time when $TP_{A,\omega}(\underline{t})$ is achieved compared to the travelling pulse solution (solid in purple). Dotted horizontal lines indicate the range threshold. Dotted vertical lines indicate the interfaces. Panel (a): Dashed blue curve and dashed-dotted green curve correspond to $(A,\omega) = (4, 2\pi)$, and $(A,\omega) = (1, \pi/4)$, respectively, with $c = 1$ and $L = 5L^* \approx 6.9203$. Panel (b): Dashed blue curve and dash-dotted green curve correspond to $(A,\omega) = (5, 2\pi)$, and $(A,\omega) = (5, \pi/4)$, respectively, with $c = 0.5$ and $L = 5L^* \approx 4.0745$. Bottom panels: Plots of $T_{A,\omega}(t)$ (across the top) and $R_{A,\omega}(t)$ (across the bottom). Panel (c): $c = 1$. Blue (high frequency) and green (low frequency) curves correspond to model parameters $(A,\omega) = (4, 2\pi)$ and $(A,\omega) = (1, \pi/4)$, respectively. Panel (d): $c = 0.5$. Blue (high frequency) and green (low frequency) curves correspond to model parameters $(A,\omega) = (5, 2\pi)$ and $(A,\omega) = (5, \pi/4)$, respectively. At $t = 0$, we plot the value of TP and R. Across all panels, other model parameters are $\alpha = 0.5 = \beta$, $d_i = 1$, $m_i = 0.1$ for $i = 1, 2$. The range threshold is 0.05. The axes across all of the panels are different.

exists a positive amplitude $\hat{A}$ such that $TP_{A,\omega}(t) \geq TP$ for $A \in \left[0, \hat{A}\right]$ and some values of t. Surprisingly, $TP_{A,\omega}(\bar{t})$, and $TP_{A,\omega}(\underline{t})$ may both exceed TP.

We find that for $A \in \left(0, \hat{A}\right)$, $R_{A,\omega}(t)$ can become larger than R (Figure 4.4). We know from Chapter 3 that an extended range can help the species retain larger population sizes. Yet, in the case of periodically fluctuating speeds, we see something novel in the profile: the global maximum of the density profile for the periodic travelling pulse is behind the trailing edge. This special profile of the "zombie" population (see Chapter 3) contributes to the increased total population.

The largest local maximum of the density profile occurs in the travelling pulse solution; i.e., when $A = 0$. Inside the suitable habitat, the population birth-death dynamics are governed by the logistic equation, thus growth is density-dependent. This translates into biomass production being highest at intermediate population levels, positive below carrying-capacity, zero at carrying capacity, and negative above carrying capacity. The progressive and recessive shifts of the suitable habitat together with movement between habitat types sustains the larger range. Inside the suitable habitat, there is less density dependence so that biomass production is higher. This mechanism is what sustains the larger total population. We elaborate on this mechanism in Section 4.5.

In the case of low frequency and low amplitude at the time when $TP_{A,\omega}(\underline{t})$ is obtained, the local maximum of the periodic travelling pulse can exceed that of the travelling pulse (Figure 4.4a), although we only see a marginal increase. At this time, $R_{A,\omega}$ measures close to R (Figure 4.4c) and the global maximum of the periodic travelling pulse is inside the suitable habitat. Once $TP_{A,\omega}(\bar{t})$ is achieved, the range is also extended (Figure 4.4c) and again, the highest local maximum of the periodic travelling pulse is below that of the travelling pulse, although it does remain inside the suitable habitat. (An illustration of the comparison is not shown.) In this case, the relative growth is incremental compared to cases where the local maximum is outside of the suitable habitat.

Biomass productivity is not the whole story. In these presented cases, the mortality rate is 10 times smaller than the growth rate inside the suitable habitat. This low mortality rate keeps the unsuitable habitat well-populated near the habitat edges, so that there are still many individuals present when the suitable habitat sweeps individuals back in as it shifts back and forth. We look at a case with higher mortality rates and compare it to one with lower mortality rates (Figure 4.5). In the case with higher mortality, $TP_{A,\omega}(\bar{t})$ (and consequently $TP_{A,\omega}(\underline{t})$) do not increase. In this case, we see that the global maximum of the density profile of the periodic travelling pulse remains inside the suitable habitat. Although the range increases, the global maximum has dropped enough due to the high mortality outside the suitable habitat, that the population suffers loss as a consequence of the fluctuation.

Higher frequencies can support larger maximum total populations (Figure 4.3).

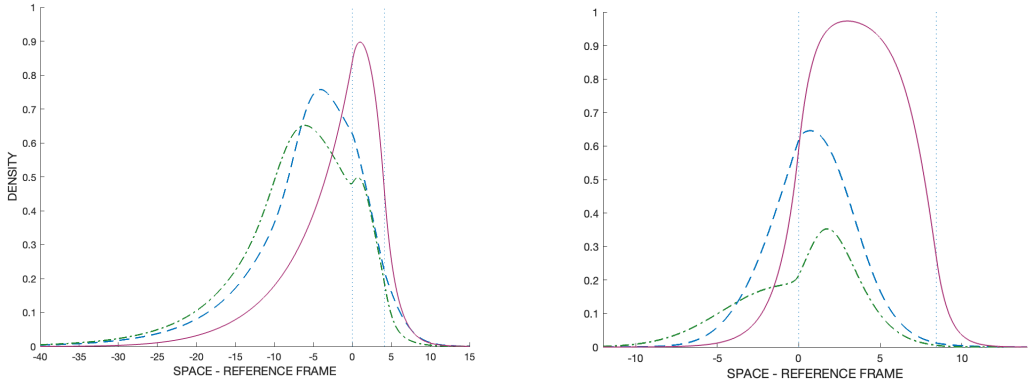

(a) Low mortality **(b)** High mortality

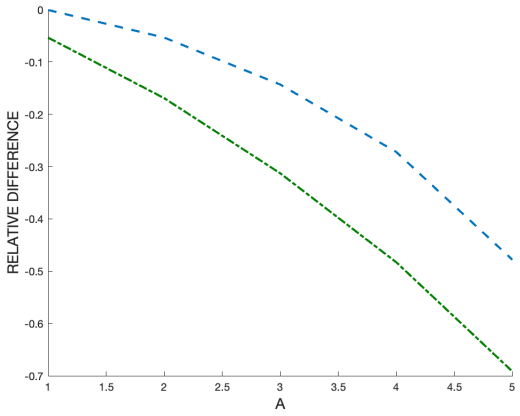

(c)

Figure 4.5: Top panels: The density profile at the time the population reaches $TP_{5,\omega}(\underline{t})$) (dash-dotted green) and $TP_{5,\omega}(\bar{t})$ (dashed blue) and the travelling pulse profile (purple solid). Panel (a): $m = 0.1$ and $L \approx 4.0745$. Panel (b): $m = 1$ and $L \approx 8.4345$. Panel (c): The relative difference between $TP_{A,\omega}(\bar{t})$ and TP (dashed blue) and $TP_{A,\omega}(\underline{t})$ and TP (dash-dotted green) for increasing A, with $m = 1$. Across all panels, other parameters are $c = 0.5$, $\omega = \frac{\pi}{2}$, $d_i = 1$, $i = 1, 2$, and $L = 5L^*$.

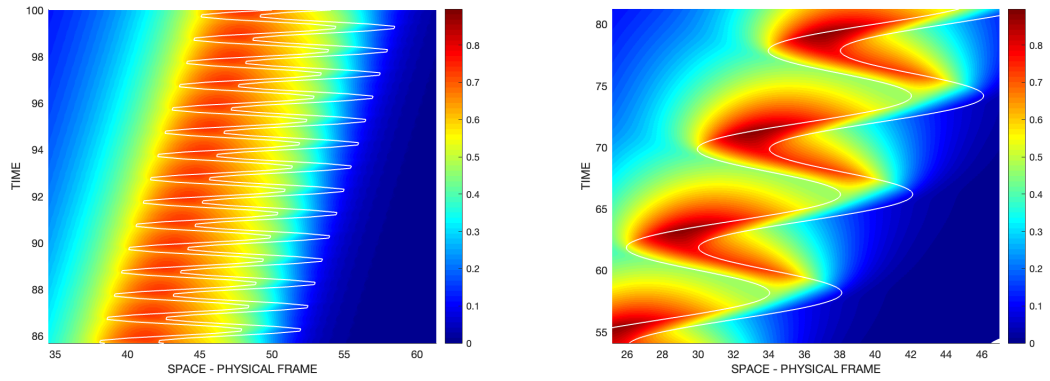

(a) **(b)**

Figure 4.6: Panel (a): An illustration of the averaging effect. Here, $A = 5$, and $\omega = 2\pi$. Panel (b): An illustration of the switch phenomenon. Here, $A = 5$, and $\omega = \pi/4$. In both these panels $c = 0.5$, and $L = 5L^* \approx 4.0745$. Across all panels, other model parameters are $\alpha = 0.5 = \beta$, $d_i = 1$, $m_i = 0.1$ for $i = 1, 2$. The colour bars across panels differ.

At high frequencies, suitable habitat progression and recession happen frequently. When paired with low mortality rates these mechanisms result in an averaging effect where $R_{A,\omega}(\bar{s}) - R_{A,\omega}(\underline{s})$ and $TP_{A,\omega}(\bar{t}) - TP_{A,\omega}(\underline{t})$ are small compared to the case of low frequencies and they can (when mortality is low enough) remain significantly higher than in the case of no variation. The high total populations are explained again via biomass production, as above.

Low frequencies matched with large amplitudes can cause the range to go through a switch phenomenon. This is when the highest density of the population outside of the suitable habitat is found in front of the leading edge during times of swift suitable habitat recession, and behind the trailing edge during times of swift suitable habitat progression (Figure 4.6b). Conversely, in a constant shift scenario when $A = 0$, the skew is always in the direction of the trailing edge.

Reminiscent of the results found in the previous section, for a given frequency, $TP_{A,\omega}(\bar{t})$ realises its maximum for larger A when c is smaller (Figure 4.3). This skew towards larger amplitudes given smaller average shifting speeds can be astonishing, as our numerical results show that this maximum can occur even when the amplitude of variation is larger than the length of the suitable habitat!

4.4 Varying Patch-Size

There are many ways of letting the patch size vary, e.g., by setting $A_1 \neq A_2$, $\omega_1 \neq \omega_2$, or $c_1 \neq c_2$. We concentrate on one extreme case only, the case where the two interfaces move in antiphase, that is we take $A_1 = A = -A_2$, where $A > 0$. In this case, the

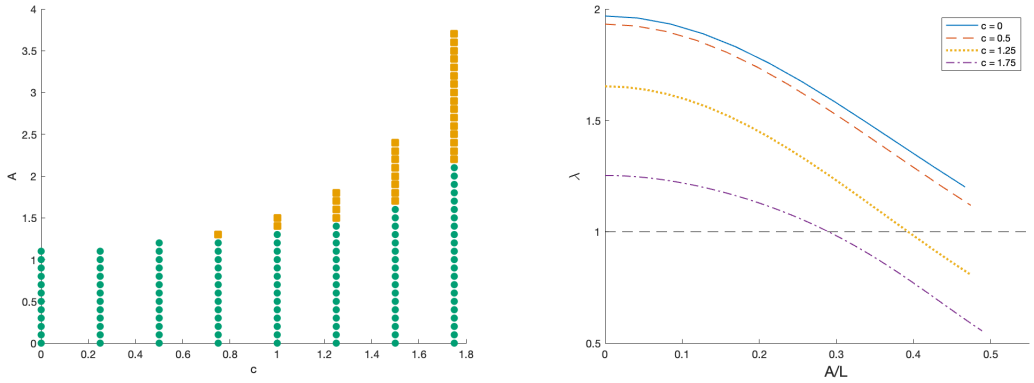

(a) **(b)**

Figure 4.7: The principal eigenvalue as a function of amplitude and average shifting speed. Panel (a): A green dot indicates that the population will persist ($\lambda > 1$), while an orange square indicates that the population will go to extinction ($\lambda < 1$). Panel (b): The principal eigenvalue as a function of $\bar{A}$ for shifting speeds, $c = 0$ (solid in blue), $c = 0.5$ (dashed in orange), $c = 1.25$ (dotted in yellow), and $c = 1.75$ (dash-dotted in purple). Other model parameters are: $d_i = 1$, $m_i = 1$, $\alpha = 0.5 = \beta$, and $L = 1.5L^*$.

suitable habitat alternates between times of expansion (interfaces moving away from each other) and times of contraction (interfaces moving towards each other). During times of contraction, one has to be careful with parameter choices so that the suitable habitat does not periodically disappear or the interfaces change their order on the real line. To satisfy these conditions we take

$$\omega_1 = \omega_2 = \omega, \quad c_1 = c_2 = c, \text{ and } A < \frac{L}{2}. \tag{4.4.1}$$

The average size of the suitable habitat is L. Since the frequency of the two interfaces is the same, solutions in the reference frame are still $\frac{2\pi}{\omega}$-periodic. We note that there are currently no analytical results on this setting with variable patch size.

4.4.1 Persistence Analysis

For the current scenario, we repeat the analysis that we did in Section 4.3.1; i.e., we numerically calculate the eigenvalue and determine the asymptotic outcome with regards to population persistence. Due to the conditions on amplitude, each column in the plot (Figure 4.7a) has a maximal amplitude where data above it is not missing, but rather not relevant according to the conditions (4.4.1).

We observe that the population either persists for all allowed values of A or there is a maximum value of $A = A^*$ for which it persists (Figure 4.7a). Periodic fluctuations do not necessarily push the eigenvalue below unity. In those cases, even

though the amplitude can be so large that the suitable habitat periodically gets close to vanishing, the population can survive overall. Given that individuals do not immediately die upon entering the unsuitable habitat, they return to the suitable habitat and contribute to future generations during times of suitable habitat growth.

The trailing edge plays a critical role in population persistence [39]. In this scenario, the trailing edge on its own has the same essential behaviour as the scenario presented in the previous section. That is, for any fixed speed, increasing the amplitude results in increasing the highest shifting speed. As the average shifting speed is increased, so is the patch-size (see Section 4.3.1), and the amplitude is permitted to increase to values corresponding to intermittent high speeds of shift that the population cannot withstand. Mathematically this corresponds to λ passing through the bifurcation point. Thus, at higher values of c we see the emergence of A^*. As we saw in Section 4.3.1, A^* is an increasing function of c.

Across the columns, the suitable habitat size L increases as a function of c. As before, we study the eigenvalue as a function of the amplitude relative to habitat length; i.e., $\lambda = \lambda(\bar{A})$. We find that λ is a decreasing function of $\bar{A}$ (Figure 4.7b). As in the case of a constant patch size, the point at which the curve passes through the bifurcation point ($\lambda = 1$) decreases as c increases. Thus, we conclude again that populations can withstand higher relative amplitudes in slower average shifting speeds.

4.4.2 Population Density

In this section, we are interested in how amplitude and frequency impact the population density, given that the population persists. We follow the same ideas as in Section 4.3.2 in that we study how amplitude and frequency impact total population levels, comparing always to the case when there is no variation ($A = 0$). We use the same notation as in the previous section.

We find that the maximum density, $TP_{A,\omega}(\bar{t})$, as a function of A can be humped shaped, particularly for low frequencies (Figure 4.8). That is, intermediate amplitudes paired with low frequencies support the largest maximum total populations. Conversely, $TP_{A,\omega}(\underline{t})$, is a decreasing function of A, and the lowest minima are associated with the lowest frequencies (Figure 4.8). Hence, large $TP_{A,\omega}(\bar{t})$ are typically associated with small $TP_{A,\omega}(\underline{t})$. As the frequency is increased, the largest $TP_{A,\omega}(\bar{t})$, occur for smaller amplitudes.

The population density spreads outward in both directions during times of suitable habitat expansion and contracts during times of suitable habitat contraction (Figure 4.9). In contrast to the case of a constant patch size, where the increase in $TP_{A,\omega}(\bar{t})$ is attributed to low mortality rates and global maxima occurring outside the suitable habitat, in the case of varying patch-size, the increase in $TP_{A,\omega}(\bar{t})$ is primarily due to the expansion of the suitable habitat.

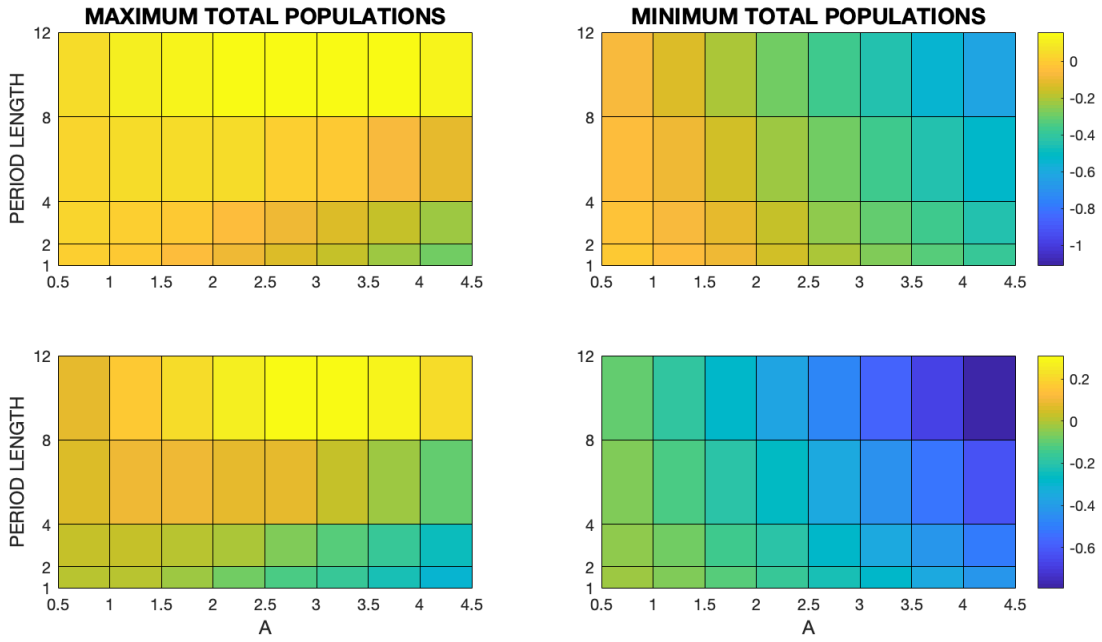

Figure 4.8: The relative difference between $TP_{A,\omega}(\bar{t})$, or $TP_{A,\omega}(\underline{t})$, and TP as functions of A and ω. Top panels: higher average shifting speed. Bottom panels: lower average shifting speed. Top panels: $c = 1$, $L = 5L^* \approx 10.5278$, and $TP \approx 9.3206$. Bottom panels: $c = 0.5$, $L = 5L^* \approx 8.4345$, and $TP \approx 7.8884$. Across all panels, other model parameters are $\alpha = 0.5 = \beta$, $d_i = 1$, $m_i = 1$ for $i = 1, 2$.

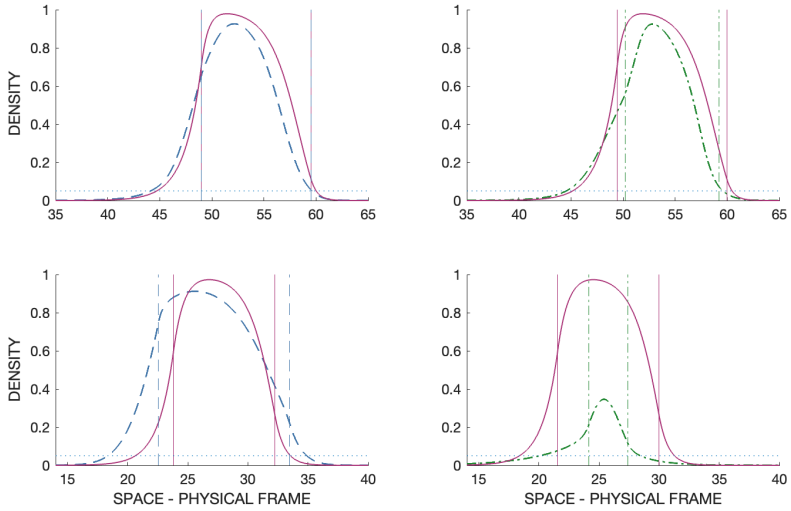

(a) Top: Intermediate average shifting speed, intermediate amplitude, high frequency. Bottom: Slow average shifting speed, large amplitude, low frequency.

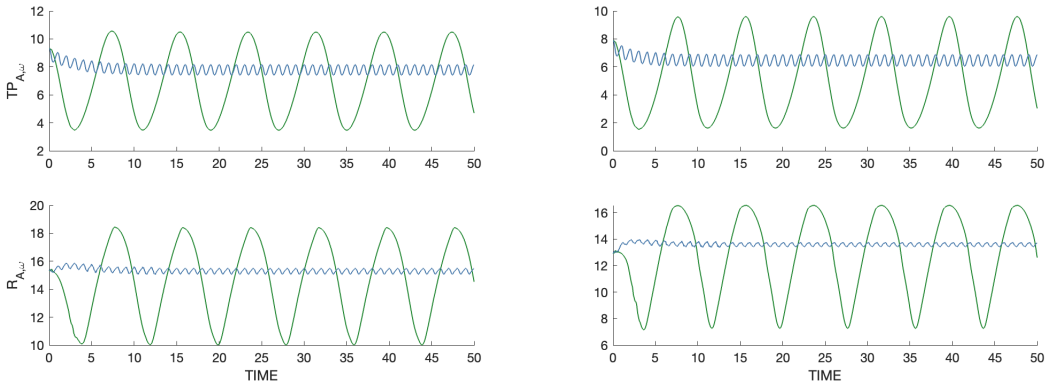

(b) **(c)**

Figure 4.9: Panel (a): The population density profiles at the time when $TP_{A,\omega}(\bar{t})$ (dashed in blue) and $TP_{A,\omega}(\underline{t})$ (dot-dashed in green) is achieved compared to the travelling pulse solution (solid in purple) Dotted horizontal lines indicate the range threshold. Vertical lines indicate the interfaces and are styled (solid/dashed/dot-dashed) according to their corresponding density profile. (Note that in the top left panel, these vertical lines overlap.) Top panels: $(A, \omega) = (2.5, 2\pi)$, $c = 1$ and $L = 5L^* \approx 10.5278$. Bottom panels: $(A, \omega) = (4, \frac{\pi}{4})$, $c = 0.5$ and $L = 5L^* \approx 8.4345$. Panels (b) and (c): Plots of $T_{A,\omega}(t)$ (across the top) and $R_{A,\omega}(t)$ (across the bottom). Blue (high frequency) curves and green (low frequency) curves correspond to model parameters $(A, \omega) = (2.5, 2\pi)$ and $(A, \omega) = (4, \pi/4)$, respectively. Panel (b): $c = 1$. Panel (c): $c = 0.5$. At $t = 0$, we plot the value of TP and R. Across all panels, other model parameters are $\alpha = 0.5 = \beta$, $d_i = 1$, $m_i = 1$ for $i = 1, 2$. The range threshold is 0.05. The axes across all of the panels are different.

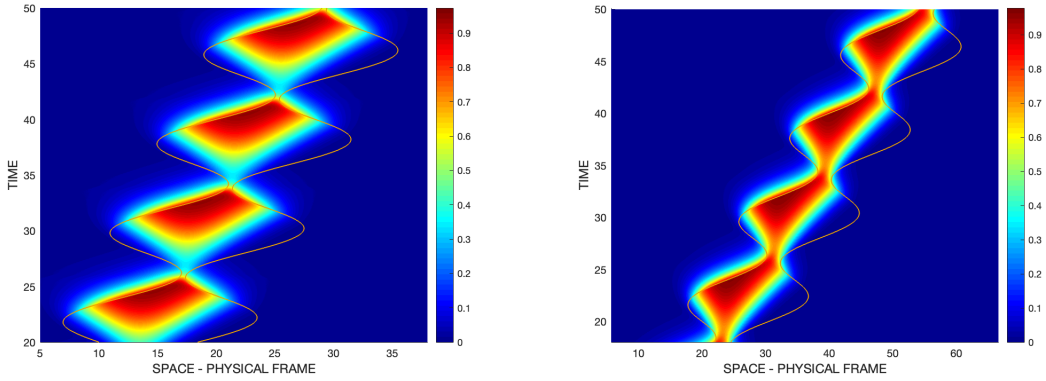

(a) Slow average shifting speed, large amplitude

(b) Intermediate average shifting speed, intermediate amplitude

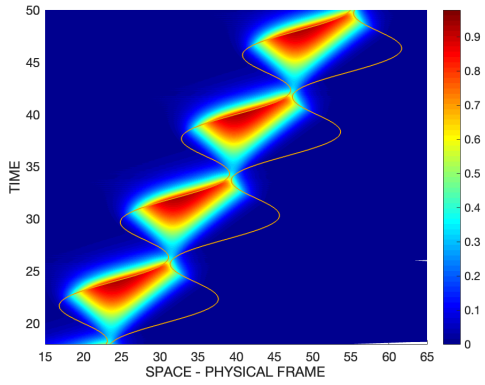

(c) Intermediate average shifting speed, large amplitude

Figure 4.10: The population density changing in time and space. Panel (a): $c = 0.5$, $A = 4$, and $L = 5L^* \approx 8.4345$. Panel (b): $c = 1$, $A = 4$, and $L = 5L^* \approx 10.5278$. Panel (c): $c = 1$, $A = 5$, $L = 5L^* \approx 10.5278$. Across all panels other model parameters are: $\omega = \frac{\pi}{4}$, $\alpha = 0.5 = \beta$, $d_i = 1$, $m_i = 1$ for $i = 1, 2$.

For larger amplitudes and low frequencies, a distinct travelling front periodically establishes (Figure 4.10). When the amplitude is large, the interfaces move swiftly out during times of habitat expansion and the majority of the population finds itself inside the suitable habitat. Thus, inside the suitable habitat, we see something akin to invasion dynamics, where the travelling fronts temporarily travel at the Fisher speed [21] (Figure 4.11). In invasion dynamics, the Fisher speed is the asymptotic speed at which a population can invade in a suitable habitat of infinite length [58]; see Chapter 1 for more detail on the Fisher speed. In our scaled model, the Fisher speed is $c_F = 2$. For two travelling fronts to appear (one pushing to the right and one pushing to the left), the amplitude must be large enough that the trailing edge moves faster than c_F during times of expansion so that the majority of the population is no longer interacting with the trailing edge. The two fronts are most pronounced when A is close to the maximum allowed A, as this coincides with very small population densities at the onset of expansion, due to the drastic loss of habitat during times of contraction; compare Figures 4.10b and 4.10c and Figures 4.11b and 4.11c. Yet, due to the average directional velocity of the interfaces, a travelling front can be established periodically at the leading edge for intermediate values of A (Figures 4.10b and 4.11b).

When the frequency is high, the averaging effect takes over, where we see that the differences $R_{A,\omega}(\bar{s}) - R_{A,\omega}(\underline{s})$ and $TP_{A,\omega}(\bar{t}) - TP_{A,\omega}(\underline{t})$ are relatively small compared to lower frequencies (Figure 4.9). Although $TP_{A,\omega}(\bar{t}) < TP$, the range my increase. The local maxima of the periodic travelling pulse are smaller than the local maximum of the travelling pulse and, in contrast to the constant patch size case, the local maximum remains inside the suitable habitat.

We find significant growth of $TP_{A,\omega}(\bar{t})$ for relatively higher mortality rates compared to the case when the patch size does not vary (Section 4.3.2). However, mortality does matter. Increasing the mortality rate and keeping approximately the ratio $A/L(m)$ constant, where $m_i = m$, $i = 1, 2$, $TP_{A,\omega}(\bar{t})$ decreases (Figure 4.12). Surprisingly, even when the mortality is larger than the growth rate, the relative difference of $TP_{A,\omega}(\bar{t})$ and TP can still be positive. During times of expansion, the suitable habitat length periodically exceeds the size of L, the length of the suitable habitat for the travelling pulse and the average length of the suitable habitat for the periodic travelling pulse. Following this expansion, the range also increases, and the suitable habitat is large enough that the bulk of the population remains inside the suitable habitat.

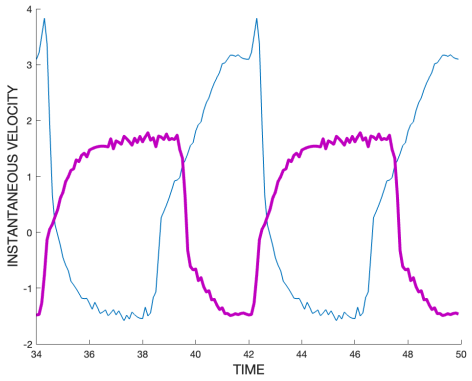

(a) Slow average shifting speed, large amplitude

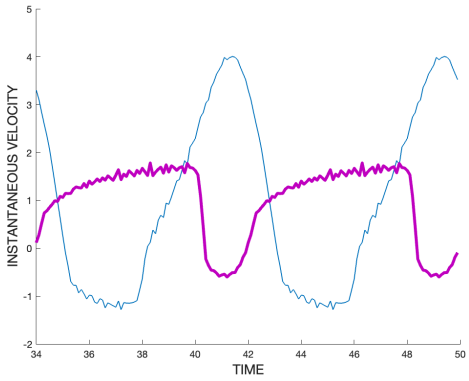

(b) Intermediate average shifting speed, intermediate amplitude

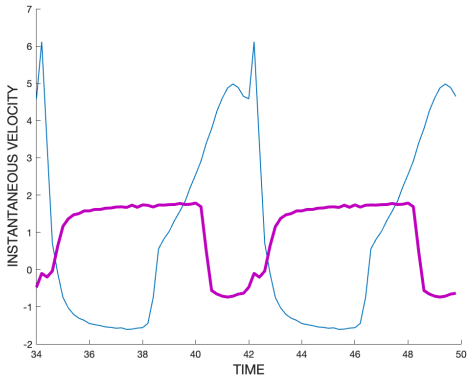

(c) Intermediate average shifting speed, large amplitude

Figure 4.11: The instantaneous velocity of the travelling fronts. Thin blue lines and thick magenta lines correspond to the left and right travelling fronts, respectively. These values are calculated by tracking level sets. Panel (a): $c = 0.5$, $A = 4$, and $L = 5L^* \approx 8.4345$. Panel (b): $c = 1$, $A = 4$, and $L = 5L^* \approx 10.5278$. Panel (c): $c = 1$, $A = 5$, and $L = 5L^* \approx 10.5278$. Other model parameters are: $\omega = \frac{\pi}{4}$, $d_i = 1$, $m_i = 1$, $\alpha = 0.5 = \beta$

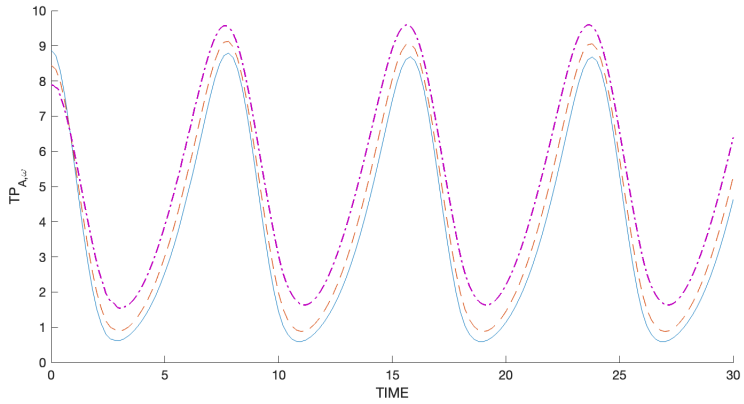

Figure 4.12: $TP_{A,\omega}$ as a function of time for $m_i = 1$ (dot-dashed in magenta), $m_i = 1.5$ (dashed in orange), and $m_i = 2$ (solid in blue), $i = 1, 2$. For each m_i, the relative differences of $TP_{A,\omega}(\bar{t})$ and TP, denoted by $Q(m)$ is: $Q(1) \approx 0.2161$, $Q(1.5) \approx 0.0665$, and $Q(2) \approx -0.0275$ Other model parameters are: $c = 0.5$, $L = 5L^*$, $A/L \approx 4.7$, $\omega = \frac{pi}{4}$, and $d_i = 1$, $i = 1, 2$.

4.5 Discussion

We studied how periodic variation in shifting speed and habitat size affects both the persistence outcome and the total population sizes. We studied persistence via the periodic mapping of the linearised system. We found that the eigenvalue is a decreasing function of the amplitude of variation, and, for large enough amplitudes, the eigenvalue will decrease below unity, which is the bifurcation point of the zero-steady state. Thus, we conclude that large enough variation can drive a species to extinction. Additionally, we found that populations undergoing relatively slower shifts can withstand larger amplitudes relative to habitat size. Since the eigenvalue is a decreasing function of amplitude, one would expect that, given persistence, populations exposed to variation would have smaller total population densities than populations not exposed to variation. Yet, we found that this is not always the case. Through our computational approach, we were able to identify parameter ranges that can support larger total populations than those in the absence of variation.

Our results in Section 4.3 show that there exist scenarios for which both $TP_{A,\omega}(\bar{t})$ and $TP_{A,\omega}(\underline{t})$ reach maxima at intermediate values of amplitude (A) and frequency (ω); i.e., their graphs as functions of A or ω are hump shaped. Similar results exist in [30] and [18]. In [30], Iglesias and Mirrahimi study a phenotypically structured population in a fluctuating and shifting trait space. In [18], Fang et al work in a moving habitat model framework that has only one interface across which the habitat types vary. In both papers, the authors show that variation can bring the average population size above the population size given no fluctuations. Yet, our result is stronger, as we show that the total population can remain higher for all time.

The higher population levels sustained in the periodic travelling pulse compared to that of the travelling pulse depend on the length of the suitable habitat and the mortality rate. Given smaller patch sizes, we saw that this effect is dampened, and for small enough patch sizes, the relative difference of $TP_{A,\omega}(\bar{t})$ and TP is negative. We took the scaled mortality rate to be $m_i = 0.1$. This low mortality rate together with individuals being reintroduced into the suitable habitat as it recesses and progresses, gives individuals, who would have been otherwise left behind, the opportunity to contribute to the population as they are reintroduced to the suitable habitat. If the unsuitable habitat is too harsh an environment (high mortality rates) variation has a negative effect on the total population size. This is similar to the results we presented in Chapter 3 where we showed that for low mortality rates there exists an intermediate shifting speed that can support a larger total population than when the suitable habitat is stationary (i.e. $c = 0$). Thus, if individuals can survive for a prolonged period of time in the unsuitable habitat, and if their suitable habitat is large enough, intermediate variation plus intermediate shifting speeds results in the highest population sizes.

The increase in overall biomass is attributed to the recession/progression pattern of the suitable habitat. This result is related to one of Zhang et al [63], who show that for intermediate values of dispersal rates over a heterogenous landscape, overall biomass is largest. They set up a series of patches over which the availability of resources changes. They found that emigration from the best patches to less resource-rich patches, keeps biomass productivity high in the most resourceful patches. In comparing the constant shifting speed scenario to that of the periodic shifting speed scenario, we see that back and forth shifting assists individuals in accessing suitable habitat where biomass productivity is high due to the decreased density dependence as a result of the shifting.

In contrast, Section 4.4.2 provides a different explanation for when $TP_{A,\omega}(\bar{t})$ exceeds TP. In this case, the average size of the suitable habitat is the size of the suitable habitat, L, corresponding to the travelling pulse solution, thus the suitable habitat size pulsates between sizes larger than and smaller than L. An increase in $TP_{A,\omega}(\bar{t})$ is largely attributed to the expanding fronts appearing during times of expansion, which occur when the frequency is low and the amplitude is high. In such a scenario, the suitable habitat expands at speeds larger than the Fisher speed, and the majority of the population is left within the suitable habitat. No longer interacting with the boundary, the population spreads in both directions at instantaneous speeds approximately equal to the Fisher speed. Even for relatively high mortality rates $TP_{A,\omega}(\bar{t})$ can still exceed TP, although there is a limit on how large the mortality can be in order to still see this effect. We did not find a scenario where $TP_{A,\omega}(\underline{t})$ exceeds TP, and we suspect that it always lies below, since these minimum population levels are associated with the suitable habitat shrinking below L.

Zhou and Fagan [64] studied the case of time-varying sizes in the absence of

an environmental shift in the context of integro-difference equations, a discrete-time, continuous-space framework. In such a framework, the population is updated at every time step according to an integral mapping that accounts for a sedentary stage and a dispersal stage. They prove that persistence can be measured by the largest eigenvalue of an associated linear operator, and that this eigenvalue is a decreasing function of the size of variation.

In their work, Zhou and Fagan also find the existence of a lower minimal limit size. They consider the case where the habitat size is 2-periodic and that there is a good season and bad season, where the habitat size is longer or shorter than the critical patch-size of the corresponding system without fluctuation. They identify conditions under which for a fixed habitat size in the good season, there exists a smallest habitat size in the bad season, below which the population will eventually go to extinction. The minimal limit size, which is a positive finite value, is the smallest habitat size in the bad season, when the habitat size for the good season approaches infinity. Although we did not look for such a value, our analysis hints at its existence. The persistence analysis shows that for fast enough speeds and high enough mortality there exists a critical amplitude above which the population goes extinct. However, our sinusoidal description of the interface movement means that habitat size minimums and maximums are both affected as the amplitude increases. Determining the corresponding values in the reaction diffusion framework that Zhou and Fagan found in the integro-difference framework is a compelling future direction.

The minimum total population size is particularly relevant when one considers the effect of rare extreme climatic events. Smaller population sizes are less resilient to such disturbances. Yet, reletive to current distributions, for example on temperature variability, extreme climate events are occurring more often [20]. The minimum viable population is the minimum population size with an acceptably low extinction probability over a given time interval [17]. Although in the previous sections, we focused our attention to the unexpected case of increased total population sizes, we also found that variation can decrease the total population size of the periodic travelling pulse over an entire period compared to a system without variation. Particularly, when the suitable habitat size is closer in size to the critical patch-size of the corresponding system with out variation. This suggests that minimum population levels could periodically be very vulnerable to stochastic events and, in the worst case, be extremely vulnerable almost all the time if the maximum population levels are also low as a consequence of variation. Alternatively, our results also show that variation can make a population more resilient against extreme climatic events whenever the parameters are such that $TP_{A,\omega}(\underline{t}) > TP$.

The maximum total population size is important when studying the effects of overpopulation. One example is large deer populations and the impact of overgrazing on ecosystems. Overgrazing can threaten the persistence of native plants, affect adults' ability to mature to their normal height and can result in invasions of exotic

plants. All of these processes can result in a disturbance that severely alters an ecosystem, for example by increasing the amount of light in a forest [29, 33]. Our results show that depending on the severity of the surrounding unsuitable habitat, periodic fluctuation can either increase or decrease maximum population levels. Thus, we conjecture that in unsuitable habitats that are not too harsh, variation may result in detrimental overgrazing of native plants. Conversely, if individuals do not survive long in the surrounding unsuitable habitat, then periodic fluctuation can in turn help sustain the native resources. Yet, to properly study such processes, one must consider a consumer and resource (or predator and prey) as dynamic variables in the model.

Predator-prey dynamics within moving-habitat models do not yet exist in the literature, although Fang et al [18] provide an epidemiological application of their system with a travelling wave connecting the epidemic steady state to the zero steady state. Additionally, river systems are similar to moving-habitat models in that they contain a similar advective term, which describes the river drift. Invasion dynamics in predator-prey systems refer to studying conditions when the prey and predator coexist, called the coexistence state. Hilker and Lewis [26] studied such dynamics in a river system of infinite length and found that the existence of such a state depends on the rivers advective speed experienced by each species. Studying invasion dynamics of a predator-prey system in a moving-habitat model is rife with options, including studying differing climatic niches or differing interaction with the habitat edge between predator and prey. Our numerical approach provides an excellent tool to commence such studies.

Another future direction of study would be to add stochasticity, for example, into the growth rate. Bourhours and Lewis [9] did just that in a different modelling framework, using integrodifference equations, where time is discrete and space is continuous. They investigated the impact of growth rate variation on a Canadian butterfly's persistence ability and concluded that larger variation has a negative impact on persistence. Integrodifference equations assume that growth and dispersal happen at different times, where as reaction-diffusion equations, as studied throughout this thesis, assume that these processes happen simultaneously. Stochastic growth rates coupled with a periodic shifting speed within our modelling framework is still open for investigation.

Finally, although we included in our model construction habitat-dependent dispersal rates ($d_1 \neq d_0 \neq 1$) and habitat preference ($\alpha \neq 0.5 \neq \beta$) we did not study their impact in this chapter. We conjecture that their impact on population dynamics may be similar to what we saw in Chapter 3. For example, that a high preference for the suitable habitat will help the population to persist at higher average shifting speeds, but that low preferences will likely sustain larger total population levels at lower average shifting speeds. We leave exploring such conjectures to future work.

Chapter 5

Two-dimensional Space

In the last two chapters we studied scenarios where a species lives in 1-dimensional space. This idealisation follows the assumption that heterogeneity in space only occurs in one direction. Naturally, this is not true. In this Chapter, we introduce a moving-habitat model in 2-dimensional space, while still incorporating habitat-dependent dispersal rates and habitat preference. This chapter is largely focused on the development of a finite element method to efficiently solve the system, with the difficulties arising from the movement of the boundary and the jump in density from the habitat-dependent movement behaviour.

5.1 Introduction

When concerned with the spatial spread of species, working in 2-dimensional space lends more flexibility to the scenarios one can study. For example, one can study space as being heterogeneous in all directions. In the rich literature of moving-habitat models, there is a subset committed to studying the case of two spatial dimensions. Within the reaction-diffusion framework, as early as the late 2000's, Berestycki and Rossi, proved the existence and uniqueness of travelling waves for a moving-habitat model in $n-$dimensional space [4, 5]. They assume that the favourable habitat is bounded and subject to a constant shift. In 2015, Ho determined conditions for the existence and uniqueness of travelling waves under a relaxed assumption on the boundedness of the suitable habitat [62]. More recently, Bouhours and Giletti, studied a more general reaction term, that allows for a weak Allee effect [8]. This is when the largest intrinsic growth rate happens for intermediate values of the density, which is not the case of the logistic function, which has a monotone decreasing intrinsic growth rate on $[0, \infty)$. In all cases, the focus is on finding conditions under which the population persists, and in all articles, a common result is the existence of critical shifting speed above which the population cannot persist. In the integro-difference framework, Phillips and Kot studied a two-dimensional moving-habitat model [46]. They found that a

limiting width of the habitat size can run a species to extinction. They state that the assumption of infinite width that implicitly accompanies a spatially 1-dimensional setting, leads to over estimations on persistence.

Understanding the conditions under which a population persists in a shifting habitat is foundational to theoretical ecology and conservation efforts. Yet, it alone doesn't provide information on how the shift impacts the population levels. Understanding how the population levels change as a consequence of the shift gives us a measure on a species susceptibility to external factors; see Section 4.5, where the importance of population density outcomes is discussed in detail. Studying transient dynamics, can assist conservation efforts in identifying high-risk populations; see Chapter 3 where we identify such parameter ranges and density profiles. Finally, thinking in terms of long-time behaviour, habitat-dependent movement behaviour affects the persistence outcome [39]. In this chapter, we develop a finite element method to study a 2-dimensional moving-habitat model that captures habitat-dependent dispersal rates and habitat preference.

We consider the whole space cut into two distinct domains, one a bounded domain, representing the suitable habitat, the other, the unbounded domain, the unsuitable habitat. The interface between these two domains represents the habitat edge, across which the suitability changes from good to bad. The habitat preference that we consider results in a jump in density across this interface. Finite element methods require the problem to first be restated in a weak form. In lieu of any special consideration, in the weak formulation the equations describing the jump in density across the interfaces appear as essential conditions, as they are strongly enforced in the solution space. In this decomposed domain, implementing such conditions is not obvious. Mortar hybrid methods allow these conditions to be weakly enforced through Lagrange multipliers; see for example [2]. In domain decomposition methods, this technique was introduced to enforce continuity across a boundary. Sacco et al, used Lagrange multipliers together with a finite element formulation called a Three-Field formulation in 3-dimensional space to enforce a comparable discontinuity of density [53]. In our case, we use it, without the Three-Field formulation to enforce the discontinuity in density. Developing a finite element method rather than a finite difference method, as done in Chapter 3, is largely motivated by the flexibility of the hybrid method to handle a decomposed domain with arbitrary interfaces.

This chapter is organised as follows: We start by introducing the 2-dimensional analogue of the moving-habitat model presented in Chapter 3, that is we consider arbitrary movement of the boundary and a jump in density across this boundary that is attributed to the habitat-dependent movement behaviour. We approach the movement of the boundary in the same spirit as we did in Chapter 3 in that we map the physical frame to a reference frame where the suitable habitat is then fixed in space. For a constant shift of the bounded domain, we develop a hybrid variational system and prove it is well-posed and equivalent to the original system. We then

develop a finite element method for this system, for which we obtain error estimates in the absence of a shift term. We implement our numerical scheme in FreeFEM++ [25]. For more general model parameters, we numerically validate our numerical scheme via comparison to the previously validated finite difference scheme developed in Chapter 3. We then apply our finite element method to a biologically motivated scenario.

5.2 The Model

The suitable habitat is now represented by $\boldsymbol{x} = (x, y) \in \Omega_0(t) \subset \mathbb{R}^2$, where $\Omega_0(t)$ is an open, bounded $\mathcal{C}^2$ boundary that is dependent on time, t. We denote its closure by $\bar{\Omega}_0(t)$. The complement of its closure, $\Omega_1(t) = \mathbb{R}^2 \backslash \bar{\Omega}_0(t)$, represents the unsuitable habitat. The interface, $\Gamma(t) = \bar{\Omega}_0(t) \backslash \Omega_0(t)$, represents the habitat edge between the suitable and unsuitable habitat.

The density of the population over space and time is denoted by $u(x, y, t)$ and we denote the restriction of u to Ω_i as

$$u|_{\Omega_i} = u_i, \quad i = 0, 1.$$

We assume that population dynamics and dispersal happen simultaneously and on the same time scale. Thus, the system representing the population dynamics over space and time is

$$\partial_t u_0 = D_0 \Delta u_0 + u_0(r - a u_0), \qquad \text{in } \Omega_0(t), \tag{5.2.1a}$$

$$\partial_t u_1 = D_1 \Delta u_1 - m_1 u_1, \qquad \text{in } \Omega_1(t), \tag{5.2.1b}$$

with interface conditions

$$u_0 = k u_1, \qquad \text{on } \Gamma(t), \tag{5.2.1c}$$

$$D_0 \partial_{\boldsymbol{\nu}} u_0 + u_0 \boldsymbol{c} \cdot \boldsymbol{\nu} = D_1 \partial_{\boldsymbol{\nu}} u_1 + u_1 \boldsymbol{c} \cdot \boldsymbol{\nu}, \qquad \text{on } \Gamma(t), \tag{5.2.1d}$$

and asymptotic conditions at infinity

$$\lim_{|\boldsymbol{x}| \to \infty} u(x, y, t) = 0. \tag{5.2.1e}$$

The operator Δ is the Laplacian; i.e., $\Delta u = u_{xx} + u_{yy}$. The coefficients D_i are the constant diffusion rates, r is the intrinsic growth rate, a is the intraspecific competition coefficient, m_i is the mortality rate, $c = c(x, y, t)$ is the velocity of $\Gamma(t)$, and the proportionality constant across the interface in equation (5.2.1c) is

$$k = k(x, y) = \frac{\alpha(x, y)}{1 - \alpha(x, y)} \sqrt{\frac{D_1}{D_0}}.$$

Here, α represents the probability that an individual enters the suitable habitat when at a point on the interface. The variable $\boldsymbol{\nu}$ denotes the unit normal pointing outward from $\Omega_0(t)$ into $\Omega_1(t)$, and consequently, $-\boldsymbol{\nu}$ is the corresponding unit normal pointing outward from $\Omega_1(t)$. We denote by $\partial \cdot / \partial \boldsymbol{\nu}$ the unit normal derivative on $\Gamma(t)$.

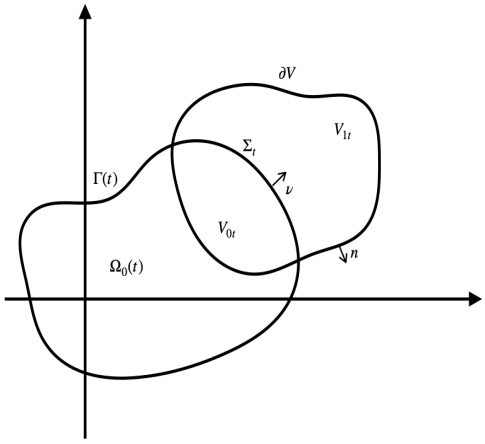

Figure 5.1: A control volume V intersecting with $\Omega_0(t)$.

5.2.1 Deriving the Flux Condition: Equation (5.2.1d)

Let V denote an arbitrary open control volume. Then, from conservation laws, the change of mass in the control volume V is equal to the diffusive flux across the boundary plus the change in mass due to the source term; i.e.,

$$\frac{d}{dt}\int_V u\mathrm{d}\boldsymbol{x} = -\int_{\partial V} F(u)\cdot n\mathrm{d}\boldsymbol{x} + \int_V G(u)\mathrm{d}\boldsymbol{x} \tag{5.2.2}$$

where ∂V denotes the boundary of V, n denotes the outward pointing unit normal on ∂V, $F(u) = -D(x,y)\nabla u$ (Fick's Law for diffusive flux), $D(x,y) = D_i$, on $\Omega_i(t)$, and

$$G(u) = \begin{cases} u(r-au), & \text{on } \Omega_0(t), \\ -mu, & \text{on } \Omega_1(t). \end{cases}$$

Let $\Sigma_t = \Gamma(t)\cap V$, $V_{it} = \Omega_i(t)\cap V$, for $i = 0, 1$. From the previous definitions of $\boldsymbol{\nu}$ and Σ, $\boldsymbol{\nu}$ is also the unit normal pointing from V_{0t} into V_{1t}. Similarly, c is the velocity of Σ_t.

The left-hand side of equation (5.2.2) is then

$$\begin{aligned}
\frac{d}{dt}\int_V u\mathrm{d}\boldsymbol{x} &= \sum_{i=0}^{1}\frac{d}{dt}\int_{V_i} u\mathrm{d}\boldsymbol{x}, \\
&= \sum_{i=0}^{1}\int_{V_{it}} u_{it}\mathrm{d}\boldsymbol{x} + \int_{\Sigma_t} u_0\boldsymbol{c}\cdot\boldsymbol{\nu}\mathrm{d}S - \int_{\Sigma_t} u_1\boldsymbol{c}\cdot\boldsymbol{\nu}\mathrm{d}S, \\
&= \sum_{i=0}^{1}\left[\int_{V_{it}} D_i\Delta u_i\mathrm{d}\boldsymbol{x} + \int_{V_{it}} G(u_i)\mathrm{d}\boldsymbol{x}\right]
\end{aligned}$$

$$
\begin{aligned}
&+ \int_{\Sigma_t} u_0 \boldsymbol{c}\cdot\boldsymbol{\nu}\mathrm{d}S - \int_{\Sigma_t} u_1 \boldsymbol{c}\cdot\boldsymbol{\nu}\mathrm{d}S,\\
&= \sum_{i=0}^{1}\left[\int_{\partial V_{it}\cap\partial V} D_i\frac{\partial u_i}{\partial n}\mathrm{d}S + \int_{V_{it}} G(u_i)\mathrm{d}\boldsymbol{x}\right] + \int_{\Sigma_t} D_0\partial_{\boldsymbol{\nu}}u_0\mathrm{d}S\\
&\quad - \int_{\Sigma_t} D_1\partial_{\boldsymbol{\nu}}u_1\mathrm{d}S + \int_{\Sigma_t} u_0\boldsymbol{c}\cdot\boldsymbol{\nu}\mathrm{d}S - \int_{\Sigma_t} u_1\boldsymbol{c}\cdot\boldsymbol{\nu}\mathrm{d}S,\\
&= -\int_{\partial V} F(u)\cdot n\mathrm{d}\boldsymbol{x} + \int_V G(u)\mathrm{d}\boldsymbol{x} + \int_{\Sigma_t} D_0\partial_{\boldsymbol{\nu}}u_0\mathrm{d}S\\
&\quad - \int_{\Sigma_t} D_1\partial_{\boldsymbol{\nu}}u_1\mathrm{d}S + \int_{\Sigma_t} u_0\boldsymbol{c}\cdot\boldsymbol{\nu}\mathrm{d}S - \int_{\Sigma_t} u_1\boldsymbol{c}\cdot\boldsymbol{\nu}\mathrm{d}S. \qquad (5.2.3)
\end{aligned}
$$

The second line is an application of the differentiation formula for moving regions; see Appendix C of [16]. (In fluid dynamics, this differentiation formula is often called Reynold's Transport Theorem [36]) Thus, from equations (5.2.2) and (5.2.3)

$$\int_{\Sigma_t} D_0\partial_{\boldsymbol{\nu}}u_0\mathrm{d}S - \int_{\Sigma_t} D_1\partial_{\boldsymbol{\nu}}u_1\mathrm{d}S + \int_{\Sigma_t} u_0\boldsymbol{c}\cdot\boldsymbol{\nu}\mathrm{d}S - \int_{\Sigma_t} u_1\boldsymbol{c}\cdot\boldsymbol{\nu}\mathrm{d}S = 0.$$

Since V is arbitrary, it follows that

$$D_0\partial_{\boldsymbol{\nu}}u_0 + u_0\boldsymbol{c}\cdot\boldsymbol{\nu} = D_1\partial_{\boldsymbol{\nu}}u_1 + u_1\boldsymbol{c}\cdot\boldsymbol{\nu}, \quad \boldsymbol{x}\in\Gamma(t).$$

One can derive the same equation through similar calculations by stating that mass is conserved over $\mathbb{R}^2$ in the absence of population dynamics, as we previously did in [39].

5.3 Change of Variable

Just as in the one dimensional case, we rewrite our system onto a reference frame, wherein we will build our numerical scheme. To do so, we follow [19]. We can write equations (5.2.1a) - (5.2.1b) efficiently as

$$u_t = D_i\Delta u + G(u), \quad \text{in } \mathbb{R}^2\backslash\Gamma(t), \qquad (5.3.1)$$

where $i = 0$, in $\Omega_0(t)$ and $i = 1$, in $\Omega_1(t)$. We assume that for each $t\in[0,T]$, that the moving domain, $\bar{\Omega}_0(t)$, is the image of a reference stationary domain $\bar{\Omega}_0'$. That is, there exists mappings x and y such that

$$\bar{\Omega}_0(t) = \left\{(x,y)\in\mathbb{R}^2 \mid x = x(\xi,\eta,t),\ y = y(\xi,\eta,t),\ (\xi,\eta)\in\bar{\Omega}_0'\right\},$$

where $\bar{\Omega}_0'\subset\mathbb{R}^2$ is independent of time and Ω_0' is open and bounded. We define $\Omega_1' := \mathbb{R}^2\backslash\bar{\Omega}_0'$ and $\Gamma' := \bar{\Omega}_0'\backslash\Omega_0$. We assume that all functions involved are smooth enough so that the inverse mappings, $\xi = \xi(x,y,t)$ and $\eta = \eta(x,y,t)$, exist.

We set $w(\xi(x,y,t),\eta(x,y,t),t) = u(x,y,t)$, where $w = w_i(\xi,\eta,t)$, for $(\xi,\eta) \in \Omega_i'$. Then, using the chain rule, we compute the first-order temporal partial derivative

$$u_t = w_t + w_\xi \xi_t + w_\eta \eta_t = w_t + (\mathbf{a}\cdot\nabla_{\xi,\eta})w, \tag{5.3.2}$$

with $\mathbf{a} = (\xi_t, \eta_t)$. The first-order spatial partial derivatives are

$$u_x = w_\xi \xi_x + w_\eta \eta_x, \tag{5.3.3}$$
$$u_y = w_\xi \xi_y + w_\eta \eta_y. \tag{5.3.4}$$

We assume that $w_{\xi\eta} = w_{\eta\xi}$, so that the second-order spatial partial derivatives are

$$u_{xx} = w_{\xi\xi}(\xi_x)^2 + w_\xi \xi_{xx} + w_{\eta\eta}(\eta_x)^2 + w_\eta \eta_{xx} + 2w_{\xi\eta}\xi_x\eta_x, \tag{5.3.5}$$
$$u_{yy} = w_{\xi\xi}(\xi_y)^2 + w_\xi \xi_{yy} + w_{\eta\eta}(\eta_y)^2 + w_\eta \eta_{yy} + 2w_{\xi\eta}\xi_y\eta_y. \tag{5.3.6}$$

Therefore, the dynamics in the $(\xi,\eta,t)-$coordinate system are

$$\begin{aligned} w_t = D\left(x(\xi,\eta,t), y(\xi,\eta,t)\right)\left[w_{\xi\xi}\left((\xi_x)^2 + (\xi_y)^2\right) + w_{\eta\eta}\left((\eta_x)^2 + (\eta_y)^2\right)\right. \\ \left. + w_\xi \Delta\xi + w_\eta \Delta\eta + 2w_{\xi\eta}\left(\xi_x\eta_x + \xi_y\eta_y\right)\right] - (\mathbf{a}\cdot\nabla_{\xi,\eta})w + G(w), \quad (\xi,\eta) \in \mathbb{R}^2\backslash\Gamma'. \end{aligned} \tag{5.3.7}$$

For the flux condition, we have that

$$\partial_{\boldsymbol{\nu}} u_i = (\boldsymbol{\nu}\cdot\nabla)\, u,$$

where $\nabla = (\partial_x, \partial_y)$. Therefore, the flux condition in the (ξ,η,t)-coordinate system is

$$D_0(\boldsymbol{\nu}\cdot\nabla)w_0 + w_0 \boldsymbol{c}\cdot\boldsymbol{\nu} = D_1(\boldsymbol{\nu}\cdot\nabla)w_1 + w_1\boldsymbol{c}\cdot\boldsymbol{\nu}, \quad (\xi,\eta) \in \Gamma', \tag{5.3.8}$$

where

$$(\boldsymbol{\nu}\cdot\nabla)w_i = w_{i\xi}\left(\nu_1\xi_x + \nu_2\xi_y\right) + w_{i\eta}\left(\nu_1\eta_x + \nu_2\eta_y\right).$$

With these mappings, the proportionality constant in the density-matching condition becomes $\kappa(\xi,\eta,t) = k(x(\xi,\eta,t), y(\xi,\eta,t))$.

We present some examples.

Example 5.3.1. We start with a rectangular domain moving in the $x-$direction

$$\Omega_0(t) = \{(x,y) \in \mathbb{R}^2 \mid ct < x < L + ct, -1 < y < 1\},$$

and

$$\Gamma(t) = \{(x,y) \in \mathbb{R}^2 \mid x = ct, L + ct, \text{ and } y = \pm 1\}.$$

The velocity of $\Gamma(t)$ is $(c,0)$. In this case, $\xi = x - ct$, $\eta = y$ and consequently

$$\Omega_0' = \{(\xi,\eta) \in \mathbb{R}^2 \mid 0 < \xi < L, -1 < \eta < 1\}$$

and

$$\Gamma' = \{(\xi, \eta) \in \mathbb{R}^2 \mid \xi = 0, 1, \text{ and } \eta = \pm 1\}.$$

The first-order partial derivatives of ξ and η are

$$\begin{aligned} \xi_t &= -c, & \xi_x &= 1, & \xi_y &= 0, \\ \eta_t &= 0, & \eta_x &= 0, & \eta_y &= 1. \end{aligned}$$

The second-order partial derivatives all vanish. Setting $w(\xi, \eta, t) = u(x, y, t)$, we find

$$w_t = D(\xi + ct, \eta)\Delta_{\xi,\eta} w + cw_\xi + G(w), \quad (\xi, \eta) \in \mathbb{R}^2 \backslash \Gamma'. \tag{5.3.9}$$

The flux condition is

$$D_0 w_{0\eta} = D_1 w_{1\eta}, \quad (\xi, \eta) \in \ell_1, \tag{5.3.10}$$
$$D_0 w_{0\xi} + cw_0 = D_1 w_{1\xi} + cw_0, \quad (\xi, \eta) \in \ell_2, \tag{5.3.11}$$
$$D_0 w_{0\eta} = D_1 w_{1\eta}, \quad (\xi, \eta) \in \ell_3, \tag{5.3.12}$$
$$D_0 w_{0\xi} cw_0 = D_1 w_{1\xi} + cw_0, \quad (\xi, \eta) \in \ell_2, \tag{5.3.13}$$

where

$$\ell_1 = \{(\xi, \eta) \mid \xi \in (0, 1), \eta = -1\}, \tag{5.3.14}$$
$$\ell_2 = \{(\xi, \eta) \mid \xi = 1, \eta \in (-1, 1)\}, \tag{5.3.15}$$
$$\ell_3 = \{(\xi, \eta) \mid \xi \in (0, 1), \eta = 1\}, \tag{5.3.16}$$
$$\ell_4 = \{(\xi, \eta) \mid \xi = 0, \eta \in (-1, 1)\}. \tag{5.3.17}$$

The density matching condition is

$$w_0 = k(\xi + ct, \eta)w_1, \quad (\xi, \eta) \in \Gamma'.$$

□

Example 5.3.2. Now we consider a circular domain moving at some constant velocity vector

$$\Omega_0(t) = \{(x, y) \in \mathbb{R}^2 \mid (x - c_1 t)^2 + (y - c_2 t)^2 < 1\}$$

and

$$\Gamma(t) = \{(x, y) \in \mathbb{R}^2 \mid (x - c_1 t)^2 + (y - c_2 t)^2 = 1\}.$$

The velocity of $\Gamma(t)$ is $c = (c_1, c_2)$. The change of variable is $\xi = x - c_1 t$ and $\eta = y - c_2 t$. Consequently, Ω_0' is the unit disc, $\xi^2 + \eta^2 < 1$, and Γ' is the unit circle. The first-order partial derivatives are

$$\begin{aligned} \xi_t &= -c_1, & \xi_x &= 1, & \xi_y &= 0, \\ \eta_t &= -c_2, & \eta_x &= 0, & \eta_y &= 1. \end{aligned} \tag{5.3.18}$$

Again, all second-order partial derivatives vanish. Setting $w(\xi,\eta,t) = u(x,y,t)$, we find

$$w_t = D(\xi + c_1 t, \eta + c_2 t)\Delta_{\xi,\eta} w + c_1 w_\xi + c_2 w_\eta + G(w), \quad (\xi,\eta) \in \mathbb{R}^2 \backslash \Gamma'. \tag{5.3.19}$$

The flux condition is

$$D_0\left(\xi w_{0\xi} + \eta w_{0\eta}\right) + w_0\left(c_1\xi + c_2\eta\right) = D_1\left(\xi w_{1\xi} + \eta w_{1\eta}\right) + w_1\left(c_1\xi + c_2\eta\right), \quad (\xi,\eta) \in \Gamma'. \tag{5.3.20}$$

and the density condition is

$$w_0 = k(\xi + c_1 t, \eta + c_2 t) w_1, \quad (\xi,\eta) \in \Gamma'.$$

□

Example 5.3.3. We generalize the second example. We consider an open, bounded domain $\Omega_0(t)$ where the outward unit normal is known on $\Gamma(0)$. If Ω_0 moves only by linear translations $x - c_1 t$ and $y - c_2 t$ then $c = (c_1, c_2)$. At any point (x', y') on $\Gamma(t)$ the outward unit normal is equal to the outward unit normal at $(x' - c_1 t, y' - c_2 t)$ on $\Gamma(0)$. Furthermore, the change of variable $\xi = x - c_1 t$ and $\eta = y - c_2 t$ sets $\Omega_0' = \Omega_0(0)$ and $\Gamma' = \Gamma(0)$. The first-order partial derivatives are as in (5.3.18) and therefore, all second-order partial derivatives vanish.

Setting $w(\xi,\eta,t) = u(x,y,t)$, we find

$$w_t = D'(\xi,\eta)\Delta_{\xi,\eta} w + c_1 w_\xi + c_2 w_\eta + G(w), \quad (\xi,\eta) \in \mathbb{R}^2 \backslash \Gamma', \tag{5.3.21}$$

where $D'(\xi,\eta) := D(\xi + c_1 t, \eta + c_2 t)$. The flux condition is

$$D_0\left(\nu_1 w_{0\xi} + \nu_2 w_{0\eta}\right) + w_0\left(c_1\nu_1 + c_2\nu_2\right) = D_1\left(\nu_1 w_{1\xi} + \nu_2 w_{1\eta}\right) + w_1\left(c_1\nu_1 + c_2\nu_2\right), \quad (\xi,\eta) \in \Gamma', \tag{5.3.22}$$

and the density condition is

$$w_0 = k(\xi + c_1 t, \eta + c_2 t) w_1, \quad (\xi,\eta) \in \Gamma'.$$

□

Going forward, we set $\xi = x$ and $\eta = y$, and simplify notation by dropping all prime notation. From now on we assume boundary shifts of the form as in Example 5.3.3. We focus our attention to finding solutions to the system

$$\partial_t w = d_i \Delta w + (\boldsymbol{c} \cdot \nabla) w + G(w), \qquad \text{in } \mathbb{R}^2 \backslash \Gamma, \tag{5.3.23}$$

$$w_0 = \kappa(x,y) w_1, \qquad \text{on } \Gamma, \tag{5.3.24}$$

$$d_0\partial_{\boldsymbol{\nu}} w_0 + (\boldsymbol{c}\cdot\boldsymbol{\nu})w_0 = d_1\partial_{\boldsymbol{\nu}} w_1 + (\boldsymbol{c}\cdot\boldsymbol{\nu})w_1, \qquad \text{on } \Gamma, \tag{5.3.25}$$

$$w_1 \to 0, \text{ as } |(x,y)| \to \infty, \tag{5.3.26}$$

and

$$G(w) = \begin{cases} w(r-aw), & \text{in } \Omega_0, \\ -mw, & \text{in } \Omega_0. \end{cases}$$

5.4 Semi-discrete Variational Formulations

We are mainly interested in the spatial discretisation of our model. Particularly, our goal is to derive a scheme that can treat the interface conditions. We approximate the time derivative so that $\partial_t w \approx \frac{w^{n+1}-w^n}{\tau}$, where τ is the time step. We use a forward-backward Euler scheme; i.e., we take all the linear terms and the nonlinear term at the $(n+1)^{th}$ time step and the n^{th} time step, respectively. Then the system at every time step becomes

$$\frac{w^{n+1}}{\tau} - d_i\Delta w^{n+1} - (\boldsymbol{c}\cdot\nabla)w^{n+1} = G(w^n) + \frac{w^n}{\tau}, \qquad \text{on } \mathbb{R}^2\backslash\Gamma, \tag{5.4.1}$$

$$w_0^{n+1} = \kappa w_1^{n+1}, \qquad \text{on } \Gamma, \tag{5.4.2}$$

$$d_0\partial_{\boldsymbol{\nu}} w_0^{n+1} + (\boldsymbol{c}\cdot\boldsymbol{\nu})w_0^{n+1} = d_1\partial_{\boldsymbol{\nu}} w_1^{n+1} + (\boldsymbol{c}\cdot\boldsymbol{\nu})w_1^{n+1}, \qquad \text{on } \Gamma, \tag{5.4.3}$$

$$w_1^{n+1} \to 0, \text{ as } |\boldsymbol{x}| \to \infty. \tag{5.4.4}$$

For our variational formulation we take Ω to be a bounded domain. We let $\Omega = \Omega_0 \cup \Omega_1 \cup \Gamma$. We assume homogeneous Dirichlet boundary conditions on the boundary of Ω, which we denote by $\partial\Omega$. That is, we consider the system

$$\frac{w^{n+1}}{\tau} - d_i\Delta w^{n+1} - (\boldsymbol{c}\cdot\nabla)w^{n+1} = G(w^n) + \frac{w^n}{\tau}, \qquad \text{on } \Omega\backslash\Gamma, \tag{5.4.5}$$

$$w_0^{n+1} = \kappa w_1^{n+1}, \qquad \text{on } \Gamma, \tag{5.4.6}$$

$$d_0\partial_{\boldsymbol{\nu}} w_0^{n+1} + (\boldsymbol{c}\cdot\boldsymbol{\nu})w_0^{n+1} = d_1\partial_{\boldsymbol{\nu}} w_1^{n+1} + (\boldsymbol{c}\cdot\boldsymbol{\nu})w_1^{n+1}, \qquad \text{on } \Gamma, \tag{5.4.7}$$

$$w_1 = 0, \qquad \text{on } \partial\Omega. \tag{5.4.8}$$

For the sake of our proofs, we assume that both c and κ are constant, and that $\kappa > 0$. With this formulation, we are no longer looking at a nonlinear problem, as the left-hand side containing the nonlinearity of the problem is known at every time step. Going forward, we replace w^{n+1} with w and $G(w_i^n) + \frac{w_i^n}{\tau}$ with g_i. Our proofs hold for any $g_i \in L^2(\Omega_i)$.

Let

$$X = \{v \in L^2(\Omega) : v|_{\Omega_i} \in H_*^1(\Omega_i)\} \equiv \Pi_{i=0}^1 H_*^1(\Omega_i),$$

where $H^1_*(\Omega_0) = H^1(\Omega_0)$ and $H^1_*(\Omega_1) = H^1_{\partial\Omega,0}(\Omega_1) = \{v \in H^1(\Omega_1) : v = 0 \text{ on } \partial\Omega\}$. We endow the space X with the norm

$$\|v\|_X = \left(\sum_{i=0}^{1} \|u_i\|^2_{H^1(\Omega_i)}\right)^{\frac{1}{2}}.$$

We are now ready to derive a weak formulation. In the following sections, we derive multiple weak formulations. We start with two variational formulations using different bilinear forms. We make clear the reason for doing so later on.

5.4.1 Bilinear Variational Formulation

For a function $w \in X$, we denote the restriction of w to Ω_i as $w_i = w|_{\Omega_i}$. Let

$$\mathcal{V}_\kappa = \{v \in X : v_0 = \kappa v_1 \text{ on } \Gamma \text{ and } v = 0 \text{ on } \partial\Omega\},$$

and let

$$\mathcal{V}_1 = \{v \in X : v_0 = v_1 \text{ on } \Gamma \text{ and } v = 0 \text{ on } \partial\Omega\} = H^1_0(\Omega).$$

The last equality results from the fact that $v_0 = v_1$ on Γ. We multiply Equation (5.4.5) by $v \in \mathcal{V}_1$, integrate, and find the relation

$$\sum_{i=0}^{1} \int_{\Omega_i} \left[-d_i \Delta w_i - \boldsymbol{c} \cdot \nabla w_i + \frac{w_i}{\tau}\right] v_i \, \mathrm{d}\boldsymbol{x} = \sum_{i=0}^{1} \int_{\Omega_i} g_i v \, \mathrm{d}\boldsymbol{x}. \tag{5.4.9}$$

We apply Green's formula and integration-by-parts to the left-hand side of this equation and obtain the following:

$$\begin{aligned}
\text{LHS} &= \sum_{i=0}^{1} \int_{\Omega_i} d_i \nabla w_i \nabla v_i + (\boldsymbol{c} \cdot \nabla v_i + \frac{v_i}{\tau}) w_i \, \mathrm{d}\boldsymbol{x} \\
&\quad + \int_\Gamma \left(d_1 \partial_{\boldsymbol{\nu}} w_1 + (\boldsymbol{c} \cdot \boldsymbol{\nu}) w_1 - d_0 \partial_{\boldsymbol{\nu}} w_0 - (\boldsymbol{c} \cdot \boldsymbol{\nu}) w_0\right) v \, \mathrm{d}s, \\
&= \sum_{i=0}^{1} \int_{\Omega_i} d_i \nabla w_i \nabla v_i + (\boldsymbol{c} \cdot \nabla v_i + \frac{v_i}{\tau}) w_i \, \mathrm{d}\boldsymbol{x}.
\end{aligned}$$

Here, the boundary terms vanish since $v_1 = v_0$ on Γ and w satisfies Equation (5.4.7). Thus, we have derived our first variational problem, which we call (**P**) .

(P) Find $w \in \mathcal{V}_\kappa$ such that

$$\sum_{i=0}^{1} \int_{\Omega_i} d_i \nabla w_i \nabla v_i + (\boldsymbol{c} \cdot \nabla v_i + \frac{v_i}{\tau}) w_i \, \mathrm{d}\boldsymbol{x} = \sum_{i=0}^{1} \int_{\Omega_i} g_i v \, \mathrm{d}\boldsymbol{x}, \tag{5.4.10}$$

for all $v \in \mathcal{V}_1$.

This problem is encumbered with the fact that the test space and the solution space are not the same. In other words, the Lax–Milgram lemma does not apply. In this case, to show that Problem (**P**) is well-posed, we must show that the conditions of the Banach-Nečas-Babuška theorem are satisfied. Furthermore, the jump across the interfaces is an imposed condition on the solution space. How to enforce such a condition in an effective finite element method to solve the problem is not obvious. Each of these two difficulties will be handled separately. Yet, we overcome both of these difficulties by considering alternative variational formulations.

To establish the well-posedness of Problem (**P**), we start by considering a new variational problem, which we call (**P′**).

(P′) Find $w \in \mathcal{V}_\kappa$ such that

$$\int_{\Omega_0} d_0 \nabla w_0 \nabla v_0 + (\boldsymbol{c}\cdot\nabla v_0 + \frac{v_0}{\tau}) w_0 \, \mathrm{d}\boldsymbol{x} + \kappa \int_{\Omega_1} d_1 \nabla w_1 \nabla v_1 + (\boldsymbol{c}\cdot\nabla v_1 + \frac{v_1}{\tau}) w_1 \, \mathrm{d}\boldsymbol{x} = \int_{\Omega_0} g_0 v_0 \, \mathrm{d}\boldsymbol{x} + \int_{\Omega_1} \kappa g_1 v_1 \, \mathrm{d}\boldsymbol{x}, \quad (5.4.11)$$

for all $v \in \mathcal{V}_\kappa$.

For Problem (**P′**) the test functions and the solution belong to the same space. Thus, for well-posedness, we need only show that the conditions of the Lax–Milgram Lemma are satisfied. We do this in the following section. Moreover, solving Problem (**P′**) is equivalent to solving Problem (**P**).

5.4.2 Existence and Uniqueness for Problem (P′).

We apply the Lax–Milgram Lemma to prove that Problem (**P′**) is well-posed. We define the bilinear form $\tilde{a}_0(\cdot,\cdot) \in \mathcal{L}(\mathcal{V}_\kappa \times \mathcal{V}_\kappa; \mathbb{R})$ as

$$\tilde{a}_0(w,v) = \int_{\Omega_0} d_0 \nabla w_0 \nabla v_0 + \frac{1}{\tau} v_0 w_0 \, \mathrm{d}\boldsymbol{x} + \int_{\Omega_1} \kappa \left[d_1 \nabla w_1 \nabla v_1 + \frac{1}{\tau} v_1 w_1 \right] \, \mathrm{d}\boldsymbol{x}.$$

and the linear form $\tilde{L} \in \mathcal{V}_\kappa'$, the dual of $\mathcal{V}_\kappa$, as

$$\tilde{L}(v) = \int_{\Omega_0} g_0 v_0 \, \mathrm{d}\boldsymbol{x} + \int_{\Omega_1} \kappa g_1 v_1 \, \mathrm{d}\boldsymbol{x}.$$

Then, when $c = 0$, we can write Equation (5.4.11) of Problem (**P′**) as

$$\tilde{a}_0(u,v) = \tilde{L}(v). \quad (5.4.12)$$

Let ($\mathbf{P}_0'$) denote the variational Problem obtained by setting $c = 0$ in Problem (**P′**).

Theorem 5.4.1. *Problem ($\boldsymbol{P}_0'$) is well posed. Moreover, $w \in \mathcal{V}_\kappa$ is the unique solution of Problem ($\boldsymbol{P}_0'$) if and only if $w \in \mathcal{V}_\kappa$ is the unique solution of System (5.4.5) - (5.4.8), when $c = 0$.*

Proof: First, note that $\mathcal{V}_\kappa$ is a Hilbert space. Indeed, the following mapping is linear and continuous:

$$v \in X \mapsto (v_0, v_1) \in H^1(\Omega_0) \times H^1_{0,\partial\Omega}(\Omega_1), \tag{5.4.13}$$
$$\mapsto (v_0|_\Gamma, v_1|_\Gamma) \in H^{1/2}(\Gamma) \times H^{1/2}(\Gamma), \tag{5.4.14}$$
$$\mapsto v_0 - \kappa v_1 = v \in H^{1/2}(\Gamma). \tag{5.4.15}$$

Let us denote this jump operator by $[v]_\kappa = v_0 - \kappa v_1$. We have that $\mathcal{V}_\kappa = ([v]_\kappa)^{-1}(\{0\})$; i.e., $\mathcal{V}_\kappa$ is the preimage of $\{0\}$. Since the set $\{0\}$ is closed in every vector space, we can apply the topological result that the preimage of a closed set under a continuous function is closed. Thus, $\mathcal{V}_\kappa$ is a closed subspace of X. Since X is a Hilbert space, then so is $\mathcal{V}_\kappa$.

The bilinear form $\tilde{a}_0(u, v)$ is coercive. Indeed,

$$\begin{aligned}
\tilde{a}_0(w, w) &= \int_{\Omega_0} d_0 |\nabla w_0|^2 + \frac{w_0^2}{\tau} \, \mathrm{d}\boldsymbol{x} + \kappa \int_{\Omega_1} d_1 |\nabla w_1|^2 + \frac{w_1^2}{\tau} \, \mathrm{d}\boldsymbol{x}, \\
&\geq \underline{\sigma} \left(\int_{\Omega_0} |\nabla w_0|^2 + |w_0|^2 \, \mathrm{d}\boldsymbol{x} + \int_{\Omega_1} |\nabla w_1|^2 + |w_1|^2 \, \mathrm{d}\boldsymbol{x} \right), \\
&= \underline{\sigma} \left\| w \right\|_X ,
\end{aligned}$$

where $\underline{\sigma} = \min(d_0, \frac{1}{\tau}, \kappa d_1, \frac{\kappa}{\tau})$. Additionally, the following calculations show that $\tilde{a}_0(u, v)$ is bounded.

$$\begin{aligned}
|\tilde{a}_0(w, v)| &= \left| \int_{\Omega_0} d_0 \nabla w_0 \nabla v_0 + \frac{v_0}{\tau} w_0 \, \mathrm{d}\boldsymbol{x} + \int_{\Omega_1} \kappa \left(d_1 \nabla w_1 \nabla v_1 + \frac{v_1}{\tau} w_1 \right) \, \mathrm{d}\boldsymbol{x} \right|, \\
&\leq \overline{\sigma} \left| \int_{\Omega_0} \nabla w_0 \nabla v_0 + w_0 v_0 \, \mathrm{d}\boldsymbol{x} \right| + \left| \int_{\Omega_1} \nabla w_1 \nabla v_1 + w_0 v_0 \, \mathrm{d}\boldsymbol{x} \right|, \\
&\leq \overline{\sigma} \left(\left\| w_0 \right\|_{H^1(\Omega_0)} \left\| v_0 \right\|_{H^1(\Omega_0)} + \left\| w_1 \right\|_{H^1(\Omega_1)} \left\| v_1 \right\|_{H^1(\Omega_0)} \right), \\
&\leq \overline{\sigma} \left(\left\| w_0 \right\|^2_{H^1(\Omega_0)} + \left\| w_1 \right\|^2_{H^1(\Omega_1)} \right)^{1/2} \left(\left\| v_0 \right\|^2_{H^1(\Omega_0)} + \left\| v_1 \right\|^2_{H^1(\Omega_0)} \right)^{1/2}, \\
&= \overline{\sigma} \left\| w \right\|^2_X \left\| v \right\|^2_X .
\end{aligned}$$

Here, $\overline{\sigma} = \max(d_0, \frac{1}{\tau}, \kappa d_1, \frac{\kappa}{\tau})$. The second line is due to the triangle inequality. The third and fourth lines result from the Cauchy-Schwarz inequality.

Thus, from the Lax–Milgram Lemma, we have that there exists a unique $w \in \mathcal{V}_\kappa$ such that

$$\tilde{a}_0(w, v) = \tilde{L}(v), \quad \forall v \in \mathcal{V}_\kappa,$$

and

$$\|w\|_X \leq C \|g\|_{0,\Omega}, \quad C > 0 \text{ is a constant.}$$

Now, suppose that $w \in \mathcal{V}_\kappa$ is the unique solution to Problem $(\mathbf{P}_0')$. Then, for any $v \in \mathcal{D}(\Omega_0)$ Equation (5.4.12) is satisfied. Applying Green's formula, we find that

$$\left\langle -d_0 \Delta w_0 + \frac{1}{\tau} w_0, v_0 \right\rangle = \int_{\Omega_0} g_0 v_0 \, \mathrm{d}\boldsymbol{x}, \qquad \forall v \in \mathcal{D}(\Omega_0)$$

Similarly, we see that

$$\left\langle \kappa \left(-d_1 \Delta w_1 + \frac{1}{\tau} w_1 \right), v_1 \right\rangle = \int_{\Omega_1} \kappa g_1 v_1 \, \mathrm{d}\boldsymbol{x}, \qquad \forall v \in \mathcal{D}(\Omega_1).$$

Thus we see that w satisfies Equation (5.4.5) in the sense of distributions when $c = 0$. We set $\mathfrak{D} = \cup_{i=0}^{1} \mathcal{D}(\bar{\Omega}_i)$. Then taking any $v \in \mathcal{V}_\kappa \cap \mathfrak{D}$, and applying Green's formula, we find that

$$\left\langle -d_0 \Delta w_0 + \frac{1}{\tau} w_0 - g_0, v_0 \right\rangle + \left\langle \kappa \left(-d_1 \Delta w_1 + \frac{1}{\tau} w_1 - g_1 \right), v_1 \right\rangle + \int_\Gamma d_0 \partial_{\boldsymbol{\nu}} w_0 v_0 - \kappa d_1 \partial_{\boldsymbol{\nu}} w_1 v_1 \, \mathrm{d}s = 0, \qquad \forall v \in \mathcal{V}_\kappa$$

Here the integral $\int_\Gamma$ represents the duality product between $H^{-1/2}(\Gamma)$ and $H^{1/2}(\Gamma)$. Since Equations (5.4.5) are satsified in the sense of distribution, we conclude that the boundary term must be equal to zero. Since for $v \in \mathcal{V}_\kappa$, we have that $v_0 = \kappa v_1$ this boundary equation becomes

$$\int_\Gamma \kappa v_1 \left(d_0 \partial_{\boldsymbol{\nu}} w_0 - d_1 \partial_{\boldsymbol{\nu}} w_1 \right) \, \mathrm{d}s = 0, \qquad \forall v \in \mathcal{V}_\kappa.$$

Hence, we recover the flux condition (5.4.7), given that $c = 0$.

Next, suppose that w satisfies System (5.4.5) -(5.4.8) in the sense of distribution. We multiply the equation inside Ω_1 corresponding to Equation (5.4.5) by κ. We multiply the resulting coupled equations by $v \in \mathcal{V}_\kappa \cap \mathfrak{D}$, integrate and then find the relation

$$\left\langle -d_0 \Delta w_0 - (\boldsymbol{c} \cdot \nabla) w_0 + \frac{w_0}{\tau}, v_0 \right\rangle + \left\langle \kappa \left(-d_1 \Delta w_1 - (\boldsymbol{c} \cdot \nabla) w_1 + \frac{w_1}{\tau} \right), v_1 \right\rangle = \int_{\Omega_0} g_0 v_0 \, \mathrm{d}\boldsymbol{x} + \int_{\Omega_1} \kappa g_1 v_1 \, \mathrm{d}\boldsymbol{x}.$$

Focusing on the left-hand side, we find that

$$\text{LHS} = \left\langle -d_0 \Delta w_0 - (\boldsymbol{c} \cdot \nabla) w_0 + \frac{w_0}{\tau}, v_0 \right\rangle + \left\langle \kappa \left(-d_1 \Delta w_1 - (\boldsymbol{c} \cdot \nabla) w_1 + \frac{w_1}{\tau} \right), v_1 \right\rangle,$$

$$
\begin{aligned}
&= \int_{\Omega_0} d_0 \nabla w_0 \nabla v_0 + (\boldsymbol{c}\cdot\nabla v_0 + \frac{v_0}{\tau}) w_0 \,\mathrm{d}\boldsymbol{x} + \kappa \int_{\Omega_1} d_1 \nabla w_1 \nabla v_1 + (\boldsymbol{c}\cdot\nabla v_1 + \frac{v_1}{\tau}) w_1 \,\mathrm{d}\boldsymbol{x}, \\
&\quad + \int_\Gamma \kappa \left(d_1 \partial_{\boldsymbol{\nu}} w_1 + (\boldsymbol{c}\cdot\boldsymbol{\nu}) w_1\right) v_1 \,\mathrm{d}s - \int_\Gamma \left(d_0 \partial_{\boldsymbol{\nu}} w_0 + (\boldsymbol{c}\cdot\boldsymbol{\nu}) w_0\right) v_0 \,\mathrm{d}s, \\
&= \int_{\Omega_0} d_0 \nabla w_0 \nabla v_0 + (\boldsymbol{c}\cdot\nabla v_0 + \frac{v_0}{\tau}) w_0 \,\mathrm{d}\boldsymbol{x} + \kappa \int_{\Omega_1} d_1 \nabla w_1 \nabla v_1 + (\boldsymbol{c}\cdot\nabla v_1 + \frac{v_1}{\tau}) w_1 \,\mathrm{d}\boldsymbol{x}, \\
&\quad + \int_\Gamma \left(d_1 \partial_{\boldsymbol{\nu}} w_1 + (\boldsymbol{c}\cdot\boldsymbol{\nu}) w_1 - d_0 \partial_{\boldsymbol{\nu}} w_0 - (\boldsymbol{c}\cdot\boldsymbol{\nu}) w_0\right) \kappa v_1 \,\mathrm{d}s, \\
&= \int_{\Omega_0} d_0 \nabla w_0 \nabla v_0 + (\boldsymbol{c}\cdot\nabla v_0 + \frac{v_0}{\tau}) w_0 \,\mathrm{d}\boldsymbol{x} + \kappa \int_{\Omega_1} d_1 \nabla w_1 \nabla v_1 + (\boldsymbol{c}\cdot\nabla v_1 + \frac{v_1}{\tau}) w_1 \,\mathrm{d}\boldsymbol{x}.
\end{aligned}
$$

In the second line, we applied Green's formula and integration-by-parts. In the third line, we applied the fact that $v_0 = \kappa v_1$ on Γ for $v \in \mathcal{V}_\kappa$. And in the last line we used the fact that w satisfies Equation (5.4.7). When $c = 0$, we have obtained the variational formulation Problem $(\mathbf{P}_0')$. Therefore, w also satisfies Problem $(\mathbf{P}_0')$. ∎

We now consider the case when $c \neq 0$. We prove the existence in this case under the assumption that $d_0 = d_1 = d$. First, following Chapter 2 of [10] and considering System (5.4.5) - (5.4.8), we make the change of variable $w_i = e^{-\frac{\boldsymbol{c}}{d}\cdot\boldsymbol{x}} u_i$. Then we have that

$$\nabla w_i = -\frac{\boldsymbol{c}}{d} e^{-\frac{\boldsymbol{c}}{d}\cdot\boldsymbol{x}} u_i + e^{-\frac{\boldsymbol{c}}{d}\cdot\boldsymbol{x}} \nabla u_i,$$

and

$$\Delta w_i = \nabla\cdot\nabla w_i = \left|\frac{\boldsymbol{c}}{d}\right|^2 e^{-\frac{\boldsymbol{c}}{d}\cdot\boldsymbol{x}} u_i - 2 e^{-\frac{\boldsymbol{c}}{d}\cdot\boldsymbol{x}} \frac{\boldsymbol{c}}{d}\cdot\nabla u_i + e^{-\frac{\boldsymbol{c}}{d}\cdot\boldsymbol{x}} \Delta u_i.$$

Hence, Equation (5.4.5) becomes

$$-d e^{-\frac{\boldsymbol{c}}{d}\cdot\boldsymbol{x}} \Delta u_i + \boldsymbol{c}\cdot e^{-\frac{\boldsymbol{c}}{d}\cdot\boldsymbol{x}} \nabla u_i + \frac{e^{-\frac{\boldsymbol{c}}{d}\cdot\boldsymbol{x}}}{\tau} u_i = \tilde{g}_i, \tag{5.4.16}$$

where, $\tilde{g}_i = G(e^{-\frac{\boldsymbol{c}}{d}\cdot\boldsymbol{x}}\tilde{u}_i) + \frac{e^{-\frac{\boldsymbol{c}}{d}\cdot\boldsymbol{x}}}{\tau}\tilde{u}_i$. We remind the reader that formally, we have that $w_i^n = e^{-\frac{\boldsymbol{c}}{d}\cdot\boldsymbol{x}}\tilde{u}_i$, and $w_i^{n+1} = e^{-\frac{\boldsymbol{c}}{d}\cdot\boldsymbol{x}} u_i$. We note that

$$\nabla\cdot\left(-d e^{-\frac{\boldsymbol{c}}{d}\cdot\boldsymbol{x}} \nabla u_i\right) = -d e^{-\frac{\boldsymbol{c}}{d}\cdot\boldsymbol{x}} \Delta u_i + \boldsymbol{c}\cdot e^{-\frac{\boldsymbol{c}}{d}\cdot\boldsymbol{x}} \nabla u_i.$$

Thus, we can write Equation (5.4.16) as

$$\nabla\cdot\left(-d e^{-\frac{\boldsymbol{c}}{d}\cdot\boldsymbol{x}} \nabla u_i\right) + \frac{e^{-\frac{\boldsymbol{c}}{d}\cdot\boldsymbol{x}}}{\tau} u_i = \tilde{g}_i. \tag{5.4.17}$$

The jump interface conditions (5.4.6) become

$$e^{-\frac{\boldsymbol{c}}{d}\cdot\boldsymbol{x}} u_0 = \kappa e^{-\frac{\boldsymbol{c}}{d}\cdot\boldsymbol{x}} u_1 \implies u_0 = \kappa u_1. \tag{5.4.18}$$

The flux interface conditions (5.4.7) become

$$de^{-\frac{\mathbf{c}}{d}\cdot\boldsymbol{x}}\partial_{\boldsymbol{\nu}}u_0 = de^{-\frac{\mathbf{c}}{d}\cdot\boldsymbol{x}}\partial_{\boldsymbol{\nu}}u_1 \implies \partial_{\boldsymbol{\nu}}u_0 = \partial_{\boldsymbol{\nu}}u_1. \tag{5.4.19}$$

Theorem 5.4.2. *When $c \neq 0$ and $d_1 = d_0 = d$, then Problem ($\boldsymbol{P'}$) is well-posed. Moreover, $w \in \mathcal{V}_\kappa$ is the unique solution of Problem ($\boldsymbol{P'}$) if and only if $w \in \mathcal{V}_\kappa$ is the unique solution of System (5.4.5) - (5.4.8),*

Proof: To prove this statement, we look at the following variational problem: Find $u \in \mathcal{V}_\kappa$ such that

$$\tilde{a}_d(u,v) = \tilde{L}_d(v), \qquad \forall v \in \mathcal{V}_\kappa.$$

where

$$\tilde{a}_d(u,v) = \int_{\Omega_0} de^{-\frac{\mathbf{c}}{d}\cdot\boldsymbol{x}}\nabla u_0\nabla v_0 + \frac{e^{-\frac{\mathbf{c}}{d}\cdot\boldsymbol{x}}}{\tau}u_0v_0\,\mathrm{d}\boldsymbol{x} + \int_{\Omega_1}\kappa\left(de^{-\frac{\mathbf{c}}{d}\cdot\boldsymbol{x}}\nabla u_1\nabla v_1 + \frac{e^{-\frac{\mathbf{c}}{d}\cdot\boldsymbol{x}}}{\tau}u_1v_1\right)\,\mathrm{d}\boldsymbol{x},$$

and

$$\tilde{L}_d(v) = \int_{\Omega_0}\tilde{g}_0v_0\,\mathrm{d}\boldsymbol{x} + \int_{\Omega_1}\kappa\tilde{g}_1v_1\,\mathrm{d}\boldsymbol{x}.$$

Since $e^{-\frac{\mathbf{c}}{d}\cdot\boldsymbol{x}}$ is bounded and positive on Ω_i, $i = 1, 2$ we have that this bilinear form is coercive and bounded. Thus, by the Lax–Milgram lemma, this variational problem is well-posed. Then, by following similar steps as in the proof of Theorem 5.4.1, we find that solutions to this variational problem are solutions to System (5.4.5) - (5.4.8) and vice-versa. Thus, there is a unique solution to System (5.4.5) - (5.4.8), when $c \neq 0$ and $d_1 = d_0$.

Finally to conclude that Problem ($\mathbf{P}'$) is well-posed when $\boldsymbol{c} \not\equiv 0$ and $d_i = d$, $i = 1, 2.$, we follow similar steps as before to show that solutions to System (5.4.5) - (5.4.8) are solutions to Problem ($\mathbf{P}'$) and vice-versa. Thus, Problem ($\mathbf{P}'$) has a unique solution and

$$\|w\|_X \leq C\,\|g\|_{0,\Omega}\,, \quad C > 0 \text{ is a constant.}$$

∎

The above two theorems prove that Problem ($\mathbf{P}'$) is well-posed in the two cases: 1) $c = 0$; 2) $c \neq 0$ and $d_1 = d_0$. As noted in [53], no proof is available for the general case $c \neq 0$ and $d_1 \neq d_0$. The two particular cases studied above indicate that existence and uniqueness should hold but a proof is still missing in the general case. For the rest of this chapter, we will assume that Problem ($\mathbf{P}'$) is well-posed in the general case.

5.4.3 Existence and Uniqueness for Problem (P)

Finally, we show that Problem ($\mathbf{P}$) is well-posed. Problem ($\mathbf{P}$) can be written in the following form: Find $w \in \mathcal{V}_\kappa$ such that

$$a(w,v) = L(v), \qquad \forall v \in \mathcal{V}_1,$$

where $a(\cdot,\cdot) \in \mathcal{L}(\mathcal{V}_\kappa \times \mathcal{V}_1; \mathbb{R})$ is the mapping

$$a(w,v) = \sum_{i=0}^{1} \int_{\Omega_i} d_i \nabla w_i \nabla v_i + (\boldsymbol{c} \cdot \nabla v_i + \frac{v_i}{\tau}) w_i \, \mathrm{d}\boldsymbol{x},$$

and $L(\cdot) \in \mathcal{L}(\mathcal{V}_1; \mathbb{R})$ is the mapping

$$L(v) = \sum_{i=0}^{1} \int_{\Omega_i} g_i v \, \mathrm{d}\boldsymbol{x}.$$

Theorem 5.4.3. *w is a solution of Problem ($\boldsymbol{P}$) if and only if w is a solution of Problem ($\boldsymbol{P}'$). Hence, Problem ($\boldsymbol{P}$) has a unique solution.*

Proof: We have that

$$\begin{aligned} w \text{ is a solution of Problem } (\mathbf{P}) &\iff w \text{ is a solution of System (5.4.5) - (5.4.8).} \\ &\iff w \text{ is a solution of Problem } (\mathbf{P}') \end{aligned}$$

Since Problem ($\mathbf{P}'$) has a unique solution, we conclude that Problem ($\mathbf{P}$) has a unique solution. ∎

We now have existence and uniqueness for Problem ($\mathbf{P}$). Thus, by the Banach-Nečas-Babuška Theorem the following conditions are satisfied:

$$\exists \sigma > 0, \qquad \inf_{w \in \mathcal{V}_\kappa} \sup_{v \in \mathcal{V}_1} \frac{a(w,v)}{\|w\|_X \|v\|_X} \geq \sigma, \tag{5.4.20}$$

$$\forall v \in \mathcal{V}_1, \quad (\forall w \in \mathcal{V}_\kappa, a(w,v) = 0) \implies (v = 0). \tag{5.4.21}$$

Moreover, we have the following a priori estimate:

$$\forall g \in \mathcal{V}_1', \quad \|w\|_{\mathcal{V}_\kappa} \leq \frac{1}{\sigma} \|f\|_{\mathcal{V}_1'}. \tag{5.4.22}$$

In the next section, we will circumvent the difficulty of implementing the jump conditions on Γ with another variational formulation, called a hybrid formulation.

5.4.4 Hybrid Variational Formulation

In the previous section we developed two variational formulations where the jump condition along the interface Γ is explicitly imposed in the functional space $\mathcal{V}_\kappa$. With a hybrid formulation, which we develop in this section, we do not need to impose the discontinuity in a strong way in the functional space. Instead, the jump on

the interface is weakly imposed through a Lagrange multiplier, which belongs to the following space:

$$M = \{\mu \in H^{-1/2}(\Gamma) : \exists \boldsymbol{q} \in H(\mathrm{div};\Omega) \text{ such that } \boldsymbol{q}\cdot\boldsymbol{\nu} = \mu \text{ on } \Gamma\}.$$

With this functional framework we define the hybrid formulation, which we call Problem (**Q**):

(Q) Find $(w,\lambda) \in X \times M$ such that

$$a(w,v) + b_1(v,\lambda) = \langle g, v\rangle_{X',X}, \qquad \forall v \in X, \tag{5.4.23}$$

$$b_\kappa(w,\mu) = 0, \qquad \forall \mu \in M, \tag{5.4.24}$$

where

$$a(w,v) = \sum_{i=0}^{1} \int_{\Omega_i} d_i \nabla w_i \nabla v_i + \left((\boldsymbol{c}\cdot\nabla v_i) + \frac{1}{\tau_n} v_i\right) w_i \, \mathrm{d}\boldsymbol{x}, \tag{5.4.25}$$

$$b_1(w,\lambda) = \int_\Gamma \lambda(w_0 - w_1)\mathrm{d}S, \tag{5.4.26}$$

$$b_\kappa(w,\lambda) = \int_\Gamma \lambda(w_0 - \kappa w_1)\mathrm{d}S. \tag{5.4.27}$$

Here the integral $\int_\Gamma$ represents the duality product between $H^{-1/2}(\Gamma)$ and $H^{1/2}(\Gamma)$; i.e., $\int_\Gamma \lambda(w_0 - \kappa w_1)\mathrm{d}S = \langle \lambda, w_0 - \kappa w_1\rangle_{H^{-1/2},H^{1/2}}$, and w_i denotes $w_i|_\Gamma = \gamma(w_i)$ where $\gamma : H^1(\Omega_i) \to H^{1/2}(\Gamma)$ is the trace operator.

In the next section we prove existence and uniqueness of the solution for this problem.

5.4.5 Existence and Uniqueness of Solutions for the Hybrid Variational Form

Following Raviart and Thomas [50], we will characterise $\mathcal{V}_1$ and $\mathcal{V}_\kappa$ through the bilinear functionals b_1 and b_κ, respectively.

Lemma 5.4.4. *A continuous linear functional L on the space X vanishes on $\mathcal{V}_1$ if and only if there exists a unique element $\mu \in M$ such that*

$$\forall v \in X,\ L(v) = \int_\Gamma \mu(v_0 - v_1)\ \mathrm{d}s.$$

Lemma 5.4.5. *A continuous linear functional L on the space X vanishes on $\mathcal{V}_\kappa$ if and only if there exists a unique element $\mu \in M$ such that*

$$\forall v \in X,\ L(v) = \int_\Gamma \mu(v_0 - \kappa v_1)\ \mathrm{d}s.$$

The proof of Lemma 5.4.4 is identical to the proof of Lemma 1 in [50]. We present the proof of Lemma 5.4.5, which is a modification of this proof.

Proof: (**Lemma 5.4.5**)
By the Riesz Representation Theorem and the Hahn-Banach Theorem, there exist $q_j \in L^2(\Omega_i)$, $j = 0, 1, 2$, such that any continuous linear function on $H^1(\Omega_i)$ can be written in the following way

$$v \mapsto \int_{\Omega_i} \kappa_i \left(q_1 \frac{\partial v}{\partial x} + q_2 \frac{\partial v}{\partial y} + q_0 v \right) \, \mathrm{d}\boldsymbol{x}, \quad q_j \in L^2(\Omega_i), \quad j = 0, 1, 2,$$

where

$$\kappa_i = \begin{cases} 1, & \boldsymbol{x} \in \Omega_0, \\ \kappa, & \boldsymbol{x} \in \Omega_1. \end{cases}$$

Hence, given a continuous linear functional L on X, there exist $q_j \in L^2(\Omega)$, $j = 0, 1, 2$ such that

$$\forall v \in X, \; L(v) = \sum_{i=0}^{1} \int_{\Omega_i} \kappa_i \left(q_1 \frac{\partial v}{\partial x} + q_2 \frac{\partial v}{\partial y} + q_0 v \right) \, \mathrm{d}\boldsymbol{x}, \quad q_j \in L^2(\Omega), \quad j = 0, 1, 2.$$

Assume that $L(v)$ vanishes on $\mathcal{V}_\kappa$; i.e.,

$$\forall v \in \mathcal{V}_\kappa, \; L(v) = \sum_{i=0}^{1} \int_{\Omega_i} \kappa_i \left(q_1 \frac{\partial v}{\partial x} + q_2 \frac{\partial v}{\partial y} + q_0 v \right) \, \mathrm{d}\boldsymbol{x} = 0. \tag{5.4.28}$$

Then, for all $v \in \mathcal{D}(\Omega_i)$ we have that

$$\int_{\Omega_i} \kappa_i \left(q_1 \frac{\partial v}{\partial x} + q_2 \frac{\partial v}{\partial y} \right) \, \mathrm{d}\boldsymbol{x} = - \int_{\Omega_i} \kappa_i q_0 v \, \mathrm{d}\boldsymbol{x}. \tag{5.4.29}$$

Using the definition of derivatives in the sense of distributions,, we obtain

$$\left\langle -\kappa_i \left(\frac{\partial q_1}{\partial x} + \frac{\partial q_2}{\partial y} \right), v \right\rangle = - \int_{\Omega_i} \kappa_i q_0 v \, \mathrm{d}\boldsymbol{x}. \tag{5.4.30}$$

$$\iff \langle \kappa_i \left(\nabla \cdot \boldsymbol{q} \right), v \rangle = \int_{\Omega_i} \kappa_i q_0 v \, \mathrm{d}\boldsymbol{x}. \tag{5.4.31}$$

Thus, inside each Ω_i, $\mathrm{div}\boldsymbol{q} = q_0 \in L^2(\Omega_i)$ in the sense of distributions, where $\boldsymbol{q} = (q_1, q_2)$. Therefore, $\boldsymbol{q} \in H(\mathrm{div}; \Omega_i)$, and the following Green's formula holds within each Ω_i:

$$\forall v \in H^1(\Omega_i), \quad \int_{\Omega_i} \nabla v_i \cdot \boldsymbol{q} + v_i \, \mathrm{div}\boldsymbol{q} \, \mathrm{d}\boldsymbol{x} = \int_{\Gamma} v_i \boldsymbol{q} \cdot \boldsymbol{\nu}_i \, \mathrm{d}s.$$

We replace q_0 with $\mathrm{div}\boldsymbol{q}$ in equation (5.4.28). Let $\gamma^*(\boldsymbol{q}|_{\Omega_i}) = \boldsymbol{q}_i \cdot \boldsymbol{\nu_i}$, where $\gamma^* : H(\mathrm{div};\Omega_i) \to H^{-1/2}(\Gamma)$ and $\boldsymbol{\nu_i}$ is the outward pointing normal to the boundary of Ω_i. Then for all $v \in \mathcal{V}_\kappa$, by applying Green's formula within each Ω_i, we find that

$$\sum_{i=0}^{1} \int_{\Omega_i} \kappa_i \left(\nabla v \cdot \boldsymbol{q} + v \ \mathrm{div}\boldsymbol{q}\right) \ \mathrm{d}\boldsymbol{x} = 0. \tag{5.4.32}$$

$$\iff \int_\Gamma \kappa \left(\boldsymbol{q}_1 \cdot \boldsymbol{\nu}_1\right) v_1 \ \mathrm{d}S + \int_\Gamma \left(\boldsymbol{q}_0 \cdot \boldsymbol{\nu}_0\right) v_0 \ \mathrm{d}s = 0. \tag{5.4.33}$$

$$\iff \int_\Gamma \kappa v_1 \left(\boldsymbol{q}_1 \cdot \boldsymbol{\nu}_1 + \boldsymbol{q}_0 \cdot \boldsymbol{\nu}_0\right) \ \mathrm{d}s = 0. \tag{5.4.34}$$

The last equivalence follows since on Γ, $v_0 = \kappa v_1$. Since this relationship is true for all $v_1 \in H^{1/2}(\Gamma)$, we have that in $H^{-1/2}(\Gamma)$

$$\boldsymbol{q}_1 \cdot \boldsymbol{\nu}_1 + \boldsymbol{q}_0 \cdot \boldsymbol{\nu}_0 = 0. \tag{5.4.35}$$

$$\iff \boldsymbol{q}_0 \cdot \boldsymbol{\nu}_0 = -\boldsymbol{q}_1 \cdot \boldsymbol{\nu}_1. \tag{5.4.36}$$

$$\iff \boldsymbol{q}_0 \cdot \boldsymbol{\nu} = \boldsymbol{q}_1 \cdot \boldsymbol{\nu}, \tag{5.4.37}$$

where in the last equivalence we use the fact that $\nu := \nu_0 = -\nu_1$. Thus, $\boldsymbol{q}$ belongs to $H(\mathrm{div};\Omega)$. Indeed, take $\phi \in \mathcal{D}(\Omega)$. Then the following holds:

$$\begin{aligned}
\int_\Omega \boldsymbol{q}\nabla\phi \ \mathrm{d}\boldsymbol{x} &= \sum_{i=0}^{1} \int_{\Omega_i} \boldsymbol{q}\nabla\phi \ \mathrm{d}\boldsymbol{x}, \\
&= \sum_{i=0}^{1} \left[- \int_{\Omega_i} \phi \mathrm{div}\boldsymbol{q} \ \mathrm{d}\boldsymbol{x} + \int_\Gamma \phi \boldsymbol{q} \cdot \boldsymbol{\nu}_i \ \mathrm{d}s \right], \\
&= \sum_{i=0}^{1} \left[- \int_{\Omega_i} \phi \mathrm{div}\boldsymbol{q} \ \mathrm{d}\boldsymbol{x} \right] + \int_\Gamma \phi \left(\boldsymbol{q} \cdot \boldsymbol{\nu} - \boldsymbol{q} \cdot \boldsymbol{\nu}\right) \ \mathrm{d}s \\
&= - \sum_{i=0}^{1} \int_{\Omega_i} \phi \mathrm{div}\boldsymbol{q} \ \mathrm{d}\boldsymbol{x}, \\
&= - \int_\Omega \phi \mathrm{div}\boldsymbol{q} \ \mathrm{d}\boldsymbol{x}.
\end{aligned}$$

Therefore, $\mathrm{div}\boldsymbol{q} \in L^2(\Omega)$ and we can write

$$\forall v \in X, \ L(v) = \sum_{i=0}^{1} \int_{\Omega_i} \kappa_i \left(\nabla v \cdot \boldsymbol{q} + v \ \mathrm{div}\boldsymbol{q}\right) \ \mathrm{d}\boldsymbol{x}. \tag{5.4.38}$$

Conversely, any linear functional of the form (5.4.38) is continuous on X and vanishes on $\mathcal{V}_\kappa$.

Using Green's formula on equation (5.4.38) and the definition of $H^{-1/2}(\Omega_i)$ within each Ω_i we obtain for all $v \in X$

$$L(v) = \sum_{i=0}^{1} \int_\Gamma \kappa_i v_i \boldsymbol{q} \cdot \boldsymbol{\nu}_i \, \mathrm{d}s = \int_\Gamma \boldsymbol{q} \cdot \boldsymbol{\nu} \left(v_0 - \kappa v_1\right) \, \mathrm{d}s = \int_\Gamma \mu \left(v_0 - \kappa v_1\right) \, \mathrm{d}s, \quad \mu \in M.$$

The function $\boldsymbol{q}$ is not uniquely determined, but the corresponding element $\mu \in M$ is unique. Indeed, assume that

$$\forall v \in X, \ \int_\Gamma \mu \left(v_0 - \kappa v_1\right) \, \mathrm{d}s = 0.$$

Then, by taking $v_1 \equiv 0$ on Ω_1 and $v_0 \in H^1(\Omega_0)$ such that $v_0 \not\equiv 0$ in $H^{1/2}(\Gamma)$, we find that

$$\int_\Gamma \mu v_0 \, \mathrm{d}s = 0.$$

Thus, we have that

$$\forall v \in H^1(\Omega_0), \quad \int_\Gamma \mu v \, \mathrm{d}s = 0,$$

which implies that $\mu = 0$ on Γ by the surjectivity of the trace operator $v \mapsto v|_\Gamma$ from $H^1(\Omega_0)$ onto $H^{1/2}(\Gamma)$. ∎

As a consequence of Lemma 5.4.4 and Lemma 5.4.5, we can characterise $\mathcal{V}_1$ and $\mathcal{V}_\kappa$ as subspaces of X, in the following ways:

$$\mathcal{V}_1 = \{v \in X \ : \ \forall \mu \in M, \ b_1(w, \mu) = 0\}, \tag{5.4.39}$$

and

$$\mathcal{V}_\kappa = \{v \in X \ : \ \forall \mu \in M, \ b_\kappa(w, \mu) = 0\}. \tag{5.4.40}$$

Theorem 5.4.6. *System (5.4.23) - (5.4.24) has a unique solution $(w, \lambda) \in X \times M$. Moreover, $w \in \mathcal{V}_\kappa$ is the solution of system (5.4.5) - (5.4.8) and we have that*

$$\lambda = -\left(d_i \partial_{\boldsymbol{\nu}} w_i + (\boldsymbol{c} \cdot \boldsymbol{\nu}) w_i\right) \quad \textit{on} \ \ \Gamma \ \ \textit{for} \ \ i = 0, 1.$$

Proof: Let $(w, \lambda) \in X \times M$ be a solution to System (5.4.23) - (5.4.24). Then from the characterisation of $\mathcal{V}_\kappa$, Equation (5.4.40), we see that $w \in \mathcal{V}_\kappa$. Choosing $v \in \mathcal{V}_1$, from the characterisation of $\mathcal{V}_1$, Equation (5.4.39), we obtain

$$a(w, v) = \int_\Omega g v \, \mathrm{d}\boldsymbol{x}, \ \forall v \in \mathcal{V}_1.$$

This equation is nothing but Problem (**P**). Thus, existence and uniqueness of $w \in \mathcal{V}_\kappa$ follows from the well-posedness of Problem (**P**). Additionally, $w \in \mathcal{V}_\kappa$ is then a solution of System (5.4.5) - (5.4.8).

Now, suppose that $w \in \mathcal{V}_\kappa$ is a solution of System (5.4.5) - (5.4.8). Consider the linear continuous function on X

$$L(v) = \int_\Omega gv dx - a(w, v).$$

The right-hand side is Problem (**P**). Hence, for $v \in \mathcal{V}_1$, $L(v)$ vanishes. Thus, by Lemma 5.4.4, there exists a unique $\lambda \in M$ such that

$$\forall v \in X,\ b_1(v, \lambda) = \int_\Omega gv \ \mathrm{d}\boldsymbol{x} - a(w, v). \tag{5.4.41}$$

Additionally, since $w \in \mathcal{V}_\kappa$, we have that $b_\kappa(w, \lambda) = 0$. Thus, (w, λ) is the solution to the hybrid formulation.

Finally, since $g_i = \frac{w_i}{\tau} - d_i \Delta w_i - (\boldsymbol{c} \cdot \nabla) w_i$ within each Ω_i, by applying Green's formula in each Ω_i with $\nabla w = q$, we find that, $\forall v \in X$

$$\begin{aligned} b_1(v, \lambda) &= \sum_{i=0}^{1} \int_{\Omega_i} \left(-d_i \Delta w_i - (\boldsymbol{c} \cdot \nabla) w_i + \frac{1}{\tau} w_i \right) v_i \ \mathrm{d}\boldsymbol{x} - a(u, v) \\ &= -\int_\Gamma \left(d_1 \partial_{\boldsymbol{\nu}_1} w_1 + (\boldsymbol{c} \cdot \boldsymbol{\nu}_1) w_1 \right) v_1 \ \mathrm{d}s - \int_\Gamma \left(d_0 \partial_{\boldsymbol{\nu}_0} w_0 + (\boldsymbol{c} \cdot \boldsymbol{\nu}_0) w_0 \right) v_0 \ \mathrm{d}s, \\ &= \int_\Gamma \left(d_1 \partial_{\boldsymbol{\nu}} w_1 + (\boldsymbol{c} \cdot \boldsymbol{\nu}) w_1 \right) v_1 - \left(d_0 \partial_{\boldsymbol{\nu}} w_0 + (\boldsymbol{c} \cdot \boldsymbol{\nu}) w_0 \right) v_0 \ \mathrm{d}s, \\ &= \int_\Gamma (v_0 - v_1) \lambda \ \mathrm{d}s. \end{aligned}$$

Thus, we have that on Γ, $\lambda = -\left(d_1 \partial_{\boldsymbol{\nu}} w_1 + (\boldsymbol{c} \cdot \boldsymbol{\nu}) w_1 \right) = -\left(d_0 \partial_{\boldsymbol{\nu}} w_0 + (\boldsymbol{c} \cdot \boldsymbol{\nu}) w_0 \right)$. ∎

In the present section, we introduced a hybrid variational formulation, called Problem (**Q**). The hybrid system has two unknowns, a primal variable, w, and a dual variable, λ. We proved that Problem (**Q**) has a unique solution. Furthermore, we proved that the primal variable is the unique solution for System (5.4.5) - (5.4.8), and that the dual variable is the flux across the interface Γ. In the following section, we construct a finite element method to approximate the solution of Problem (**Q**).

5.5 Finite Element Formulation

The next step is to define the finite element formulation of the hybrid system. In this section, we assume that Γ is a polygon. We denote by $\bar{\Gamma}_j$, $j = 1, ..., J$ the line

segments that form Γ. We denote by $\mathbb{P}_s$ the space of polynomials of degree $\leq s$. Let $\mathcal{T}_h^i$ denote a triangulation of Ω_i, and let K denote any element of $\mathcal{T}_h^i$. We assume the elements are triangular. Here, h denotes the length of the longest edge of all the elements K. Then, we can define the finite dimensional spaces

$$\mathcal{U}_h^i = \mathcal{U}_h(\Omega_i) = \{v_h \in \mathcal{C}(\Omega_i) : v_h|_K \in \mathbb{P}_s(K),\ \forall K \in \mathcal{T}_h^i, v_h|_{\partial\Omega_i \cap \partial\Omega} = 0\}.$$

We consider the subset of X :

$$X_h = \mathcal{U}_h^0 \times \mathcal{U}_h^1.$$

The trace of the triangulation within each Ω_i over Γ creates a triangulation along Γ. We denote these triangulations by t_i, $i = 0, 1$, and we call the elements in t_i, F. The distinction between these two triangulations is important since it is not necessary for the triangulations to match across Γ. Then we define the finite dimensional space

$$M_h = \{\mu_h \in \mathcal{C}(\Gamma) : \forall F \in t_0,\ \mu_h|_F \in \mathbb{P}_s(F)\}.$$

Remark 5.5.1. We choose, in line with our numerical implementation, to define M_h through the triangulation resulting from $\mathcal{T}_h^0$. It is possible to define M_h in other ways, for example, by the triangulation resulting from $\mathcal{T}_h^1$, or by the intersection of the two [2].

With these definitions, we build our finite dimensional approximation of the hybrid formulation, which we call Problem $(\mathbf{Q}_h)$:

$(\mathbf{Q}_h)$ Find $(w_h, \lambda_h) \in X_h \times M_h$ such that

$$a(w_h, v_h) + b_1(v_h, \lambda_h) = \langle g, v_h \rangle, \qquad \forall v_h \in X_h, \tag{5.5.1}$$
$$b_\kappa(w_h, \mu_h) = 0, \qquad \forall \mu_h \in M_h. \tag{5.5.2}$$

We define the following sets:

$$\mathcal{V}_{\kappa h} = \{v_h \in X_h \ :\ b_\kappa(v_h, \mu_h) = 0,\ \forall \mu_h \in M_h\},$$

and

$$\mathcal{V}_{1h} = \{v_h \in X_h \ :\ b_1(v_h, \mu_h) = 0,\ \forall \mu_h \in M_h\}.$$

Then, we define the following two problems:

$(\mathbf{P}_h)$ Find $w_h \in \mathcal{V}_{\kappa h}$ such that

$$a(w_h, v_h) = L(v_h), \qquad \forall v_h \in \mathcal{V}_{1h}. \tag{5.5.3}$$

$(\mathbf{P}'_h)$ Find $w_h \in \mathcal{V}_{\kappa h}$ such that

$$\tilde{a}(w_h, v_h) = \tilde{L}(v_h), \qquad \forall v_h \in \mathcal{V}_{\kappa h}. \tag{5.5.4}$$

Lemma 5.5.2. *$w_h \in \mathcal{V}_{\kappa h}$ is a solution to Problem ($\boldsymbol{P}_h$) if and only if $w_h \in \mathcal{V}_{\kappa h}$ is a solution to Problem ($\boldsymbol{P}'_h$).*

Proof: Suppose that $w_h \in \mathcal{V}_{\kappa h}$ is a solution to Problem ($\mathbf{P}_h$). Let $(v_{0h}, v_{1h}) \in \mathcal{V}_{1h}$. Then, the equation

$$v_h = (v_{0h}, v_{1h}) = (u_{0h}, \kappa u_{1h})$$

defines a one-to-one relation between $\mathcal{V}_{1h}$ and $\mathcal{V}_{\kappa h}$. Upon plugging in u_h into Equation (5.5.3) we see that w_h satisfies Equation (5.5.4) for any v_h defined through this relation.

Arguing in a similar manner in the other direction proves that w_h, a solution of Problem ($\mathbf{P}'_h$), is also a solution of Problem ($\mathbf{P}_h$), thus concluding the proof. ∎

For the numerical analysis of the problem we make the assumption that $c = 0$. We use the 0-subscript notation, as done in Section 5.4.2, to indicate that this assumption holds. In later sections we validate our scheme for cases where $c \neq 0$. An analytical proof of existence and uniqueness for the discretised system in the most general case remains an open question.

Proposition 5.5.3. *For any $j = \kappa, 1$,*

$$\{\mu_h \in M_h \ ; \ \forall v_h \in X_h, \ b_j(v_h, \mu_h) = 0\} = \{0\}.$$

Proof: Consider μ_h in this subspace and choose $v_h \in X_h$ such that $v_{1h}|_\Gamma = 0$ and $v_{0h}|_\Gamma = \mu_h$. Then

$$b_j(v_h, \mu_h) = \int_\Gamma \mu_h^2 \, \mathrm{d}s = 0 \iff \mu_h = 0.$$

∎

Theorem 5.5.4. *1. Problem ($\boldsymbol{P}'_{h0}$) has a unique solution.*

2. Problem ($\boldsymbol{P}_{h0}$) has a unique solution.

3. Problem ($\boldsymbol{Q}_{h0}$) has a unique solution.

Proof: The proof is similar to that of Theorem 2 of [50].

1. We have that $V_{\kappa h} \subset X_h \subset X$. Since $\tilde{a}_0(v_h, v_h)$ is coercive and bounded over X we conclude that $\tilde{a}_0(v_h, v_h)$ is coercive and bounded over $\mathcal{V}_{\kappa h}$. Thus, by the Lax–Milgram lemma, Problem ($\mathbf{P}'_{h0}$) has a unique solution.

2. By Lemma 5.5.2, Problem ($\mathbf{P}_h$) has a unique solution.

3. Problem $(\mathbf{Q}_{h0})$ is equivalent to a $N \times N$ linear system with $N = \dim(X_h) + \dim(M_h)$. Thus, existence of a solution follows from uniqueness, so that we need only to consider the corresponding homogeneous equation. We assume that $g = 0$. Then, necessarily, from Problem $(\mathbf{P}_{h0})$, $w_h = 0$. We have then that λ_h satisfies
$$b_1(v_h, \lambda_h) = 0, \qquad \forall v_h \in X_h.$$
Hence, from Proposition 5.5.3, $\lambda_h = 0$.

With uniqueness and existence proven, we note that in fact, if $(w_h, \lambda_h) \in X_h \times M_h$ is the unique solution of Problem $(\mathbf{Q}_{h0})$, then $w_h \in \mathcal{V}_{\kappa h}$, and w_h is the unique solution of Problem $(\mathbf{P}_{h0})$.

∎

With the existence and uniqueness proven for our hybrid scheme, we now derive a priori estimates on our approximation of w.

5.6 Error Analysis

In this section we focus on getting error estimates on $w - w_h$. Our overarching goal is to approximate well the solution w of System (5.4.5)- (5.4.8). We leave the error analysis of λ for future work.

First, we introduce yet another finite element formulation:

$(\mathbf{Q}'_{h0})$ Find $(w_h, \lambda_h) \in X_h \times M_h$ such that
$$\tilde{a}_0(w_h, v_h) + b_\kappa(v_h, \lambda_h) = \tilde{L}(v_h), \qquad \forall v_h \in X_h, \tag{5.6.1}$$
$$b_\kappa(w_h, \mu_h) = 0, \qquad \forall \mu_h \in M_h. \tag{5.6.2}$$

In the same way that Problem $(\mathbf{Q}_{h0})$ has a unique solution, we can show that Problem $(\mathbf{Q}'_{h0})$ has a unique solution. Additionally, whenever $(w_h, \lambda_h) \in X_h \times M_h$ is the unique solution to Problem $(\mathbf{Q}'_{h0})$, then $w_h \in \mathcal{V}_{\kappa h}$ and w_h is also the unique solution to Problem $(\mathbf{P}'_{h0})$.

We define the following norm:
$$v_h \to \|v_h\|_a = (\tilde{a}_0(v_h, v_h))^{1/2}.$$
And we note that there exists two constants C_* and C^* dependent only on κ, δ_i and τ such that for $v_h \in X_h$
$$C_* \|v_h\|_a \leq \|v_h\|_X \leq C^* \|v_h\|_a .$$
We define by $\|\cdot\|_{a,\Omega_i}$ the norm
$$\|w\|_{a,\Omega_i} = \left(\int_{\Omega_i} d_i |\nabla w_i|^2 \, \mathrm{d}\boldsymbol{x} + \int_{\Omega_i} \frac{1}{\tau} |w_i|^2 \, \mathrm{d}\boldsymbol{x} \right)^{\frac{1}{2}}.$$

Theorem 5.6.1. *The solution $w_h \in \mathcal{V}_{\kappa h}$ of Problem ($\boldsymbol{P}'_{h0}$) satisfies*

$$\|w - w_h\|_a = \left(\left(\inf_{v_h \in \mathcal{V}_{\kappa h}} \|w - v_h\|_a \right)^2 + \left(\inf_{\mu_h \in M_h} \sup_{v_h \in \mathcal{V}_{\kappa h}} \frac{b_\kappa(v_h, \lambda - \mu_h)}{\|v_h\|_a} \right)^2 \right)^{1/2} \tag{5.6.3}$$

Proof: The result is a direct consequence of Theorem 3 of [50]. ∎

In the literature, the first term in Equation (5.6.3) is called the approximation error, the second term is called the consistency error. Before obtaining bounds on $\|w - w_h\|_a$ we introduce some notation. We assume that $\mathcal{T}_h^i$ are regular families of triangulations in the sense that there exists a constant $\sigma_1 > 0$ independent of h such that

$$\max_{K \in \mathcal{T}_h^i} \frac{h_K}{\rho_K} \leq \sigma_1.$$

where

$$\rho_K = \text{ diameter of the inscribed sphere in } K.$$

Additionally, we also assume that there exists a constant σ_2 such that for any two elements F and F' in t_0

$$|F| \geq \sigma_2 |F'|,$$

where $|\cdot|$ denotes the length of the segment.

Theorem 5.6.2. *Let M_h be associated to a regular family of triangulations. Let $\phi = (\phi_0, \phi_1) \in H^{\sigma+\frac{3}{2}}(\Omega) \times H^{\sigma+\frac{3}{2}}(\Omega)$, where $\frac{1}{2} \leq \sigma \leq s+1$ such that $\frac{\partial \phi_0}{\partial \boldsymbol{\nu}} = \lambda \in M$. Then there exists a constant C, independent of h such that*

$$\inf_{\mu_h \in M_h} \sup_{v_h \in \mathcal{V}_{\kappa h}} \frac{b_\kappa(v_h, \lambda - \mu_h)}{\|v_h\|_a} \leq C h^{\frac{1}{2}+\sigma} \left(\|\phi_0\|_{\sigma+\frac{3}{2},\Omega_0} + \|\phi_1\|_{\sigma+\frac{3}{2},\Omega_1} \right). \tag{5.6.4}$$

Proof: We have that

$$\begin{aligned}
b_\kappa(v_h, \lambda - \mu_h) &= \int_\Gamma (\lambda - \mu_h)(v_{0h} - \kappa v_{1h}) \, \mathrm{d}s, \\
&\leq \|\lambda - \mu_h\|_{H^{-1/2}(\Gamma)} \|v_{0h} - \kappa v_{1h}\|_{H^{1/2}(\Gamma)}, \\
&\leq \|\lambda - \mu_h\|_{H^{-1/2}(\Gamma)} \left(\|v_{0h}\|_{H^{1/2}(\Gamma)} + \|\kappa v_{1h}\|_{H^{1/2}(\Gamma)} \right), \\
&\leq C \|\lambda - \mu_h\|_{H^{-1/2}(\Gamma)} \left(\|v_{0h}\|_{1,\Omega_0} + \|\kappa v_{1h}\|_{1,\Omega_1} \right), \\
&\leq C \|\lambda - \mu_h\|_{H^{-1/2}(\Gamma)} \|v_h\|_a .
\end{aligned}$$

Therefore,

$$\frac{b_\kappa(v_h, \lambda - \mu_h)}{\|v_h\|_a} \leq C \|\lambda - \mu_h\|_{H^{-1/2}(\Gamma)} \implies \sup_{v_h \in \mathcal{V}_{\kappa h}} \frac{b_\kappa(v_h, \lambda - \mu_h)}{\|v_h\|_a} \leq C \|\lambda - \mu_h\|_{H^{-1/2}(\Gamma)} \tag{5.6.5}$$

We can interpret μ_h as the orthogonal projection of $\lambda = \frac{\partial \phi}{\partial \boldsymbol{\nu}}$ from $L^2(\Gamma)$ onto M_h. Thus, from Lemma 2.4 of [7] we have that

$$\begin{aligned}
\|\lambda - \mu_h\|_{H^{-1/2}(\Gamma)} &\leq C h_0^{\frac{1}{2}+\sigma} \left\| \frac{\partial \phi}{\partial \boldsymbol{\nu}} \right\|_{\sigma,\Gamma}, \\
&\leq C h^{\frac{1}{2}+\sigma} \|\phi_0\|_{\sigma+\frac{3}{2},\Omega_0}, \\
&\leq C h^{\frac{1}{2}+\sigma} \left(\|\phi_0\|_{\sigma+\frac{3}{2},\Omega_0} + \|\phi_1\|_{\sigma+\frac{3}{2},\Omega_1} \right).
\end{aligned}$$

In the first line, h_0 is the longest edge of all the elements in Ω_0. The result then follows immediately. ∎

Before finding bounds on the approximation error, we construct a lifting from $M_h \to \mathcal{U}_h^0$.

Lemma 5.6.3. *There exists a lifting $R_{h,\Omega_0} : M_h \to \mathcal{U}_h^0$, such that for any $\mu_h \in M_h$,*

$$\|R_{h,\Omega_0}(\mu_h)\|_{a,\Omega_0} \leq C \|\mu_h\|_{\frac{1}{2},\Gamma}.$$

Proof: Consider any $\mu_h \in M_h$. Then, since μ_h is continuous along Γ, $\mu_h \in H^1(\Gamma)$. Thus, by surjectivity of the trace operator, we have that there exists an operator $R_{\Omega_0} : H^{\frac{1}{2}}(\Gamma) \to H^1(\Omega_0)$ such that

$$\|R_{\Omega_0}(\mu_h)\|_{1,\Omega_0} \leq C \|\mu_h\|_{\frac{1}{2},\Gamma}.$$

We introduce the Scott-Zhang interpolator $\mathcal{SZ}_h$, (see expressions (2.12) and (2.13) in [55]), where

$$\mathcal{SZ}_h : H^1(\Omega_0) \to \mathcal{U}_h^0,$$

and

$$\|\mathcal{SZ}_h(v)\|_{1,\Omega_0} \leq C \|v\|_{1,\Omega_0}.$$

The Scott-Zhang interpolator preserves the boundary value; i.e., $\mathcal{SZ}_h(v)|_\Gamma = v|_\Gamma$, if $v|_\Gamma \in M_h$.

We let $\mathcal{R}_{h,\Omega_0} = \mathcal{SZ}_h \circ \mathcal{R}_{\Omega_0}(\mu_h)$. Then we have that,

$$\|\mathcal{R}_{h,\Omega_0}(\mu_h)\|_{a,\Omega_0} \leq C \|\mathcal{R}_{h,\Omega_0}(\mu_h)\|_{1,\Omega_0} \leq C \|\mathcal{R}_{\Omega_0}(\mu_h)\|_{1,\Omega_0} \leq C \|\mu_h\|_{\frac{1}{2},\Gamma}.$$

∎

We now find bounds on the approximation error.

Theorem 5.6.4. *For $w = (w_0, w_1) \in H^\delta(\Omega_0) \times H^\delta(\Omega_1)$, with $1\langle\delta \leq s+1$ there exists a constant C independent of h such that*

$$\inf_{v_h \in \mathcal{V}_{\kappa h}} \|w - v_h\|_a \leq C h^{\delta-1}(\|w_0\|_{\delta,\Omega_0} + \|w_1\|_{\delta,\Omega_1}). \tag{5.6.6}$$

Proof: We have that

$$\begin{aligned}\|w - v_h\|_a &= \left(\|w - v_h\|^2_{a,\Omega_0} + \kappa \|w - v_h\|^2_{a,\Omega_1}\right)^{\frac{1}{2}}, \\ &\leq \|w - v_h\|_{a,\Omega_0} + \sqrt{\kappa}\, \|w - v_h\|_{a,\Omega_1}.\end{aligned}$$

Let π_{h,Ω_i} be the Lagrange interpolant operator of degree s on Ω_i. We can set $v_h|_{\Omega_1} = \pi_{h,\Omega_1} w_1$, so that we have

$$\|w - \pi_{h,\Omega_1} w_1\|_{a,\Omega_1} \leq C \|w - \pi_{h,\Omega_1} w_1\|_{1,\Omega_1} \leq C h_1^{\delta-1} \|w\|_{\delta,\Omega_1}, \tag{5.6.7}$$

where the last inequality comes from Theorem 3.1.6 in [12]. Now we need a suitable function $v_h = (\hat{w}_{0,h}, \hat{w}_{1,h})$ where $\hat{w}_{1,h} = \pi_{h,\Omega_1} w_1$ and $\hat{w}_{0,h}$ satisfies

$$\int_\Gamma (\hat{w}_{0,h} - \hat{w}_{1,h})\, \mu_h \, \mathrm{d}s = 0, \qquad \forall \mu_h \in M_h. \tag{5.6.8}$$

Let $\hat{\mu}_h \in M_h$. Then we define

$$\hat{w}_{0,h} = \pi_{h,\Omega_0} w_0 + \mathcal{R}_{h,\Omega_0}(\hat{\mu}_h),$$

To satisfy Equation (5.6.8), we have that

$$\begin{aligned}&\int_\Gamma (\hat{w}_{0,h} - \hat{w}_{1,h})\, \mu_h \, \mathrm{d}s = 0, \ \forall \mu_h \in M_h = 0 \\ &\qquad \iff \int_\Gamma \hat{\mu}_h \mu_h \, \mathrm{d}s = \int_\Gamma (\kappa \pi_{h,\Omega_1} w_1 - \pi_{h,\Omega_0} w_0)\, \mu_h \, \mathrm{d}s, \ \forall \mu_h \in M_h.\end{aligned}$$

Thus, $\hat{\mu}_h$ is the $L^2(\Gamma)$ projection of $\kappa\pi_{h,\Omega_1}w_1 - \pi_{h,\Omega_0}w_0$ on M_h, and we have that

$$\begin{aligned}
\|\hat{\mu}_h\|_{0,\Gamma} &\leq \|\kappa\pi_{h,\Omega_1}w_1 - \pi_{h,\Omega_0}w_0\|_{0,\Gamma}\,, \\
&= \|\kappa\pi_{h,\Omega_1}w_1 - \pi_{h,\Omega_0}w_0 + (w_0 - \kappa w_1)\|_{0,\Gamma}\,, \\
&\leq \|\kappa\pi_{h,\Omega_1}w_1 - \kappa w_1\|_{0,\Gamma} + \|w_0 - \pi_{h,\Omega_0}w_0\|_{0,\Gamma}\,, \\
&\leq C\left[\left(\sum_{j=1}^{J}\|\pi_{h,\Omega_1}w_1 - w_1\|^2_{0,\Gamma_j}\right)^{1/2} + \left(\sum_{j=1}^{J}\|w_0 - \pi_{h,\Omega_0}w_0\|^2_{0,\Gamma_j}\right)^{1/2}\right], \\
&\leq C\left[\left(\sum_{j=1}^{J}ch_1^{2\left(\delta-\frac{1}{2}\right)}|w_1|^2_{\delta-\frac{1}{2},\Gamma_j}\right)^{1/2} + \left(\sum_{j=1}^{J}ch_0^{2\left(\delta-\frac{1}{2}\right)}|w_0|^2_{\delta-\frac{1}{2},\Gamma_j}\right)^{1/2}\right], \\
&\leq Ch^{\delta-\frac{1}{2}}\left[\left(\sum_{j=1}^{J}\|w_1\|^2_{\delta-\frac{1}{2},\Gamma_j}\right)^{1/2} + \left(\sum_{j=1}^{J}\|w_0\|^2_{\delta-\frac{1}{2},\Gamma_j}\right)^{1/2}\right], \\
&\leq Ch^{\delta-\frac{1}{2}}\left[\left(J\|w_1\|^2_{\delta,\Omega_1}\right)^{1/2} + \left(J\|w_0\|^2_{\delta,\Omega_0}\right)^{1/2}\right], \\
&\leq Ch^{\delta-\frac{1}{2}}\left(\|w_1\|_{\delta,\Omega_1} + \|w_0\|_{\delta,\Omega_0}\right).
\end{aligned} \tag{5.6.9}$$

Here, at the fifth line we applied Proposition 1.12 of [15], and the second last inequality is due to the continuity of the trace operator (Theorem 1.5.2.1, [24]).

Thus, we have that

$$\begin{aligned}
\|w - v_h\|_a &\leq \|w - \hat{w}_{0h}\|_{a,\Omega_0} + \sqrt{\kappa}\,\|w - \hat{w}_{1h}\|_{a,\Omega_1}\,, \\
&\leq C\left(\|w - \hat{w}_{0h}\|_{1,\Omega_0} + \|w - \hat{w}_{1h}\|_{1,\Omega_1}\right), \\
&\leq C\left(\|w - \pi_{h,\Omega_0}w_0\|_{1,\Omega_0} + \|R_{h,\Omega_0}(\hat{\mu_h})\|_{1,\Omega_0} + Ch_1^{\delta-1}\|w_1\|_{\delta,\Omega_1}\right), \\
&\leq C\left(Ch_0^{\delta-1}\|w_0\|_{\delta,\Omega_0} + C\|\hat{\mu}_h\|_{\frac{1}{2},\Gamma} + Ch_1^{\delta-1}\|w_1\|_{\delta,\Omega_1}\right), \\
&\leq C\left(Ch_0^{\delta-1}\|w_0\|_{\delta,\Omega_0} + Ch^{-\frac{1}{2}}\|\hat{\mu}_h\|_{0,\Gamma} + Ch_1^{\delta-1}\|w_1\|_{\delta,\Omega_1}\right), \\
&\leq Ch^{\delta-1}\left(C\|w_0\|_{\delta,\Omega_0} + \|w_1\|_{\delta,\Omega_1}\right).
\end{aligned} \tag{5.6.10}$$

Here, the second last line comes from the inverse inequality (Corollary 1.141, [15]).

The result then follows immediately. ∎

We finally have arrived at the error bounds of $w - w_h$.

Theorem 5.6.5. *For $(w_0, w_1) \in H^\delta \times H^\delta$ with $2 \leq \delta \leq s+1$, there exists a constant C independent of h such that*

$$\|w - w_h\| \leq Ch^{\delta-1}\left(C\|w_0\|_{\delta,\Omega_0} + \|w_1\|_{\delta,\Omega_1}\right). \tag{5.6.11}$$

Proof: The result is a direct consequence of Theorems 5.6.2 and 5.6.4. ∎

Remark 5.6.6. In this section we provided an error analysis in the case when $c = 0$. This case is biologically relevant. We have proved our scheme approximates well an equation that describes population density for a species whose individuals may have a habitat preference and habitat-dependent dispersal rates over a stationary habitat.

5.7 Numerical Test Cases

In this chapter we present first a numerical validation of the finite element method with test cases derived from the spatially one-dimensional model. We then present a biologically motivated scenario, which we then discuss.

We implement the finite element method using the FreeFEM++ finite element library [25].

5.7.1 Validation

In Chapter 3 we numerically validated a finite difference method for the spatially 1-dimensional system. We now numerically validate our finite element method by comparison with the finite difference method. Using the technique of Ludwig et al [38] (see Section 2.1.1), we can write the 1-dimensional system on the reference frame as

$$\partial_t w_0 = d_0\partial_{xx}w_0 + c\partial w_0 + w(r - aw), \qquad x < 0, \tag{5.7.1}$$
$$\partial_t w_1 = d_1\partial_{xx}w_1 + c\partial w_1 - m_1 w_1, \qquad 0 < x < L, \tag{5.7.2}$$
$$w_0 = k^\alpha w_1, \qquad x = 0, \tag{5.7.3}$$
$$d_0\partial_x w_0 + cw_0 = d_1\partial_x w_1 + cw_1, \qquad x = 0, \tag{5.7.4}$$
$$d_0\partial_x w + cw = bw, \qquad x = L, \tag{5.7.5}$$
$$\lim_{x\to-\infty} w(x,t) = 0. \tag{5.7.6}$$

That is, we can rewrite the system on a semi-bounded domain where the boundary coefficient $b = b(\beta, d_2, m_2, c)$, at $x = L$ is a constant [39]. Here, the parameters β, d_2, and m_2, are defined as in System (2.1.1). Steady-state solutions to this system over $x < 0$ are exponential curves; i.e., $w_1 \sim e^{n^+ x,}$ where $n^+ > 0$, and is dependent on

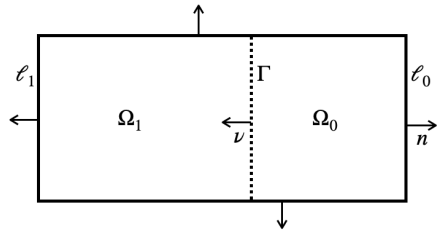

Figure 5.2: An illustration of the bi-domain for numerical validation

the parameters of the system [39]. Thus, over $x < 0$, far enough away from $x = 0$, solutions are flat.

An analogous 2-dimensional system is

$$\partial_t w = d_i \Delta w + (\boldsymbol{c} \cdot \nabla) w + G(w), \qquad \text{on } \Omega \backslash \Gamma, \tag{5.7.7}$$

$$w_0 = \kappa w_1, \qquad \text{on } \Gamma, \tag{5.7.8}$$

$$d_0 \partial_{\boldsymbol{\nu}} w_0 + (\boldsymbol{c} \cdot \nu) w_0 = d_1 \partial_{\boldsymbol{\nu}} w_1 + (\boldsymbol{c} \cdot \nu) w_1, \qquad \text{on } \Gamma, \tag{5.7.9}$$

$$d_0 \partial_{\boldsymbol{n}} w + (\boldsymbol{c} \cdot \boldsymbol{n}) w = b w, \qquad \text{on } \ell_0, \tag{5.7.10}$$

$$\partial_n w = 0, \qquad \text{on } \partial\Omega \backslash (\ell_1 \cup \ell_0), \tag{5.7.11}$$

$$\lim_{\boldsymbol{x} \to -\infty} w = 0, \tag{5.7.12}$$

where $\Omega = \Omega_1 \cup \Omega_0 \cup \Gamma$, and $\Omega_1 = \{(x, y) \in \mathbb{R}^2 \mid x < 0, -H' < y < H''\}$, $\Omega_0 = \{(x, y) \in \mathbb{R}^2 \mid 0 < x < L, -H' < y < H''\}$, $\Gamma = \{(x, y) \in \mathbb{R}^2 \mid x = 0, -H' < y < H''\}$, and $\ell_0 = \{(x, y) \in \mathbb{R}^2 \mid x = L, -H' < y < H''\}$. Here, $\boldsymbol{n}$ is the outward-pointing unit normal on $\partial\Omega$. In this special case, $c = (c_1, 0)$. This system is spatially homogeneous in the y-direction and spatially heterogeneous in the x-direction. Under conditions that the population persists, the numerical solution approaches a steady-state, which in the physical frame, is a travelling-pulse. Cuts of the solution along the x-direction is the steady-state solution to System (5.7.1) - (5.7.6).

We apply the hybrid finite element method to System (5.7.7) - (5.7.11) by truncating the subdomain Ω_1 at $\ell_1 = \{(x, y) \in \mathbb{R}^2 | x = -L', -H' < y < H''\}$, where $L' > 0$ (Figure 5.2). On this boundary, we set homogeneous Dirichlet boundary conditions. The value of L' is chosen large enough so that the solutions are flat out near the boundary ℓ_1.

We implement our finite element method with $\mathbb{P}_1$ approximations for both the Lagrange multiplier and the function w. Inside Ω_1 far away from Γ, the solution is nearly constant, so, we use an increasing element size progressing away from Γ (Figure 5.4). FreeFEM++ internally builds the mesh. The mesh is conformal inside each Ω_i, but across Γ, the mesh is nonconformal. Thus, we have a locally conformal/globally nonconformal mesh. The details of the mesh description are given on a case-by-case basis.

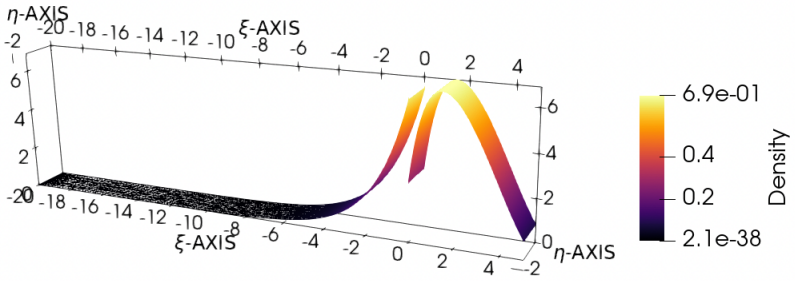

Figure 5.3: A 2-dimensional travelling pulse profile.

At steady-state, $\partial_t w = 0$. We employ this as a stopping condition for our scheme. We let w^n denote the numerical solution at time τn, where τ is the time step, which we take to be uniform. Then we approximate the square of the L^2 norm of the time derivative as

$$||\partial_t w||^2_{0,\Omega} \approx ||w^n||^2_{\tau,0,\Omega} := \sum_{i=0}^{1} \int_{\Omega_{ih}} \left(\frac{w^{n+1} - w^n}{\tau} \right)^2 \, \mathrm{d}\boldsymbol{x},$$

where Ω_{ih} is the discretised domain of Ω_i, $i = 1, 2$. To calculate the integral in FreeFEM++, the software uses a 6^{th} order quadrature formula which is exact for polynomials of degree 5. We stop the iterations once $||w^n||^2_{\tau,0,\Omega} < 10^{-5}$.

We denote by U_{FD} the solution of the one-dimensional model, computed using the finite difference scheme presented in Chapter 3. For each test case, U_{FD} is determined via mesh refinement and is a grid independent solution within 1%. For each simulation, we stop the scheme once the forward difference approximation of the time derivative in the L^∞ norm is below 10^{-3}. The details of the numerical parameters are given on a case-by-case basis.

The numerical solution determined by the finite element method is a travelling pulse that is uniform in the y-direction (Figure 5.3). Using the open-source software ParaView [1], we extract the solution along a cut in the x-direction, which we denote by $U_{h,\tau}$, where h is a measure of the grid size, and τ is the time step used in the scheme. In MATLAB®, we look for numerical parameter values for which $U_{h,\tau}$ is superimposed on U_{FD}. Here, $U_{h,\tau}$ and U_{FD} are vectors whose j^{th} component is the approximation of the value of the travelling pulse solution over the reference frame at (ξ_j, η_0), where η_0 is a constant. We interpolate U_{FD} onto the extracted grid of $U_{h,\tau}$. We calculate the relative error, $e_\infty\left(U_{h,\tau}, U_{FD}\right)$, in the infinity norm, where

$$e_\infty\left(U, V\right) = \frac{\|U - V\|_\infty}{\|V\|_\infty}.$$

We also look at the grid dependence of the finite element method. We assign the numerical solution found on the finest grid to be the reference solution, U_r. We test

Table 5.1: The parameter sets for validation

Test Case	α	β	D_1	D_2	m_1	m_2	c
humped shaped	0.3	0.3	1	1	1	1	1
decreasing	0.8	0.5	1	1	1	0.5	1.5
sharply decreasing	0.8	0.6	2	1.3	0.1	1.4	2.5

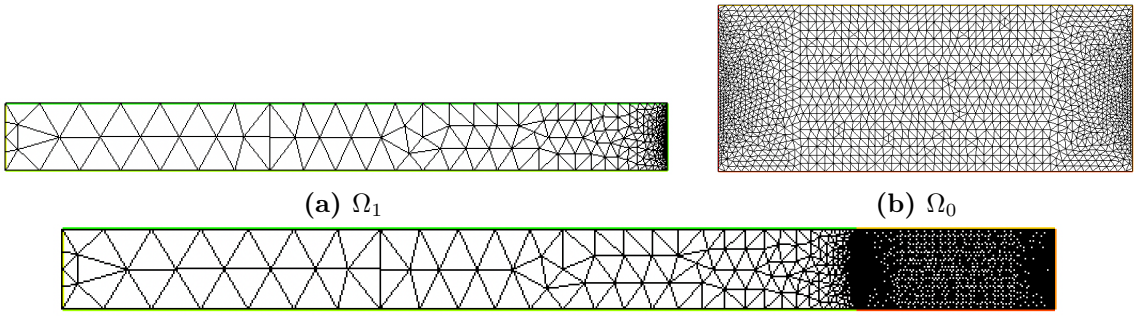

(a) Ω_1 **(b)** Ω_0

(c) Ω

Figure 5.4: The coarsest triangulation for validation. Panel (a): $\mathcal{T}_h^1$. Panel (b): $\mathcal{T}_h^0$, stretched for visual ease. Panel (c): $\mathcal{T}_h^1 \cup \mathcal{T}_h^0$

how good this reference solution is via comparison to the solutions on the coarser grids with the relative error in the infinity norm; i.e., we compute $e_\infty\left(U_{h,\tau}, U_r\right)$.

We choose three different sets of model parameters, called humped shaped, decreasing, and sharply decreasing, which describe the shape of the profile inside the suitable habitat (Table 5.1). Since the finite dimensional scheme is written for the scaled system, we always take $D_0 = r = a = 1$.

humped shaped: We run the simulation four times, where each time we refine both the time-step and the spatial grid. We take $L = 5$, and $L' = 20$. Our coarsest grid has 30 nodes across the x-direction in Ω_1, and 50 uniformly spaced nodes across the x-direction in Ω_0. In the y-direction, we place 5 nodes on ℓ_1, 50 nodes along both sides of Γ and 50 nodes along ℓ_2 (Figure 5.4). Our finest grid has 8 times more nodes for each of the listed quantities. Let h be the measure of the largest triangle on our coarsest grid.

Using the notation of Chapter 3, the solution U_{FD} is computed over a computational domain where $(a_1, a_2) = (4, 1)$, $h_0 = 2.5 \times 10^{-3}$, $r = 1.005$, $k = 2.5 \times 10^{-2}$. This solution is grid independent to the solution computed on the finer grid with $(h_0, k) = (1.25 \times 10^{-3}, 1.25 \times 10^{-3})$, with a relative error in the infinity norm of approximately 3×10^{-4}.

The finite element solutions are superimposed on U_{FD} (Figure 5.5). The relative error, $e_\infty(U_{h,\tau}, U_{FD})$ is below 0.1% for each solution, except for our solution on

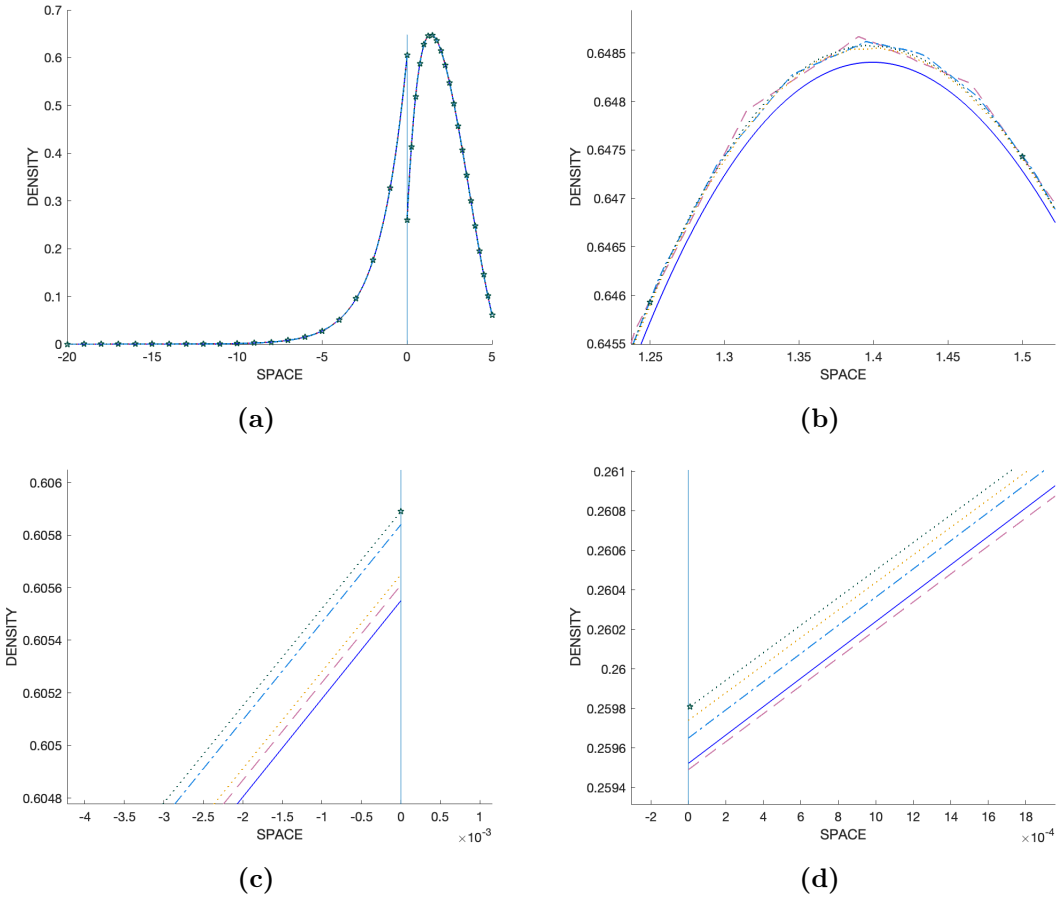

Figure 5.5: The four numerical solutions, $U_{h,0.1}$ (dashed, purple), $U_{\frac{h}{2},0.05}$ (dot-dashed, light blue), $U_{\frac{h}{4},0.025}$ (dotted, orange) and $U_{\frac{h}{8},0.0125}$ (dotted with pentagon maker, green) plotted against U_{FD} for parameter set "hump shaped". Panel (a): All of the curves are superimposed on U_{FD} (solid, dark blue). Panel (b): The hump of the curves. Panel (c): The curves approaching the left side of the interface. Panel (d): The curves approaching the right side of the interface. The vertical line is the interface Γ.

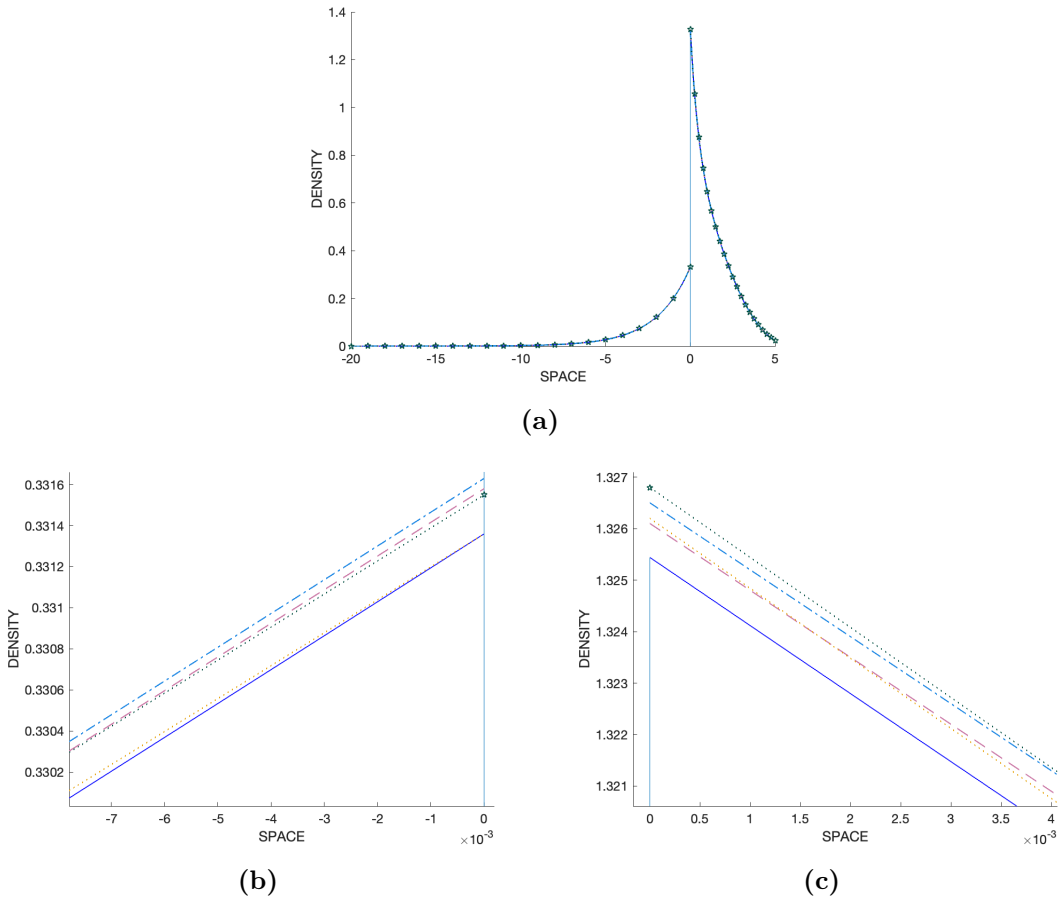

Figure 5.6: The four numerical solutions, $U_{h,0.1}$ (dashed, purple), $U_{\frac{h}{2},0.05}$ (dot-dashed, light blue), $U_{\frac{h}{4},0.025}$ (dotted, orange) and $U_{\frac{h}{8},0.0125}$ (dotted with pentagon maker, green) plotted against U_{FD} for parameter set "decreasing". Panel (a): All of the curves are superimposed on U_{FD} (solid, dark blue). Panel (b): The curves approaching the left side of the interface. Panel (c): The curves approaching the right side of the interface. The vertical line is the interface Γ.

the coarsest grid, where the relative error is approximately 0.14% (Table 5.2). In refining the finite element mesh, $e_\infty(U_{h,\tau}, U_{FD})$ approaches the accuracy of U_{FD}. On the last two finest meshes the computed relative error stops decreasing as it is too close to the tolerance prescribed on the finite difference solution (Table 5.2).

We set $U_{\frac{h}{8},0.0125} = U_r$. The solutions are all within 1% relative error to U_r (Table 5.3). The decay of the error for the first two solutions suggests a better than linear convergence, although as we further refine the mesh, the relative error is limited by the tolerance prescribed on our reference solution U_r.

decreasing: For the finite element approximation we use the same four meshes as we did for parameter set "humped shaped".

Using the notation of Chapter 3, the solution U_{FD} is computed over a computational domain where $(a_1, a_2) = (4, 1)$, $h_0 = 1.25 \times 10^{-3}$, $r = 1.005$, $k = 1.25 \times 10^{-3}$. This solution is grid independent to the solution computed on the coarser grid $(h_0, k) = (2.5 \times 10^{-3}, 2.5 \times 10^{-2})$, with a relative error in the infinity norm of approximately 1.3×10^{-3}.

The finite element solutions are superimposed on U_{FD} (Figure 5.5). All the solutions satisfy $e_\infty(U_{h,\tau}, U_{FD}) \leq 0.1\%$ (Table 5.2). The relative error $e_\infty(U_{h,\tau}, U_{FD})$ remains within the bounds of the accuracy prescribed on U_{FD} with no possible decay as we refine the mesh.

We set $U_{\frac{h}{8},0.0125} = U_r$. The solutions are all within 1% relative error to U_r (Table 5.3). Again, the decay of the error for the first two solutions suggests a better than linear convergence, with the tolerance on U_r also limiting further improvement of the accuracy for the last solution (Table 5.3).

sharply decreasing: Here, we take $L = 5$ and $L' = 250$. We impose the exact same number of nodes along each boundary as we did in the two previous test cases. In this case, to achieve an exponential curve along a cut in the unsuitable habitat, we stop the simulation once $||w^n||^2_{\tau,0,\Omega} < 10^{-7}$.

Using the notation of Chapter 3, the solution U_{FD} is computed over a computational domain where $(a_1, a_2) = (50, 1)$, $h_0 = 7.8125 \times 10^{-5}$, $r = 1.005$, $k = 7.8125 \times 10^{-4}$. This solution is approximately grid independent to the solution computed on the coarser grid $(h_0, k) = (1.5625 \times 10^{-4}, 1.5625 \times 10^{-3})$, with a relative error in the infinity norm of approximately 1.1×10^{-2}. Simulations for these solutions are stopped when the forward difference approximation of the time derivative in the L^∞ norm is below 10^{-5}.

All the solutions have the correct qualitative behaviour and the solutions on the finer grids are superimposed on U_{FD} (Figure 5.7). On the coarsest grid, the largest error occurs near the interface where the solution visibly differs from

Table 5.2: The relative error between the numerical solutions of the finite element solver and U_{FD}, for $\mathcal{P}_1$ approximations of the dual and primal variable

$e_\infty(U_{h,\tau}, U_{FD})$					U_{FD} accuracy
	$U_{h,0.1}$	$U_{\frac{h}{2},0.05}$	$U_{\frac{h}{4},0.025}$	$U_{\frac{h}{8},0.0125}$	
humped shaped	0.0014	0.0006	0.0005	0.0006	3×10^{-4}
decreasing	0.0010	0.0009	0.0008	0.0010	1.3×10^{-3}
sharply decreasing	0.1266	0.0041	0.0018	0.0057	1.1×10^{-2}

Table 5.3: The relative error between the finite element solutions and the finite element solution on the finest mesh.

$e_\infty\left(U_{h,\tau}, U_{\frac{h}{8},0.0125}\right)$			
	$U_{h,0.1}$	$U_{\frac{h}{2},0.05}$	$U_{\frac{h}{4},0.025}$
humped shaped	0.0012	0.0004	0.0004
decreasing	0.0005	0.0002	0.0005
sharply decreasing	0.1216	0.0099	0.0075

U_{FD}. The relative errors for the finer meshes are below 1%, but again, the relative error cannot decrease far below the tolerance on U_{FD} (Table 5.2).

Again, we set $U_{\frac{h}{8},0.0125} = U_r$. The pattern still suggests better than linear convergence (Table 5.3).

Remark 5.7.1. If we choose $\mathbb{P}_2$ approximations for w, then we cannot choose $\mathbb{P}_2$ approximations for λ, as the resulting solution is inaccurate along the interface. In this spatial set up we have that $\Gamma \cap \partial\Omega \neq \varnothing$. In the literature, this situation needs to be treated specially (see Section 2.2.2), where the approximation of the Lagrange multiplier is of polynomial order $\leq s-1$ on F if a vertex of F lies on $\partial\Omega$ [6]. Going forward, we don't consider situations where $\Gamma \cap \partial\Omega \neq \varnothing$. We are interested in situations where the suitable habitat is surrounded by unsuitable habitat in all directions. Thus, $\Gamma \cap \partial\Omega = \varnothing$.

In this section, we compared our finite element solutions to those of the finite difference scheme. We found in all cases that solutions agreed well. We see that with steep curves, care should be taken in the mesh size and the stopping criteria threshold may need to be taken smaller.

5.7.2 An Ecological Application

We present an application of the finite element method for an ecologically motivated scenario. To work in 1-dimensional space, we first make the assumption that in one

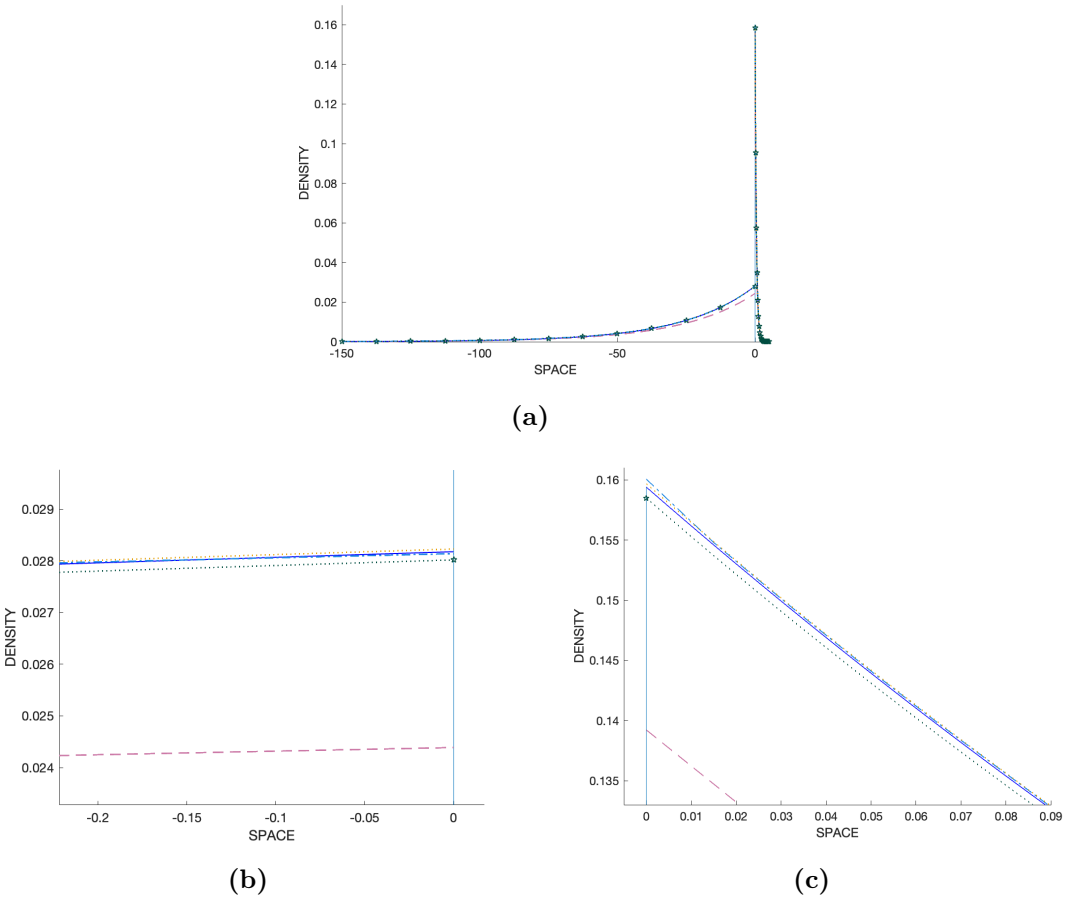

Figure 5.7: The four numerical solutions, $U_{h,0.1}$ (dashed, purple), $U_{\frac{h}{2},0.05}$ (dot-dashed, light blue), $U_{\frac{h}{4},0.025}$ (dotted, orange) and $U_{\frac{h}{8},0.0125}$ (dotted with pentagon maker, green) plotted against U_{FD} for parameter set "sharply decreasing". Panel (a):The qualitative behaviour matches U_{FD} (solid, dark blue) The solutions differentiate near the interface. Panel (b): The curves approaching the left side of the interface. Panel (c): The curves approaching the right side of the interface. The vertical line is the interface Γ.

direction the habitat is completely homogeneous. One impelling reason to work in 2-dimensional space is to drop this assumption.

We assume our suitable habitat is a circular disk so that in every direction, the habitat suitability changes at an equal distance from the point $\boldsymbol{x} = (x_0(t), y_0(t))$. We take $\Omega_0(t) = \{\boldsymbol{x} \in \mathbb{R}^2 \ : \ (x - c_1 t)^2 + (y - c_2 t)^2 < 2\}$ and $\Omega_1(t) = \{\boldsymbol{x} \in \mathbb{R}^2 \ : \ (x - c_1 t)^2 + (y - c_2 t)^2 > 2\}$. Thus, $\Gamma(t) = \{\boldsymbol{x} \in \mathbb{R}^2 \ : \ (x - c_1 t)^2 + (y - c_2 t)^2 = 2\}$ In the reference frame, $\tilde{\Omega}_i = \Omega_i(0)$ and $\tilde{\Gamma} = \Gamma(0)$. For our computational domain we truncate $\tilde{\Omega}_1$ at a radius of 10. We impose homogeneous Dirichlet boundary conditions along $\partial\tilde{\Omega}$. We use a globally conforming mesh where along partial $\partial\tilde{\Omega}$ we place 80 nodes, and along $\tilde{\Gamma}$ we place 160 nodes. We take a mesh size enlarging from $\tilde{\Gamma}$ out towards $\partial\tilde{\Omega}$. We take a uniform time step of $\tau = 0.025$. For an initial condition we take a Gaussian function

$$w(x, 0) = \frac{20}{2\pi(0.5)(0.5)} \exp\left(-0.5\left(\left(\frac{\xi}{0.5}\right)^2 + \left(\frac{\eta}{0.5}\right)^2\right)\right).$$

Solutions of System (5.2.1) with a constant shift approach a unique travelling pulse solution [4]. Such a solution is a steady-state solution in the reference frame, and so $\partial_t w = 0$. As in the previous section, we employ this as a stopping condition and stop the iterations when $||w^n||^2_{\tau,0,\Omega} < 10^{-5}$.

Our finite element method was analysed under the assumption that the interface was polygonal. Over this computational domain, Γ is a smooth curve. We ran simulations for multiple parameter sets and found that solutions were accurate provided the interface is well represented by the linear mesh.

We present the travelling pulse solution for two of these parameter sets, described in the caption of Figure 5.8. For these cases, we consider the x-axis as moving across latitudinal curves and the y-axis as moving along longitudinal curves, and thus the poleward environmental shift [11] is represented by a constant shift along the positive x direction. The population density profile has a local maximum along the x-axis (Figure 5.8). The shift causes the maximum of the density profile within the suitable habitat to skew towards the opposite direction of the shift. The location of the local maximum of the density profile over the suitable habitat depends on the model parameters. For example, when there is no bias for the suitable habitat, this local maximum occurs within the suitable habitat (Figures 5.8c and 5.8d). Increasing the bias, causes the local maximum to shift towards the boundary Γ, where a cut of the density profile along the x-axis is a decreasing curve (Figures 5.8a and 5.8b).

In the present chapter, we developed a 2-dimensional moving-habitat model in a reaction-diffusion framework. The system can capture arbitrary movement of the interface. We developed a finite element method for the simplest case, that is when the interface moves at a constant speed and there is no deformation of the boundary. With this solver, we can begin to study the impact of spatial heterogeneity in all directions on population persistence and density levels. We gave one example of the

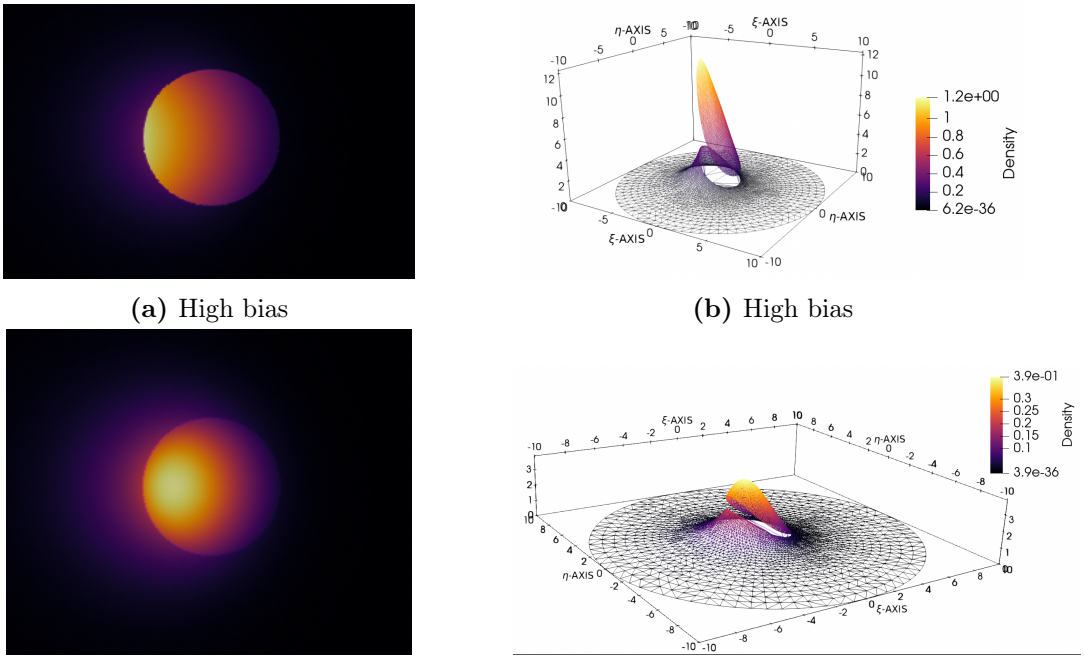

(a) High bias

(b) High bias

(c) No bias

(d) No bias

Figure 5.8: Density over a circular suitable habitat in the reference frame. Panels (a) and (b): $\alpha = 0.7$. Panels (c) and (d): $\alpha = 0.5$. All other parameter values are $d_1 = 2$, $d_0 = 1$, $\boldsymbol{c} = (1, 0)$, $r = 1.2$, $a = 8$, $m = 1$. Density scales are different across rows of panels.

impact of speed of the interface movement, where our numerical results show that the shape of the density profile heavily depends on the speed of the interfaces, much like in the case of the 1-dimensional model. Immediate future projects will more heavily exploit the second dimension to gain insight on the impact of habitat width measured across the axis perpendicular to the axis defining the direction of the shift. Starting with the simplest case gives a platform for foundational results that can be used to support and validate the more difficult cases.

Chapter 6

Conclusion

The primary goal of our research was to develop numerical schemes in one and two space dimensions to accurately capture jumps across arbitrarily moving interfaces. Our research was motivated by the phenomena of climate-driven range shifts and habitat-dependent movement behaviour. Climate-driven range shifts occur when a species shifts its geographical range to follow its suitable habitat, defined by a climatic niche, which is shifting due to climate change. For habitat-dependent movement behaviour, we consider habitat-dependent dispersal rates and habitat bias.

In Chapter 3, we introduce a mathematical model where a bounded interval on the real line represents the suitable habitat, and the half-lines to either side the unsuitable habitat. The points at which the habitat changes suitability are called the habitat edges. They are represented by the end points of the bounded interval. We call these points the interfaces. The interfaces have arbitrary movement, with the conditions that the suitable habitat always has a positive length and that the functions describing the movement are continuous and differentiable. Since we consider habitat-dependent movement behaviour, we impose a jump in density across each interface. The arbitrary movement of the interface and the jump in density motivate the numerical approach. To resolve the difficulty of the moving interfaces, we borrow ideas from the ALE approach, and use the two points of prescribed velocity, our interfaces, to map the spatial coordinate system to a reference frame, in which the interfaces have a fixed position. To solve our system, we develop a finite difference scheme that places two nodes on each interface, which allows us to accurately capture the jump in density. We numerically validate our scheme. We then apply it to three different biologically motivated scenarios of interface movement: constant matching speeds, constant nonmatching speeds, and accelerating speeds.

In the constant matching speeds case, we find parameter ranges for which the total population exceeds the total population in the absence of an environmental shift. In the constant nonmatching speeds case, we show that, even if a suitable habitat is expanding, if the shifting speed of the trailing edge is beyond the critical threshold

speed, then the population will still die out. In the case of accelerating speeds, we look at the time to extinction and determine that a strong habitat bias can actually reduce the time to extinction, as it depletes the "zombie" population.

Chapter 4, we devote to periodic shifting speeds of the interface. By applying the finite difference scheme of Chapter 3, we perform a persistence analysis, and examine the impact of periodic shifting speeds on persisting populations. For each of these analyses, we consider two cases: a constant patch-size and a varying patch-size. For the persistence analysis, we calculate the principal eigenvalue, λ, of the corresponding linearised periodic mapping. This eigenvalue is a metric for persistence, as when $|\lambda| < 1$, the population will go to extinction, and when $|\lambda| > 1$, the population will persist. In both cases, we found that the eigenvalue is a decreasing function of the amplitude of variation, and that populations in faster shifting speeds are more susceptible to variation, in that the eigenvalue passes the bifurcation point at smaller amplitudes relative to the suitable habitat size. In both cases, we found parameter ranges for which the total population exceeds that of the total population in the system without fluctuation. In the case of a constant patch size, this growth can be attributed to low mortality rates and less density dependence due to the fluctuations. In the case of a varying patch size, this growth is attributed to low enough mortality rates and the emergence of periodically occurring invasion fronts.

Lastly, in Chapter 5 we introduce the 2-dimensional analogue of the 1-dimensional system presented in Chapter 3. The interface is now a closed curve. The bounded domain contained within the closed curve represents the suitable habitat, the corresponding unbounded domain, the unsuitable habitat. As we did in Chapter 3, we first restate our system on a reference coordinate system where the interface is fixed in space. On this domain, we derive a hybrid formulation of the semi-discretised system on a truncated domain. With the hybrid formulation we do not have to impose the jump in density on the interface in a strong way via the chosen functional space. Rather, we introduce a mortar element on the interface, which weakly enforces the jump. We prove that the problem is well-posed. We then introduce a finite element formulation of the problem. We prove that this problem is well-posed. We perform an a priori error analysis for the approximation of the density function. We then validate our numerical scheme via comparison to the validated finite difference scheme of Chapter 3. Finally, we present a test case of a biologically motivated scenario.

A main contribution of this thesis is thus the two numerical schemes that have widespread applications to moving-habitat models. For the spatially 1-dimensoinal system, we could add a second species and study multiple different dynamics between the two. Some examples are: cooperative behaviour, competition, and consumer-resource. Potapov and Lewis [48] studied competition in moving-habitat models, but their model did not include habitat-dependent dispersal rates or habitat bias. So we could ask, how the invasion analysis is affected by differing habitat preferences and how temporal variability in speed of the interfaces would effect coexistence. These are

interesting questions that arise from our analysis. For example, suppose that species 1 has a high preference and species 2, the invading species, has a low preference, does the larger "zombie" population assist the population in establishing within the moving habitat? In a pulsating environment, we could likely establish intervals on the amplitude for which the two species coexist.

For the spatially 2-dimensional model, a first project would be to establish persistence conditions for our moving habitat model with habitat-dependent movement rates given a constant habitat shift. In their two papers for moving-habitat models in $d-$dimensional space, Berestycki and Rossi [4, 5], prove that for every population persisting in a bounded habitat without an environmental shift, there exists a critical shifting speed, below which the population can persist in the shifting habitat, and above which, they cannot. That is, the authors relate the shift to the size of the habitat. In the 1-dimensional case, one can analytically characterise the critical patch-size [3, 48, 39]. In the 2-dimensional case, we could numerically determine curves for the critical-patch size as a function of model parameters.

Phillips and Kot [46] studied the critical size of a rectangular habitat shifting in the direction parallel to the $x-$axis in an integro-difference framework, where time is discrete and space continuous. They found that decreasing the width of the rectangle decreased the spectral radius of the operator associated to the eigenvalue problem that determines persistence. If the spectral radius is larger than unity, the population persists, when it is smaller than unity, it goes to extinction. Thus, for every habitat length, there is a minimal habitat width. They also show that there is a limit to how much an increased width benefits the population. Increasing the width without bound asymptotically reaches the scenario of the 1-dimensional case, where the habitat is heterogeneous across only one dimension. They show that by increasing the width, the critical shifting speed curve as a function of net reproductive rate converges to the corresponding curve of the associated 1-dimensional system. Even more so, they show that for some movement behaviour, that width is more important than length, in that when the width is larger than the length, the population has a higher persistence ability.

We could use the finite element method to study the corresponding scenario in the reaction-diffusion framework with our moving-habitat model. If we think about the x-axis as moving across latitudinal curves and the y-axis as moving along longitudinal curves then we would orientate our shift in the x direction. Considering a rectangular suitable habitat would give us the reaction-diffusion analogue studied in [46]. Many of their results rely on the dispersal behaviour, which is determined by the dispersal kernel. A reaction diffusion equation with random dispersal corresponds to the Gaussian kernel, where their results show that width and length are of equal importance. Yet, we could study how the interface conditions affect the importance of width and length. For example, habitat preference could be dependent on latitudinal or longitudinal directions. Although our method was built assuming that the jump

proportionality coefficient, κ, was constant, we conjecture that our methods will work and could be proven to be convergent, perhaps with slight modifications, for weaker assumptions on κ.

Our finite element method can handle many different interface curves. For a predator-prey model, Garvie et al [22] found that the geometry of the boundary and the boundary conditions could generate solutions of periodic travelling wave type, and even spatiotemporal chaos. In the same spirit as Garvie et al [22], we could test the effect of the interface geometry on the solution. For a single species model, this would be similar to what we already discussed relevant to the research of Phillips and Kot [46]. However, with a two species model, to which we could easily adapt our method, we could study the impact of interface geometry with respect to invasion dynamics.

The development of a finite element method that can handle arbitrary movement of the boundary is still open for future work. In this case, the Lagrange multiplier would be time dependent, and the analysis more involved. The method is worth developing though, as with such a tool, one could study domains that may pulsate in size, or even periodically contract from the "top-down." For this latter scenario, we have in mind a suitable habitat that is passing through a set of narrow corridors.

Both our finite difference scheme and our finite element method use a fixed mesh on the reference frame. This is somewhat limiting in that, given large deformations of the habitat, solutions could lose accuracy as the mesh deforms. For example, in the growing domain studied in Chapter 3, we were limited with how far in time we could go, since the fixed mesh in the reference frame is the mapping of a more and more stretched mesh in the physical frame. Thus, to go further in time, we had to start with a relatively fine spatial mesh. This could be remedied with adaptive meshing [37], where, at every time step, we remesh to retain an appropriate mesh in the reference frame. Remeshing requires interpolation, which in turn, introduces some error.

For the finite element method, we omitted an error analysis on the Lagrange multiplier. Our main concern was the accuracy of the density function, but a more holistic analysis would include estimates on the Lagrange multiplier as well. Furthermore, we could relax the assumption of the shape of the interface and obtain error results for smooth curvilinear interfaces. With any of these error estimates, we could test them in practise on multiple polygonal boundaries.

We have provided efficient and accessible numerical methods for moving-habitat models with habitat-dependent movement behaviour in one and two space dimensions for a wide selection of interface movement and geometric shapes. These schemes can assist researchers in producing novel insights not otherwise attainable via analytical methods. They can help us understand on which species conservation efforts should be focused. They are general enough that they can be adapted to include possible conservation efforts, so to test them via simulation before doing so in a landscape

scenario, which can be expensive and irrevocable. An example population that we are considering for simulation is that of the Atlantic lobster. Reported by the House of Commons and Standing Committee on Fisheries and Oceans [43], their population density has in recent years been higher along the eastern coastline, which for the Canadian economy is good. However in trend with the declining populations along the more southern Atlantic coastlines, the population density is predicted to likely eventually decline in favour of yet more northern latitudes. To what implications this pattern lends itself is of obvious interest to the Canadian people along the east coast due to both its unknown impact on the biodiversity of the coastal ocean and the economy.

Bibliography

[1] U. Ayachit. *The ParaView Guide: A Parallel Visualization Application*. Kitware, Inc., 2015.

[2] F. B. Belgacem. The Mortar finite element method with Lagrange multipliers. *Numerische Mathematik*, 84(2):173–197, 1999.

[3] H. Berestycki, O. Diekmann, C. Nagelkerke, and P. Zegeling. Can a species keep pace with a shifting climate? *Bulletin of Mathematical Biology*, 71:339–429, 2009.

[4] H. Berestycki and L. Rossi. Reaction-diffusion equations for population dynamics with forced speed I - The case of the whole space. *Discrete & Continuous Dynamical Systems*, 21(1):41, 2008.

[5] H. Berestycki and L. Rossi. Reaction-diffusion equations for population dynamics with forced speed II - Cylindrical-type domains. *Discrete & Continuous Dynamical Systems*, 25(1):19, 2009.

[6] C. Bernardi, Y. Maday, and A. T. Patera. Domain Decomposition by the Mortar Element Method. In *Asymptotic and Numerical Methods for Partial Differential Equations with Critical Parameters*, pages 269–286. Springer, 1993.

[7] C. Bernardi, Y. Maday, and A. T. Patera. A new conforming approach to domain decomposition: the mortar element method. In H. Brézis and J. L. Lions, editors, *Nonlinear partial differential equations and their applications, Collège de France Seminar*, volume XI. 1994.

[8] J. Bouhours and T. Giletti. Spreading and Vanishing for a Monostable Reaction–Diffusion Equation with Forced Speed. *Journal of Dynamics and Differential Equations*, 31(1):247–286, 2019.

[9] J. Bouhours and M. A. Lewis. Climate Change and Integrodifference Equations in a Stochastic Environment. *Bulletin of Mathematical Biology*, 78(9):1866–1903, 2016.

[10] R. S. Cantrell and C. Cosner. *Spatial Ecology via Reaction-Diffusion Equations*. John Wiley & Sons, 2004.

[11] I.-C. Chen, J. K. Hill, R. Ohlemüller, D. B. Roy, and C. D. Thomas. Rapid Range Shifts of Species Associated with High Levels of Climate Warming. *Science*, 333(6045):1024–1026, 2011.

[12] P. G. Ciarlet. *The Finite Element Method for Elliptic Problems*. SIAM, 2002.

[13] H. F. Diaz, T. W. Giambelluca, and J. K. Eischeid. Changes in the vertical profiles of mean temperature and humidity in the Hawaiian islands. *Global and Planetary Change*, 77(1-2):21–25, 2011.

[14] J. Donea, A. Huerta, J.-P. Ponthot, and A. Rodríguez-Ferran. Chapter 14: Arbitrary Lagrangian–Eulerian Methods. In *Examine Basic Concepts Behind Interpolation, Error Estimation, Computer Algebra and Geometric Modelling in Computational Mechanics*. Business Wire, 2006.

[15] A. Ern and J.-L. Guermond. *Theory and Practice of Finite Elements*, volume 159. Springer, 2004.

[16] L. C. Evans. *Partial Differential Equations*, volume 19. American Mathematical Society, 2 edition, 2010.

[17] D. A. Falk and K. E. Holsinger. *Genetics and Conservation of Rare Plants*. Oxford University Press on Demand, 1991.

[18] J. Fang, R. Peng, and X.-Q. Zhao. Propagation dynamics of a reaction-diffusion equation in a time-periodic shifting environment. *Journal de Mathématiques Pures et Appliquées*, 147:1–28, 2021.

[19] R. I. Fernandes, B. Bialecki, and G. Fairweather. An ADI extrapolated Crank–Nicolson orthogonal spline collocation method for nonlinear reaction–diffusion systems on evolving domains. *Journal of Computational Physics*, 299:561–580, 2015.

[20] C. B. Field, V. Barros, T. F. Stocker, Q. Dahe, D. Dokken, D. Ebi, M. Mastrandrea, K. Mach, G.-K. Plattner, S. Allen, M. Tignor, and P. Midgley (eds.). *Managing the Risks of Extreme Events and Disasters to Advance Climate Change Adaptation: A Special Report of Working Groups I and II of the Intergovernmental Panel on Climate Change*. Cambridge University Press, 2012.

[21] R. A. Fisher. The Wave of Advance of Advantageous Genes. *Annals of Eugenics*, 7(4):355–369, 1937.

[22] M. R. Garvie, J. Burkardt, and J. Morgan. Simple Finite Element Methods for Approximating Predator–Prey Dynamics in Two Dimensions Using MATLAB. *Bulletin of Mathematical Biology*, 77(3):548–578, 2015.

[23] M. R. Garvie, J. Morgan, and V. Sharma. Finite element approximation of a spatially structured metapopulation PDE model. *Computers & Mathematics with Applications*, 74(5):934–947, 2017.

[24] P. Grisvard. *Elliptic Problems in Nonsmooth Domains*. SIAM, 2011.

[25] F. Hecht. New development in freefem++. *Journal of Numerical Mathematics*, 20(3-4):251–265, 2012.

[26] F. M. Hilker and M. A. Lewis. Predator–prey systems in streams and rivers. *Theoretical Ecology*, 3(3):175–193, 2010.

[27] A. T. Hitch and P. L. Leberg. Breeding Distributions of North American Bird Species Moving North as a Result of Climate Change. *Conservation Biology*, 21(2):534–539, 2007.

[28] S. Hongo, Y. Nakashima, E. F. Akomo-Okoue, and F. L. Mindonga-Nguelet. Seasonal Change in Diet and Habitat use in Wild Mandrills (*Mandrillus sphinx*). *International Journal of Primatology*, 39(1):27–48, 2018.

[29] K. E. Hynes, S. Koh, S. McLachlan, M. Timciska, and D. Bazely. Shedding Light on the Problem of Deer Overgrazing in Carolinian Forests. In S. Bondrup-Nielsen, N. W. P. Munro, G. Nelson, J. H. M. Willison, T. B. Herman, and P. Eagles, editors, *Managing Protected Areas In a Changing World*. Proceedings of the Fourth International Conference on Science and Management of Protected Areas, Centre for Wildlife and Conservation Biology, Acadia University, 2002.

[30] S. F. Iglesias and S. Mirrahimi. Selection and mutation in a shifting and fluctuating environment. *arXiv preprint arXiv:2103.07317*, 2021.

[31] W. Jetz, D. S. Wilcove, and A. P. Dobson. Projected Impacts of Climate and Land-Use Change on the Global Diversity of Birds. *PLoS Biology*, 5(6):e157, 2007.

[32] H. Kierstead and L. B. Slobodkin. The Size of Water Masses Containing Plankton Blooms. *Journal of Marine Research*, 12(1):141–147, 1953.

[33] S. Koh, D. R. Bazely, A. J. Tanentzap, D. R. Voigt, and E. Da Silva. *Trillium grandiflorum* height is an indicator of white-tailed deer density at local and regional scales. *Forest Ecology and Management*, 259(8):1472–1479, 2010.

[34] Z. Li. An Overview of the Immersed Interface Method and Its Applications. *Taiwanese Journal of Mathematics*, 7(1):1–49, 2003.

[35] Z. Li, T. Lin, and X. Wu. New Cartesian grid methods for interface problems using the finite element formulation. *Numerische Mathematik*, 96:61–98, 2003.

[36] P. Lidström. Moving regions in Euclidean space and Reynolds' transport theorem. *Mathematics and Mechanics of Solids*, 16(4):366–380, 2011.

[37] S. Lo. Finite element mesh generation and adaptive meshing. *Progress in Structural Engineering and Materials*, 4(4):381–399, 2002.

[38] D. Ludwig, D. Aronson, and H. Weinberger. Spatial patterning of the spruce budworm. *Journal of Mathematical Biology*, 8(3):217–258, 1979.

[39] J. S. MacDonald and F. Lutscher. Individual behavior at habitat edges may help populations persist in moving habitats. *Journal of Mathematical Biology*, 77(6):2049–2077, 2018.

[40] G. A. Maciel and F. Lutscher. How Individual Movement Response to Habitat Edges Affects Population Persistence and Spatial Spread. *The American Naturalist*, 182(1):42–52, 2013.

[41] S. B. Mamede and C. J. R. Alho. Response of wild mammals to seasonal shrinking-and-expansion of habitats due to flooding regime of the Pantanal, Brazil. *Brazilian Journal of Biology*, 66:991–998, 2006.

[42] C. Mavriplis. *Nonconforming Discretizations and A Posteriori Error Estimators for Adaptive Spectral Element Techniques*. PhD thesis, Massachusetts Institute of Technology, 1989.

[43] K. McDonald. *In Hot Water- Lobster and Snow Crab in Eastern Canada*. House of Commons Canada and Standing Committee on Fisheries and Oceans, 2019.

[44] O. Ovaskainen and S. J. Cornell. Biased movement at a boundary and conditional occupancy times for diffusion processes. *Journal of Applied Probability*, 40(3):557–580, 2003.

[45] H. M. Pereira, P. W. Leadley, V. Proença, R. Alkemade, J. P. Scharlemann, J. F. Fernandez-Manjarrés, M. B. Araújo, P. Balvanera, R. Biggs, W. W. Cheung, et al. Scenarios for Global Biodiversity in the 21st Century. *Science*, 330(6010):1496–1501, 2010.

[46] A. Phillips and M. Kot. Persistence in a Two-Dimensional Moving-Habitat Model. *Bulletin of Mathematical Biology*, 77(11):2125–2159, 2015.

[47] T. Plewa, T. Linde, and V. G. Weirs. *Adaptive Mesh Refinement - Theory and Applications*. Springer, 2005.

[48] A. B. Potapov and M. A. Lewis. Climate and competition: the effect of moving range boundaries on habitat invasibility. *Bulletin of Mathematical Biology*, 66(5):975–1008, 2004.

[49] A. Quarteroni and A. Valli. *Numerical Approximation of Partial Differential Equations*, volume 23. Springer Science & Business Media, 2008.

[50] P.-A. Raviart and J.-M. Thomas. Primal Hybrid Finite Element Methods for 2nd Order Elliptic Equations. *Mathematics of Computation*, 31(138):391–413, 1977.

[51] J. D. Reeve and J. T. Cronin. Edge behaviour in a minute parasitic wasp. *Journal of Animal Ecology*, 79(2):483–490, 2010.

[52] O. Richter, S. Moenickes, and F. Suhling. Modelling the effect of temperature on the range expansion of species by reaction–diffusion equations. *Mathematical Biosciences*, 235(2):171–181, 2012.

[53] R. Sacoo, A. G. Mauri, and G. Guidoboni. A Stabilized Dual Mixed Hybrid Finite Element Method with Lagrange Multipliers for Three-Dimensional Elliptic Problems with Internal Interfaces. *Journal of Scientific Computing*, 82(60), 2020.

[54] C. B. Schultz and E. E. Crone. Edge-Mediated Dispersal Behavior in a Prairie Butterfly. *Ecology*, 82(7):1879–1892, 2001.

[55] L. R. Scott and S. Zhang. Finite element interpolation of nonsmooth functions satisfying boundary conditions. *Mathematics of Computation*, 54(190):483–493, 1990.

[56] W. Shen, Z. Shen, S. Xue, and D. Zhou. Population dynamics under climate change: persistence criterion and effects of fluctuations. *Journal of Mathematical Biology*, 84(4):1–42, 2022.

[57] P. Shukla, J. Skea, E. Calvo Buendia, V. Masson-Delmotte, H.-O. Pörtner, D. C. Roberts, P. Zhai, R. Slade, S. Connors, R. van Diemen, M. Ferrat, E. Haughey, S. Luz, S. Neogi, M. Pathak, J. Petzold, J. Portugal Pereira, P. Vyas, E. Huntley, K. Kissick, M. Belkacemi, and J. Malley (eds.). IPCC, 2019: Climate Change and Land: an IPCC special report on climate change, desertification, land degradation, sustainable land management, food security, and greenhouse gas fluxes in terrestrial ecosystems. 2019.

[58] J. G. Skellam. Random Dispersal in Theoretical Populations. *Biometrika*, 38(1/2):196–218, 1951.

[59] C. D. Thomas, A. Cameron, R. E. Green, M. Bakkenes, L. J. Beaumont, Y. C. Collingham, B. F. Erasmus, M. F. De Siqueira, A. Grainger, L. Hannah, et al. Extinction risk from climate change. *Nature*, 427(6970):145–148, 2004.

[60] M. C. Urban. Accelerating extinction risk from climate change. *Science*, 348(6234):571–573, 2015.

[61] F. Valladares, S. Matesanz, F. Guilhaumon, M. B. Araújo, L. Balaguer, M. Benito-Garzón, W. Cornwell, E. Gianoli, M. van Kleunen, D. E. Naya, et al. The effects of phenotypic plasticity and local adaptation on forecasts of species range shifts under climate change. *Ecology Letters*, 17(11):1351–1364, 2014.

[62] H.-H. Vo. Persistence versus extinction under a climate change in mixed environments. *Journal of Differential Equations*, 259(10):4947–4988, 2015.

[63] B. Zhang, X. Liu, D. L. DeAngelis, W.-M. Ni, and G. G. Wang. Effects of dispersal on total biomass in a patchy, heterogeneous system: Analysis and experiment. *Mathematical Biosciences*, 264:54–62, 2015.

[64] Y. Zhou and W. F. Fagan. A discrete-time model for population persistence in habitats with time-varying sizes. *Journal of Mathematical Biology*, 75(3):649–704, 2017.